Sustainable Cellulose Composite Membranes for Multifunctional Sensing Applications

Sheila M. Goodman

A dissertation
submitted in partial fulfillment of the
requirements for the degree of

Doctor of Philosophy

University of Washington
2021

Reading Committee:
Anthony Dichiara, Chair
Renata Bura
Rick Gustafson

Program Authorized to Offer Degree:
School of Environmental and Forest Sciences

University of Washington

Abstract

Sustainable Cellulose Composite Membranes for Multifunctional Sensing Applications

Sheila M. Goodman

Chair of the Supervisory Committee:
Anthony B. Dichiara
School of Environmental and Forest Sciences

With growing environmental conscientiousness and climate effects being more readily seen around the world, the next generation of wearable electronics will not only be characterized by their portability, flexibility, and drop-in implementation, but also their low cost and environmental impact[1]. A variety of natural polymers have been considered as potential substrates to meet this increasing demand, but none possess the sustainability or commercializability of cellulose. As the most abundant natural polymer, cellulose can be extracted from a number of biological sources, including lignocellulosic biomass[2–4], algae[5–7], and bacterial sources[8]. Cellulose microfibers, extracted from lignocellulosic sources, have been used by societies for thousands of years, and are still the major feedstock of the pulp and paper industries[9]. Recent advances in biopolymer extraction and manipulation have allowed for the isolation of cellulose in its nano form (i.e. cellulose nanofibrils), derived from its naturally occurring hierarchical structure[10]. In this work, membranes comprised of cellulose microfibers and nanofibrils are prepared for multifunctional sensing and energy storage applications. When fabricated using traditional papermaking techniques, cellulose microfibers form a porous

entangled structure. Through the incorporation of carbon nanotubes (CNTs), an electrically conductive cellulose-CNT composite matrix is formed whose electrical resistance changes in response to environmental stimuli. Specifically, the hygroscopic nature of cellulose causes the discrete fibers to swell when immersed in water, driving the matrix below a conductivity percolation threshold, and significantly increasing the electrical resistance. Implemented in tandem with an inexpensive microcontroller, this ‘smart’ paper can function as a stand-alone remote leak detection device. By leveraging mature web-forming techniques, the adaptation of composite ‘smart’ papers from the batch to the pilot-scale was facilitated which allowed for continuous production with minimal nanoparticle loss, demonstrating commercial viability for the rapid and reliable quantification of small volumes of water over large areas. In addition to the investigation of cellulose-CNT composites, cellulose nanofibrils (CNFs) were examined for suitability as the main component in flexible dielectric films, with applications in advanced energy storage and piezoelectric sensing technologies. The dielectric performance and energy storage capabilities of the material were tuned through the optimization of the CNF fabrication process, as well as through the incorporation of poly(vinylidene fluoride) (PVDF) nanoparticles. Optimized performance was further extended through the development of a layer-by-layer fabrication process in which bi- and tri-layer films of varying composition were evaluated, significantly improving breakdown strength and permittivity. In this work, cellulose-based composites were successfully adapted to multifunctional sensing and energy storage applications, and this exercise offers insight into the possibility of the large-scale integration of biopolymers in the field of flexible electronics.

Table of Content

List of Figures

List of Tables

Acknowledgements

I owe a great deal of gratitude to many people who have worked with and supported me throughout this journey. First, I would like to thank my committee members, Dr. Renata Bura, Dr. Rick Gustafson, and Dr. Jaehyun Chung for their support and research guidance over the last five years. I would like to specially thank the Chateaubriand Fellowship for the opportunity to study abroad in Bordeaux, France and expand my area of research expertise. To my co-advisor Dr. Jinkai Yuan, thank you for the guidance and your tireless efforts to continue our international collaboration during an unprecedented global pandemic. And to my advisor, Dr. Anthony Dichiara, thank you for entrusting me to be your first graduate student and always pushing me to step outside my comfort zone and be the best engineer and scientist I could be. My technical writing skills and love of French wine have flourished under your guidance.

I was lucky enough to have cohorts in both the Bioresource Science and Engineering (BSE) and Chemical Engineering (ChemE) departments here at the University of Washington, and am forever grateful for the friendships I have gained during my graduate career. To my BSE colleagues, Kurt Haunreiter, Dr. Gabriel Suefitelli, and Danielle Pascoli, thank you for always making Bloedel Hall an enjoyable place to come to work every day. To my lab mates Heather Wise and Dylan Edmundson, thank you for being the best part of graduate school and completing the DreamTeam! I have loved learning with and from you both over the last five years and am honored to have been on this journey together. To Victor Hu and Luke Gibson, thank you for accepting me as an honorary ChemE and always being around to help celebrate the highs and commiserate the lows of graduate school. Your love of sunrise hikes and camping trips helped balance out all those long nights in the lab over the years. To the staff at the Molecular Analysis Facility (MAF), especially Dr. Micah Glaz, Scott Braswell, and Ellen Lavoie, thank you for all of your hard work and assistance in incorporating unique ideas and configurations to characterize the most challenging of nanomaterials!

To all of the other friends from New York who have supported me from afar, Wyatt, Maleesa and Rebecca, and Kaylin and Danielle, and the friends who have made Seattle feel like home these last five years, I thank you for your continued friendship and support.

To my parents, Bob and Kathy, thank you for your unending love and support. Your encouragement over the last 28 years has shaped me into the woman and engineer I am today, and I would not have made it this far without you. To my older brother Brian, thank you for encouraging me to take that first engineering class and always making the time to check over my AP calculus and physics homework all those years ago. And finally, to Neal. Your unwavering belief in my ability to succeed has been my greatest strength. Thank you for encouraging me to always give my best in the lab, while reminding me not to sweat the small stuff. I have loved every day of being able to share this experience with my best friend, and I cannot wait to keep working harder and hiking further with you.

Dedication

This is dedicated to my parents, Robert and Kathryn Goodman, for their unwavering love and support. And to my older brother and role model, Brian, without whom I would have never become an engineer.

I. Introduction

1.1 Cellulose composite electronics overview

Flexible wearable electronics have gained considerable interest in recent years for their ability to advance the world of portable electronic devices[11]. With growing demand for mobile electronics and a dependence on Internet of Things (IoT) devices, the portability and robustness of electronic devices is becoming of paramount importance[12]. As demand for energy storage and sensing capabilities continues to rise, novel flexible-electronics with commercial viability are leading research to turn to alternative polymeric materials with enhanced performance[12].

Sensing technology plays an important role in almost every market in the world today, including agriculture, health and safety, medical, and environmental tracking[13]. Characterized by the environmental changes they are tailored for detecting, sensors are frequently divided into three categories including, (i) physical sensors that respond to pressure/strain[14–16], (ii) chemical sensors that respond to ions, pH changes, gas/vapor, or solution changes[17–19], and (iii) biosensors that respond to biomolecules and pathogens, etc.[20,21]. Although recent advances in the literature have focused on developing novel alternative materials for a variety of sensing designs, traditional commercial instrumentation generally retains superior sensitivity and product design. However, traditional materials do face a number of drawbacks, including expensive instrumentation, raw material usage, and a dependence on petrochemical derived sources[13,22,23]. Prompted by a need for more flexible materials for the growing field of wearable electronics, combined with heightened societal conscientiousness and rising climate concerns, a demand for greener materials has sparked recent literature reports in the development of more environmentally friendly alternative polymeric sensing materials[24,25]. As the most abundant natural polymer, cellulose based composites have gained considerable attention in the literature as one of the most widely studied materials for alternative sensor development. Along with its ease of extraction from a variety of biomass sources, flexibility, and mechanical and thermal stability, cellulose based materials offer unique advantages in novel sensor design[25].

A similar push for flexible and sustainable polymeric materials in energy storage technology has also been seen in the literature as demand for electrical energy continues to rise. Recently, dielectric capacitors, which store electrostatic energy in the form of the displacement of charge, have gained significant interest in the literature due to their ability to rapidly release energy, intrinsically high power density and extended life span[26–28]. In particular, polymer based dielectrics are being considered for their increased flexibility and ease of scalable processing conditions compared with traditionally used inorganic materials[26,29]. As the most naturally occurring polymeric material on Earth, cellulose offers biodegradability, flexibility, and innately favorable dielectric properties, making it a compelling sustainable alternative to polymeric dielectrics. Specific interest has been given to the nano-form of cellulose microfibers, referred to as cellulose nanofibrils (CNF), as its unique material properties have demonstrated significant improvement in energy storage capabilities[30–33].

1.2 Cellulose: Extraction and structure

With increasing concerns surrounding industry dependence on fossil fuel use and the associated detrimental environmental effects, the large scale integration of biopolymers has become highly desirable. Cellulose can be found in a variety of forms from multiple feedstock sources, including lignocellulosic biomass[2–4], algae[5–7], and bacterial sources[8]. While lignocellulosic sources require additional processing to isolate the cellulose fibers, they are still the most studied form as they provide the highest abundance of cellulose and benefit from existing extraction and separation infrastructure in place from the well-established pulp and paper industry[18]. Within lignocellulosic biomass exists a complex heterogeneous structure mainly comprised of cellulose (~30-50% by weight), hemicellulose (~19-45% by weight), and lignin (~15-35% by weight), with the exact composition dependent upon the source and type of the biomass[34]. Cellulose is a linear chain homopolymer with the repeating unit comprised of two anhydrous glucose rings, linked by a covalently bonded oxygen between C1 of one monomer and C4 of the adjoining ring through a β 1-4 glucosidic bond[9,10,35]. Interchain hydrogen bonding between hydroxyl groups, combined with the glucosidic and hydrogen bonds between glucose units, helps to stabilize the high molecular weight linkage and promote parallel stacking of chains, forming elementary fibrils that further accumulate into larger cellulose microfibrils, shown in **Figure 1**[36]. Within these cellulose fibrils exist crystalline (ordered) and amorphous (disordered) regions that control the mechanical strength and flexibility of the polymer, respectively[37].

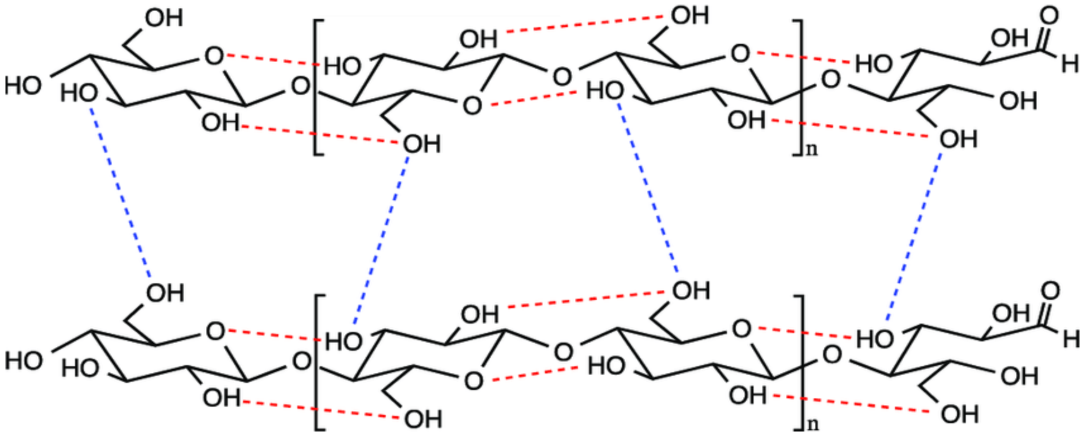

Figure 1. *Cellulose structure*. Structure of cellulose with intra- (red) and inter-chain (blue) hydrogen bonds represented[36]. Reprinted from reference 36, Copyright (2015), with permission from Elsevier.

Hemicellulose consists of a mix of highly branched pentoses (5 C sugars) and hexoses (6 C sugars). Lignin, the second most abundant natural polymer, is a highly complex three-dimensional aromatic macromolecule, constructed from phenylpropanoid monomers with varying degrees of methoxylation[38,39]. The plant cell wall contains a lignin and polysaccharide mixture that helps maintain biomass structure and provides protection from external hazards[40]. The hierarchical structure of cellulose within the complex biomass structure is represented in **Figure 2**. Elementary cellulose chains stack together to form larger microfibrils that further accumulate into larger matrices that make up the biomass cell wall.

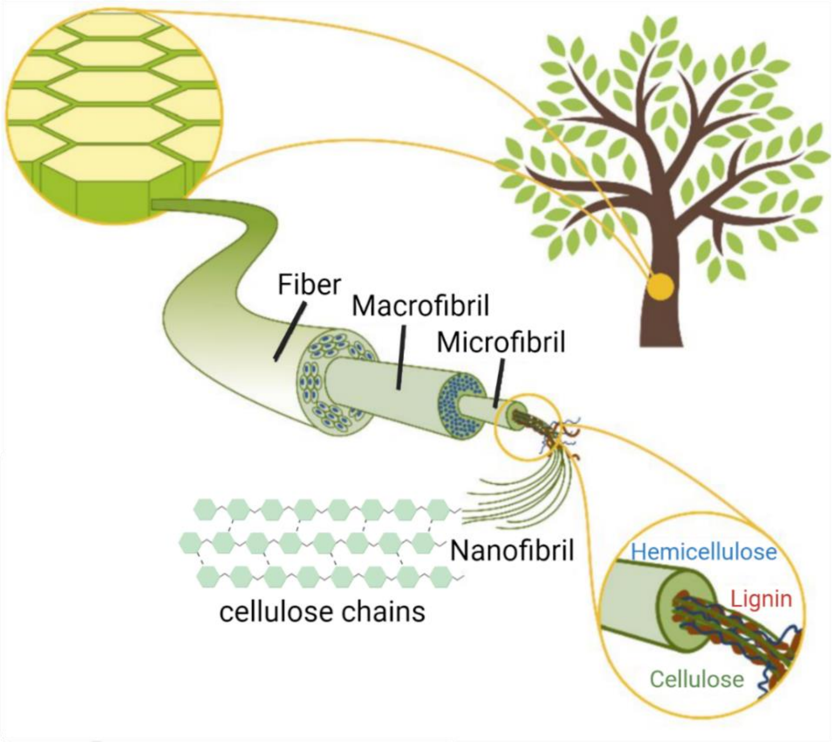

Figure 2. *Representative hierarchical lignocellulosic biomass structure*, adapted with permission from Martin-Martinez et al[41].

The isolation of cellulose fibers from a heterogeneous feedstock material is of paramount importance for its use as a biopolymer, as the cellulose fibers are physically entrained in other feedstock components. Its extraction is typically characterized by two processing steps: the pretreatment of the biomass to disrupt the cell wall and solubilize the polysaccharides and lignin, and the mechanical separation of pretreated biomass into their individual components[40,42]. The Kraft pulping process is most commonly used to isolate cellulose fibers due to its effective lignin removal, which is extremely important when cellulosic fibers will be used for paper based composites, as the presence of lignin and other constituents will limit available cellulose surface area and disrupt interfiber bonding, reducing overall sheet strength[42]. The well-established Kraft pulping processes effectively depolymerizes and solubilizes the lignin while also hydrolyzing and solubilizing some hemicelluloses, priming the remaining biomass to be adequately treated to isolate and extract the cellulose fibers[42]. In general, lignocellulosic biomass is first treated by a high temperature steam pretreatment process in the presence of NaOH and Na_2S under pressure, which initiates the depolymerization and subsequent solubilization of the lignin, resulting in fibers with lignin contents anywhere from 1-10% of the dry total mass[42]. Resulting fibers then undergo a separation process, typically mechanical defibrillation[3,43], acid hydrolysis[42,44,45], or enzymatic hydrolysis[42,44,46] to achieve a desired level of purified and isolated cellulose fibers dependent on the final application. The purified cellulose microfibrils are characterized by a negative charge due to the carboxyl groups on their surface and a degree of polymerization up to ~10,000[39]. Further processing can then be performed to isolate the elementary cellulose fibrils within the extracted microfibrils to achieve subsequent cellulose based materials (cellulose nanocrystals, cellulose nanofibrils, etc.) for a variety of other material properties and use applications.

1.3 Nanocellulose: Extraction and structure

Owing to the naturally hierarchical structure of lignocellulosic biomass, cellulose nanoparticles, more commonly referred to as nanocellulose, can be extracted and isolated as an additional biopolymer by overcoming the interfiber hydrogen bonds or breaking the amorphous region chains via a variety of chemical and mechanical treatments. The term ‘nanocellulose’ refers to a cellulose-based material with at least one dimension in the nanometer range (1-100 nm). Classified based on three main subcategories, including dimension, function, and preparation technique, nanocellulose can be tailored to achieve different resulting structures and orientations, largely dependent on the type of biomass feedstock and the preparation method used[47,48]. The two main types of nanocellulose produced from lignocellulosic materials are cellulose nanocrystals (CNCs) and cellulose nanofibrils (CNFs). Cellulose nanocrystals (CNCs) are characterized by a rod-like shape and low aspect ratio, with typical diameters in the range of 2-20 nm and lengths between 100 nm to several microns[42,47,49]. CNCs are composed of 100% pure cellulose, with high crystallinity, generally between 54 and 88 % dependent upon the source of the cellulose material used to prepare the nanoparticles[46]. Cellulose nanofibrils consist of both crystalline and amorphous regions, similar to the original structure of microfibril cellulose. With average diameters of 2-5 nm and lengths between 500 nm and several microns, the much higher aspect ratio causes CNFs to behave more similarly to traditional polymers, owing their mechanical strength and flexibility to the presence of both crystalline and amorphous regions, respectively[47,50].

A variety of techniques have been studied to achieve individualized nanocellulose particles in solution by using a combination of chemical treatments, including acid hydrolysis[51,52], TEMPO mediated oxidation[50,53–55], or biochemical enzymatic hydrolysis[56], followed by mechanical defibrillation[57], or a combination of the above[54,58]. While acid hydrolysis, mainly utilizing sulfuric acid or peracetic acid[51], yields uniform nanoparticle dimensions, the harsh treatments lead to CNC formation rather than CNFs, limiting the flexibility of the nanomaterial and reducing the similarity to traditional petrochemical derived polymers. Mechanical defibrillation maintains the highest cellulose yield, but with limited ability to achieve cellulose particles on the nanometer scale. TEMPO mediated oxidation, in combination with mechanical defibrillation, has been proven to achieve uniform fiber morphology while maintaining relatively high yields[50,54]. Once pure cellulose has been isolated from its heterogeneous biomass source, TEMPO mediated oxidation is able to efficiently convert primary C6 hydroxyl groups to carboxylates via aldehydes in a regioselective process, according to the mechanism suggested by Isogai et al, presented in **Figure 3**[50].

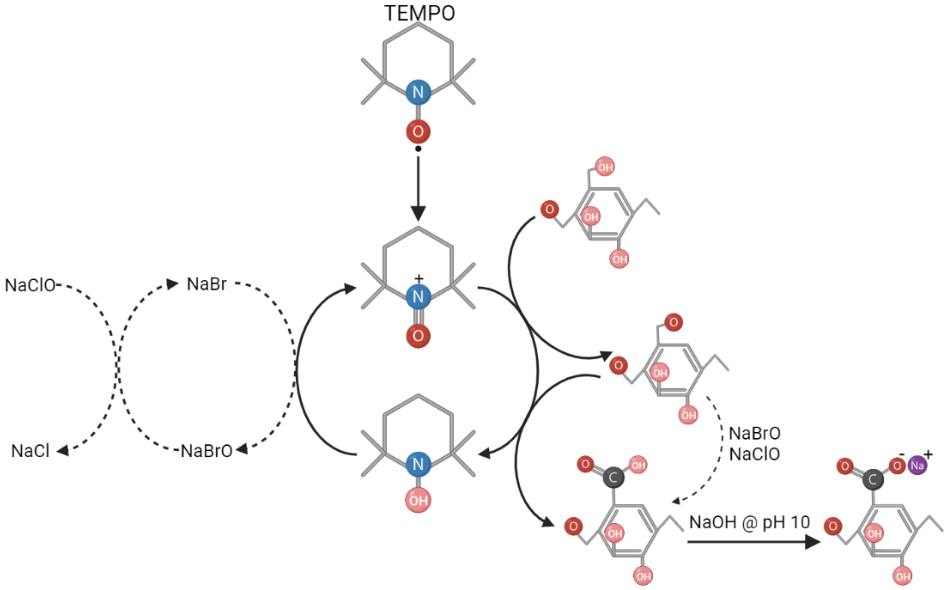

Figure 3. *Regioselective TEMPO-oxidation mechanism* of cellulose C6 primary hydroxyls to carboxylates by the TEMPO/NaBr/NaClO oxidation in water under basic conditions (pH 10-11), as proposed by Isogai et al[50]. Image created with BioRender.

In general, catalytic amounts of both TEMPO, a water soluble and stable nitroxyl radical, and sodium bromide (NaBr), are dissolved in aqueous cellulose solutions under basic conditions, followed by the addition of sodium hypochlorite (NaClO) to initiate the oxidation reaction, efficiently converting primary hydroxyl groups to carboxylates via aldehydes. The oxidation process can be monitored by the pattern of aqueous NaOH consumption, which is continuously added to the reaction mixture to maintain a pH of 10 throughout oxidation. When used in combination with mild mechanical defibrillation (blending, ultra sonication, microfluidic homogenizer, etc.), resulting CNFs with carboxylate content above 0.8 mmol/g cellulose are characterized by their transparent properties and uniform dimensions. Regardless of cellulose feedstock species tested, CNFs prepared from TEMPO mediated oxidation were characterized by high aspect rations, greater than 100, with diameters between 2-4 nm, the smallest elementary fibrils achieved to date from original cellulose wood fibers[50]. The transparency and uniformity of the resulting CNFs affords an application range typically monopolized by petrochemical-based polymers. While nanofibril widths remain constant regardless of the biomass examined, variations in length and surface charge are largely dependent upon oxidation and disintegration conditions, allowing for highly controllable material properties. The surface oxidation, or charge density, characterized by the carboxylate concentration on a fibrils surface, has been proven to be largely dependent on the amount of NaClO added during the oxidation stage and the duration of oxidation. When higher NaClO concentrations are supplied during the oxidation of Kraft pulps, or the oxidation reaction is allowed to proceed for longer amounts of time, the resulting nanofibril carboxylate content is known to increase, yielding more individually available fibrils with improved aqueous dispersion quality, as shown by a higher transmittance in **Figure 4**[3,50,59,60]. The improved dispersion quality and higher surface charge become especially important when CNF is used as a dispersing agent in composite materials[61,62].

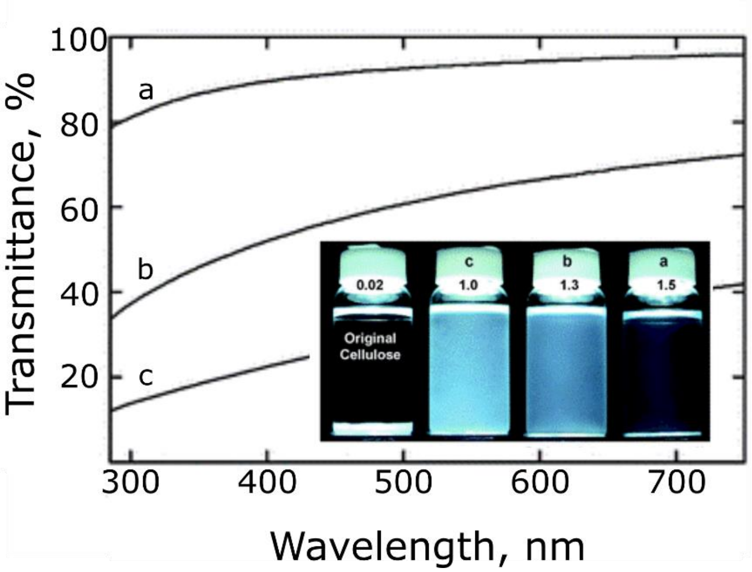

Figure 4. *Dispersion states of TEMPO-oxidized CNF* with varying surface charge densities of, 0.02, 1, 1.3 and 1.5 mmol COOH/g, demonstrated by optical absorption (UV-vis) spectroscopy. Inset shows images of as-prepared TEMPO-oxidized CNF with different charge densities. Adapted with permission from reference 60. Copyright (2007) American Chemical Society[60].

Nanofibril yield, length, and viscosity are highly dependent on mechanical defibrillation conditions, including time and severity of treatment. The tunability of TEMPO mediated oxidation to isolate elementary cellulose nanofibrils with specific desirable characteristics is advantageous for the increased use of cellulose derivatives as alternative polymeric materials. By maintaining the original fibrous morphology of wood celluloses throughout oxidation and mechanical treatment, cellulose nanofibrils are still characterized by strong crystalline regions and flexible amorphous regions, allowing for use as bio-polymers in a variety of applications. Highly tunable surface chemistry results in improved dispersion quality, leading to facile material development in water based suspensions. The use of the most abundant natural polymer as a sustainable and inexpensive feedstock allows for the possibility of cellulose based nanomaterials to compete with commercially available petrochemical-derived polymeric materials in a wide variety of applications.

1.4 Cellulose composites for sensing applications

A variety of techniques to produce cellulose based materials for multifunctional sensing applications have been reported, including films[63,64], aerogels[65], and membranes prepared from a variety of techniques[19,66,67]. While different sensing applications can be met with varying fabrication techniques, preparing cellulose-based materials using traditional papermaking methods demonstrates the most commercial viability by capitalizing on a well-established fabrication process. In general, paper consists of a nonwoven network of randomly oriented fibers laid down to form a mat, typically prepared from cellulose fibers[19]. With the incorporation of electrically conductive fillers (i.e. carbon nanomaterials, metallic nanoparticles, etc.), paper can exhibit an electrical resistance response to external stimuli such as temperature shifts, mechanical deformations, and the presence of liquids and gasses[63,68–72]. This emerging field of ‘smart’ paper-based materials offer compelling alternatives for use in a variety of sensing applications.

The methods for preparing ‘smart’ paper sensors can be classified into two different categories. The first consists of coating a conductive layer on the external surfaces of an already existing paper specimen[19,73]. The second involves mixing the conductive component with cellulose fibers during papermaking to yield a percolated conductive network constituting electrical paths throughout the whole volume of the prepare paper[19,74]. Although both approaches offer short processing times and low cost, the later exhibits higher potential for sensing applications due to increased interactions between the electrically conductive fillers and cellulose fibers. Among a variety of conductive fillers, carbon nanotubes (CNTs), comprising of one or several sheets of hexagonally packed carbon atoms rolled in concentric seamless tubes, have drawn considerable attention due to their exceptional electrically conductivity, mechanical strength, and thermal stability. Since inter-fiber cohesion of cellulose consists of hydrogen bonding, however, one challenge associated with the introduction of CNTs is that the addition of carbon without hydroxyl groups to the pulp matrix inhibits the interaction between cellulose fibers, hindering the mechanical integrity of the paper. In addition, the incorporation of high loadings of CNTs is known to reduce the tensile strength of papers[75]. Recent reports have focused on achieving high loadings of CNTs through unique bonding chemistries and fabrication techniques[19,67,76].

In particular, water sensing applications have been increasingly evaluated for paper based composites given the bio-renewable and hygroscopic nature of cellulose, providing an excellent platform for building sustainable and affordable water sensors. Although existing systems exist that can detect water, typical devices attempt to infer water loss either from a difference in flow rate within a pipeline or through changes in conductivity due to the presence of water. These technologies have significant drawbacks – namely, time consuming human intervention to confirm alerts and inconsistent signals due to moisture effects, respectively. Literature reports of other polymer-based systems are also known to produce inconsistent signals due to material degradation in aqueous environments [77–82]. The unique water sensing mechanism achieved through the hygroscopic nature of the cellulose platform, combined with the electrical conductivity of conductive fillers, allows for rapid and reliable liquid water detection[19,63,83]. While a fifth of the world's population lacks access to safe drinking water, crumbling infrastructure and leaky pipes are major contributors to global water scarcity. Capitalizing on the hygroscopic nature of cellulose combined with the superior electrical conductivity of carbon nanomaterials, paper based composite sensors offer flexibility and versatility for remote water sensing applications that would otherwise be left undetected.

1.5 Carbon nanomaterials as conductive fillers

Carbon nanomaterials, a class of carbon allotropes with at least one dimension between 1 and 100 nm[84,85], have gained considerable attention due to their unique properties, including enhanced surface area, thermal, electrical, and mechanical performance[22]. The most commonly studied allotropes of carbon nanomaterials, formed due to the different possible hybridization states of carbon, include fullerenes, carbon nanotubes (CNTs), and graphene (**Figure 5**)[85]. Fullerenes, characterized by a hollow spherical arrangement of five and six carbon rings, commonly referred to as a zero-dimensional structure, have been extensively studied for their optical and photonic-related applications due to their unique morphology. Carbon nanotubes, a one-dimensional hollow cylindrical structure, and graphene, a two-dimensional flat sheet of hexagonally packed carbon atoms, have been of great interest for use in polymer composites, electronics, and energy harvesting and storage devices due to their enhanced thermal and electrical properties resulting from the unique sp2 hybridized graphitic structure[85,86].

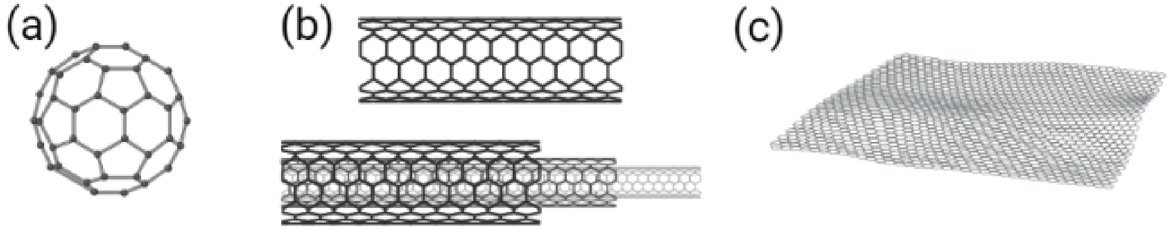

Figure 5. Structural representation of common Carbon allotropes including (a) fullerenes, (b) SWCNT and MWCNT, and (c) graphene. Image created with BioRender.

The one-dimensional, tubular morphology of CNTs was first recognized by S. Iijima in 1991, in a by-product of the fullerene synthesis by arc discharge[87]. High resolution electron micrographs were able to show to presence of concentric lattice tube-like structures, deemed multi-walled carbon nanotubes (MWCNTs), shown in **Figure 6**. The separation between concentric tubes was found to be approximately 0.34 nm, matching that found in bulk graphite. Two years later in 1993, tubes formed with a single layer in soot-like deposits from arc-discharge were discovered, deemed single-walled carbon nanotubes (SWCNTs)[86]. Further research efforts led to the understanding that the desired properties (mechanical, electrical, thermal, etc.) of carbon nanotubes could be optimized based on the growth techniques used to produce them[88]. Historically, arc discharge and laser ablation techniques were used to produce CNTs, but recent developments in chemical vapor deposition (CVD) have advanced the inexpensive scale-up of production[89]. With increased production possible, CNTs have been more widely used as a conductive filler in polymer composites, deemed "smart" composites, for a variety of sensing and energy harvesting techniques, with commercial viability.

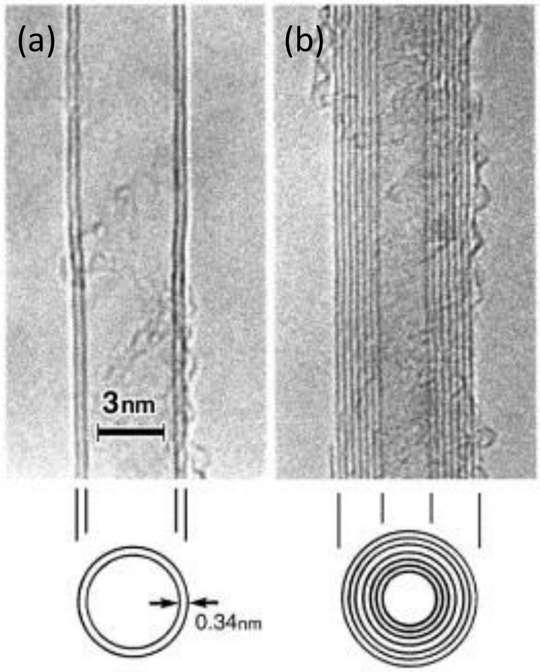

Figure 6. Electron micrographs of MWCNTs with a cross section view illustrated below with (a) two rings and (b) seven concentric rings. Parallel dark lines correspond to the (002) lattice images of graphite. Reprinted Carbon nanaotubes: past, present, and future, 323/1-4, Sumio Iijima, Pages No. 1-5, Copyright (2002), with permission from Elsevier[87,90].

Classified by their one dimensional structure, CNTs are often described at the molecular level as a graphene sheet seamlessly rolled up into hollow cylindrical tubes (SWCNTs), with the possibility for multiple sheets to be wrapped concentrically (MWCNTs)[22]. Historically, SWCNTs have diameters on the order of a few angstroms to tens of nanometers, with MWCNT diameters possible up to a few hundred nanometers. In both forms, CNT length can vary from hundreds of nanometers to a few mm, resulting in their high aspect ratio[91]. Beyond their dimensional classification, the chirality, or the angle at which the graphene sheets wrap into a tube-like structure, has a significant impact on the resulting electrical conductivity, with properties varying from semi-conducting to metallic with an electrical conductivity as high as 5000 S/cm, shown in **Figure 6**[92]. Their high conductivity and aspect ratio ensure high charge transport capabilities within composite structures. The unique arrangement of carbon atoms and resulting porosity and high surface area also lend CNTs to be excellent additives in a variety of composite materials. CNTs also possess high thermal conductivity (6000 Wm/K), thermal stability (stable up to 2800 C in vacuum), and good mechanical properties (tensile strength 45 billion Pa)[93]. This combination of unique properties have made CNTs extremely attractive as a filler material in a variety of composite materials for multifunctional sensing applications.

1.6 Cellulose composites for energy storage applications

With the ever increasing demand of electrical energy, energy storage technologies are steadily becoming more crucial in advanced electrical power systems. Recently, dielectric capacitors have gained significant interest in the literature due to their ability to rapidly release energy, intrinsically high power density and extended life span[26–28]. Dielectric energy storage is defined as the storage of electrical energy due to the polarization of a material in the presence of an external electric field, causing the distribution of positive and negative charges to orient themselves on opposite electrodes, as demonstrated in **Figure 7**[94].

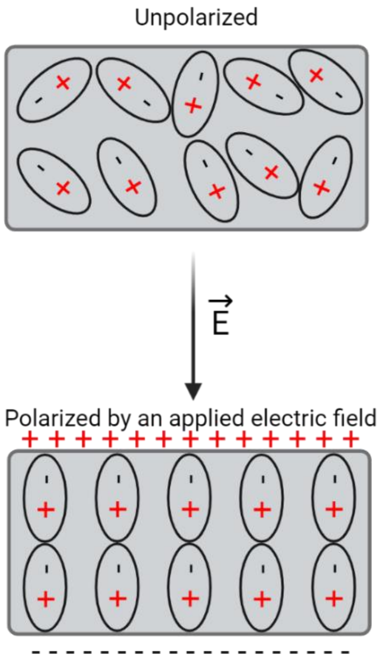

Figure 7. Dielectric polarization schematic. Depiction of a dielectric material being polarized by an applied electric field. Image created with BioRender.

The versatility of dielectric materials is commonly defined by the energy density they can store, calculated by

$$U_e = \int EdD = \varepsilon_0 \int Ed_{\varepsilon_r}E \qquad \textit{Eqn 1.}$$

where E represents the electric field strength and ε_r denotes the dielectric relative permittivity, both of which are key metrics in assessing the applicable range in which dielectric devices can be optimally employed[95]. Materials with high breakdown strengths are increasingly being investigated for their high energy density capabilities at high electric field strengths, whereas materials with increased permittivity remain more beneficial for smaller and more portable wearable electronics[95]. To accommodate a variety of energy storage applications, recent research has focused on improving the energy density storage of new materials for use in both low and high applied electric field applications.

Compared to traditionally employed inorganic materials commonly studied as dielectrics for their insulating properties, high breakdown strength, and superior dielectric constants, such as barium titanate ($BaTiO_3$), boron nitride (BN) and zinc oxide (ZnO), polymer based dielectric systems are gaining considerable interest in recent literature reports. Polymers are becoming more attractive due to their high breakdown strengths, flexibility, and ease of processing capabilities making commercialization more viable[26,96]. However, limited success in achieving both sufficiently high permittivity and breakdown strength have limited polymer use on their own. Composite structures where inorganic fillers of typical high dielectric strength materials (i.e. $BaTiO_3$, BN, ZnO) are embedded in a polymer matrix have therefore attracted attention in recent years, capitalizing on the flexibility and breakdown strength of a polymer matrix and the intrinsic permittivity of the ceramic fillers[97,98]. In spite of some success demonstrated by inorganic filler-polymer composites, most studies have reported a tradeoff in dielectric permittivity and breakdown strength, as high densities of filler nanoparticles and large dielectric and physiochemical differences between filler and matrix material lead to inadequate distribution of nanoparticles within the polymer matrix and localized electrical fields causing breakdown[26,99].

Composites comprised of two or more polymeric components have thus gained significant interest as an alternative dielectric materials in more recent years. Similar solubility and chemical structure allow for easier processing conditions and enhanced dispersion quality throughout the composite fabrication process. In the past, high breakdown strength and low loss polymers, such as polycarbonate (PC) and polyethylene terephthalate (PET) have been used in tandem with high permittivity poly(vinylidene fluoride) (PVDF)[26,100,101]. Recently, the immersion of cellulose as a sustainable polymeric alternative has gained significant traction in the literature for energy storage technologies. Due to the loosely bound hydroxyl and carboxylate groups on the surface of cellulose fibers, when exposed to an electric field, polarization, or the rotation and alignment of charged functional groups, occurs which allows for charge to be stored. As the degree of polarization of cellulose is highly dependent on its structure and the extraction technique used to isolate it, a variety of different types of cellulose have been evaluated as a bio-degradable and inexpensive alternative, with a relatively high permittivity[31,102]. Reports have focused on both original cellulose microfibers[103], and cellulose nanofibrils[30,32,33], as well as cellulose-based composites of inorganic fillers[98,104], organic fillers[105,106], and other polymer blends[107–109]. Additionally, cellulose offers improvements in processing conditions for dielectric materials as it is soluble in water, reducing the need for harsh chemicals and energy intensive fabrication techniques. Combined with its natural abundance, flexibility, and inexpensive processing techniques, cellulose composites offer a compelling alternative to traditional polymeric dielectric materials currently driving the industry.

II. Materials and Methods

In this chapter the materials and methods used to fabricate all materials presented throughout this work, including conductive paper nanocomposites and cellulose nanofibril (CNF) films, will be described in detail. The different characterization and analysis techniques used to assess resulting material microstructure and electrical properties will also be presented.

2.1 Materials

2.1.1 Conductive paper nanocomposites

Unbleached Kraft softwood (SW) pulp (50% Douglas Fir, 50% Hemlock), provided by Port Townsend Paper mill, bleached Kraft SW pulp (50% Douglas Fir, 50% Hemlock), provided by WestRock, and bleached hardwood (HW) pulp (50% Cottonwood, 50% sawdust), provided by Boise Cascade Company, were received in a dried mat form after chipping, screening, washing, and digesting. Pristine and hydroxyl-functionalized multiwalled carbon nanotubes (CNTs) with length in the range of 10-20 μm and a mean diameter of 50 nm, synthesized by chemical vapor deposition and purified using acid reflux, were purchased from CheapTubes Inc. The hydroxyl-functionalized CNTs, defined henceforth as CNT-OH contain ~0.7wt% of OH groups per the manufacturer's technical data. Alkali lignin (AL, 99%) and cetyl-trimethylammonium bromide (CTAB, 99%) dispersants were obtained from Tokyo Chemical Industry Co. and Amresco, respectively. Cationic retention aid, cationic polyacrylamide (CPAM, Percol 3025), was obtained from BASF. All chemicals were used as received without any further treatment unless otherwise specified.

2.1.2 Cellulose nanofibrils (CNF)

Chemicals used for the production of nanocellulose fibrils (CNF) from bleached Kraft SW pulp fibers (WestRock) included, sodium bromide and sodium hypochlorite (12.5 w/w%), purchased from VWR, and 2,2,6,6-Tetramethylpiperidine (TEMPO), purchased from Tokyo Chemical Industry Co.. Prior to use in the CNF oxidation reaction, TEMPO was first dispersed in DI water at a 9.6 mg/mL solution. Hydrochloric acid (HCL, 1M), used as received, and sodium hydroxide (NaOH, 1M), diluted to 0.5M prior to use, were purchased from Fischer Scientific.

2.1.3 Cellulose nanofibril (CNF) films

In addition to the chemicals listed above for the production of the CNF, Polyvinylidene difluoride (PVDF) was provided by Arkema (Kynar ARC latex, aqueous) with an estimated initial solids concentration of 44 wt% and a fluoropolymer: resin ratio of 70:30. Polyvinyl alcohol (PVA) was purchased from Sigma Aldrich (CAS number 9002-89-5) with a molecular weight of 89,000-98,000 g/mol and a degree of hydrolysis of 99+%. Prior to use, PVA was dispersed in DI water at 5 wt%, and stirred at 60 °C for ~2 hours, or until all PVA had dissolved.

2.2 Experimental Methods

2.2.1 Preparation of CNT-surfactant dispersions

Prior to bonding with cellulose fibers, the individualization of CNT aggregates is critical to provide large numbers of charge transport routes throughout the composite, such that a low percolation threshold for electrical conductance can be achieved. A variety of surfactants were used throughout this work to individualize CNTs in solution prior to bonding with additional materials (i.e. pulp fibers).

In general, a selected surfactant was added to ~500 mL of deionized (DI) water and mechanically stirred (magnetic stir plate) for 5 minutes, followed by bath sonication for 5 minutes. A desired amount of CNTs were then added to the aqueous surfactant solution under constant stirring for 5 minutes, followed by double acoustic irradiation, combining both bath and probe sonication[110], for 20 minutes. The water in the sonic bath was intermittently replaced by cold water to maintain the temperature below 30°C throughout the sonication process. The amount of CNTs and surfactants were adjusted to maintain a CNT: surfactant ratio of 1:1, 2:1, or 3:1, and a final CNT loading of 2.5, 5, 10, 15, or 20 wt% for 40, 60, 80, or 100 g/m^2 paper nanocomposites.

2.2.1a Aqueous CNT dispersions used in Chapter 1 study

In the study described in Chapter 1, all aqueous CNT solutions were prepared at a 2:1 CNT: surfactant ratio where AL was the only surfactant used, and both pristine and hydroxyl-functionalized CNTs were studied. The content of CNTs was adjusted to obtain an OD CNT loading of either 2.5 or 10 wt% in the final nanocomposite, and a resulting grammage of 60 g/m^2.

2.2.1b Aqueous CNT dispersions used in Chapter 2 optimization study

In the optimization study described in Chapter 2, all aqueous CNT solutions were prepared using hydroxyl-functionalized CNTs (CNT-OH) and as-prepared TEMPO-oxidized cellulose nanofibrils (CNF) as the dispersant. The contents of CNTs and CNFs were adjusted to maintain either a 1:1, 2:1, or 3:1 CNT: CNF ratio, with a final nanocomposite CNT content of 5, 10, or 15 wt% and a grammage of either 40, 60, 80, or 100 g/m^2. For example, when preparing a solution for a 15 wt% nanocomposite at a 2:1 ratio and 60 g/m^2 grammage, 0.09 g of CNF (volume needed to achieve 0.09g dependent upon measured CNF solution concentration) was added DI water to achieve a ~500mL solution, followed by the aforementioned mechanical stirring and bath sonication, before

0.18g of CNT-OH were added, followed by the previously described double acoustic irradiation procedure.

2.2.1c Aqueous CNT dispersions used in Chapter 3 pilot-scale study

The general procedure for the preparation of aqueous dispersions of CNTs was adapted from the batch-scale to accommodate the larger volumes needed for the scale-up study described in Chapter 3. For the pilot-scale production of paper nanocomposites, aqueous CNT solutions were prepared based on calculations taking into account desired machine speed, paper grammage, and a final CNT loading of 20 wt% in the nanocomposite. For enhanced nanoparticle retention during continuous processing, both AL, an anionic surfactant, and CTAB, a cationic surfactant, were used to achieve a layer-by-layer nanoassembly technique, relying on alternating streams of oppositely charged CNT solutions. For flexibility during the pilot-scale production processes, 2/3 of the aqueous CNT dispersions were prepared using AL, and 1/3 was prepared using CTAB. Regardless of surfactant used, aqueous CNT solutions were prepared at a solids content of 7.5 wt% and a 2:1 CNT: surfactant ratio. Based on volume limitations due to the size of the double acoustic irradiation system described above, dispersions could only be prepared in batches of up to 2,000 mL of DI water. To accommodate these restrictions, multiple aqueous CNT dispersions were prepared and combined into one final AL, and one final CTAB based dispersion after the double acoustic irradiation processing step, and magnetically stirred in tanks connected to the pilot-scale web former until use. The breakdown of how smaller aqueous CNT dispersion were prepared prior to combining is outlined below:

- CNT:AL dispersions:
    - Batch 1: 2,000 mL DI water + 100 g CNT-OH + 50 g AL
    - Batch 2: 2,000 mL DI water + 100 g CNT-OH + 50 g AL
    - Batch 3: 1,333.4 mL DI water + 66.67 g CNT-OH + 33.33 g AL
- CNT:CTAB dispersions:
    - Batch 1: 2,000 mL DI water + 100 g CNT-OH + 50 g CTAB
    - Batch 2: 666.6 mL DI water + 33.33 g CNT-OH + 16.67 g CTAB

2.2.2 TEMPO-mediated oxidation of bleached softwood pulp

Cellulose nanofibrils (CNFs) were synthesized following a previously described TEMPO-mediated oxidation process (TEMPO/NaBr/NaClO), on the basis of 5 mmol NaClO per gram of bleached softwood pulp, followed by mechanical defibrillation.[50,54] Briefly, bleached softwood pulp was first soaked in 3 L DI water for 24 hours under mechanical agitation. Sodium bromide (NaBr) was added to the pulp (10 w/w %) followed by a 9.6 mg/mL aqueous solution of TEMPO under constant agitation. A 15mmol solution of sodium hypochlorite (NaClO, 5mmol/g pulp) was then slowly added to the pulp slurry and thoroughly mixed. Sodium hydroxide was then added drop wise to the pulp until a pH of 10 was maintained for at least 30 minutes, and a color change from yellow to white was observed, or until a desired oxidation time was reached (i.e. 5 minutes, 30 minutes, 1hour and 45 minutes, 3 hours). HCl was then added drop wise until solution pH was maintained at 7 for at least 30 minutes, stopping the oxidation reaction. The cellulose solution was then centrifuged for 10 minutes at 5,000 rpm, and the precipitate was poured into dialysis bags and stored in DI water. Dialysis water was exchanged daily until a solution conductivity of <1 μS was maintained. The washed fibrils were then removed from the dialysis bags and DI water was added up to a total volume of 800 mL. A blender was used to liquefy the solution, 400 mL at a time, for

30 minutes, or until a smooth solution consistency was reached. The blended pulp solution was then probe sonicated at 100% amplitude for 2 minutes. The sonicated CNF was then centrifuge for 15 minutes at 5,000 rpm, and the supernatant was collected for use. A representative schematic of the TEMPO-mediatited oxidation procedure is depicted below in **Figure 8**.

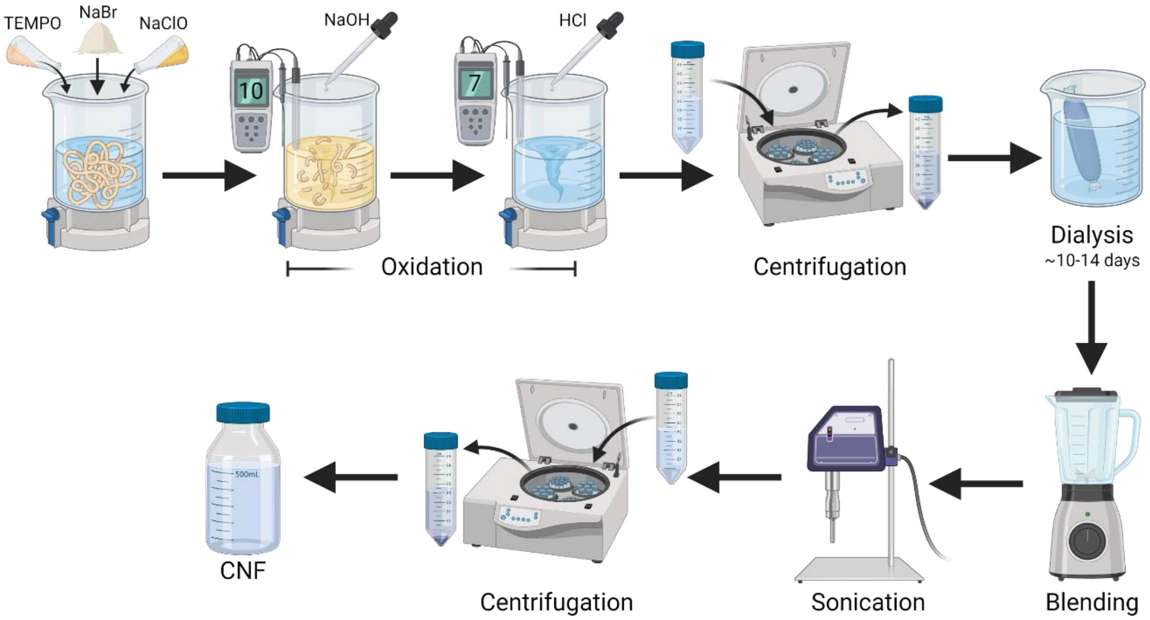

Figure 8. Representative schematic of the TEMPO-mediated oxidation process used to prepare CNF. Image created with BioRender.

After CNF was prepared, the solution concentration was determined based on oven drying a known volume of solution overnight at 60°C and recording the resulting dried mass (g/mL). Conductometric titration was then used to measure the carboxylate content of CNF (charge density), described in detail in Section 2.3.1a of this text.

2.2.3 Preparation of aqueous cationic polyacrylamide (CPAM) solutions

Kraft pulp (used throughout this work) is known to generate fibers with a negative surface charge due to the presence of hydroxyl and carboxyl groups. Since the as-prepared CNT dispersions made with AL also carrying a negative surface charge due to the anionic nature of AL, a cationic polymer was utilized in the study described in Chapter 1 to fix the CNTs to the pulp fibers. Aqueous solutions of CPAM were prepared in bulk by first soaking a 0.06 g of CPAM in ~ 1 mL of acetone for 30 seconds, and then mixing in 1L of DI water at 50°C on a hot plate stirrer for ~45 minutes, or until all CPAM crystals had dissolved. A volume of 200 mL of the as-prepared CPAM solution was then added into the pulp solution to obtain paper nanocomposites with a CPAM content of 1 wt% (60 g/m^2 basis). Pulp fiber and CPAM solutions were then mixed on a hot plate stirrer at 50°C for 30 minutes prior to the addition of aqueous CNT-AL solutions as previously described.

2.2.4 Pulp stock preparation

As provided pulp (30g, OD mat form) was dispersed in 2000 mL of DI water (1.2% consistency) using a disintegrator (Messmer Instruments Limited: Disintegrator MK.3C) operated at 3000 rpm. Water was removed to achieve a consistency of 10% before refining in a Paperindustriens Forsknings-Institut (PFI) mill at 15 Kg beating load, until a desired freeness of 250 mL, determined using a Mitchell CANADA: Freeness Tester, was achieved, (Canadian Standard Freeness, method TAPPI T227). The refined pulp stock solution was diluted to 0.3% consistency and stored for at least 24 hours before processing.

2.2.5 Batch-scale production of conductive paper nanocomposite handsheets

The conductive paper nanocomposite handsheets, dubbed “smart” paper, were prepared following the TAPPI T-205 method. A desired volume of pulp stock solution was heated to 50 °C on a hot plate under constant stirring. If CPAM was used in the handsheet preparation (Chapter 1 study), it was added to the pulp solution here and mixed for 30 minutes. The as-prepared CNT-surfactant solution was then slowly added to the pulp solution and thoroughly mixed for 30 minutes on a magnetic stir plate. The combined CNT-surfactant-pulp solution was then slowly poured into a handsheet mold (Essex International Inc. Custom Machinery), and pressed and dried according to TAPPI T-205 standards. The proportions of cellulose, CNT, and surfactants were adjusted to obtain a paper with a CNT loading of 2.5, 5, 10, or 15 wt% and a grammage of 40, 60, 80, or 100 g/m^2. All prepared hand sheets were stored for at least 48 hours under controlled humidity conditions of 23°C and 50% relative humidity (RH) prior to testing (ASTM D685). A representation of the preparation procedure used to prepare paper nanocomposite handsheets at the batch scale is outlined below in **Figure 9**.

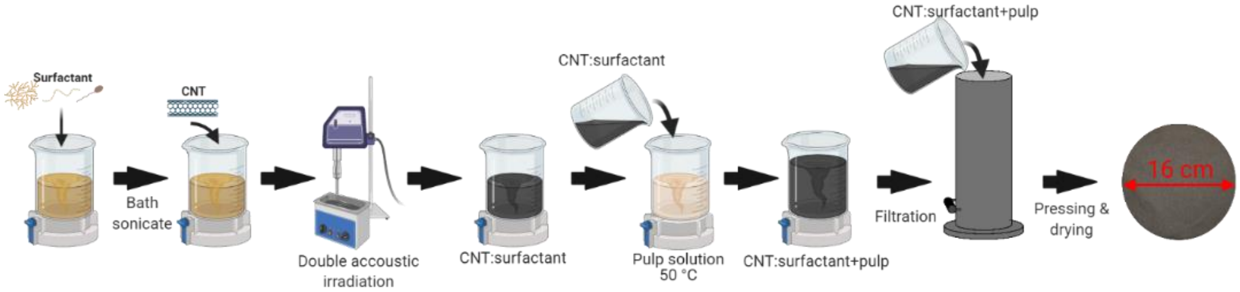

Figure 9. Representative schematic of batch scale production of nanocomposite handsheets. Image created with BioRender.

2.2.5a Handsheet preparation method used in Chapter 1

Following the general guidelines described in the aforementioned preparation method, handsheets used in the study described in Chapter 1 were prepared at a final paper grammage of 60 g/m^2 (1.2 g OD), using both bleached and unbleached pulp fibers and pristine and hydroxyl-functionalized CNT contents of 2.5 and 10 wt%. All handsheets were prepared at a 2:1 CNT: surfactant ratio, where AL was the only surfactant studied. Handsheets prepared in this study also included a 1wt% CPAM solution, combined with the pulp fibers prior to the addition of aqueous CNT-AL solutions.

2.2.5b Handsheet preparation method used in Chapter 2 optimization

For the optimization study described in Chapter 2, paper nanocomposites were prepared at a variety of grammages (40, 60, 80, and 100 g/m^2) and CNT: surfactant ratios (1:1, 2:1, and 3:1). In all handsheets, bleached Kraft SW pulp and hydroxyl-functionalized CNTs were used. CNF, prepared at a 3 hour oxidation time, was used as the surfactant throughout this study.

2.2.6 Continuous pilot-scale production of conductive paper nanocomposites

Paper nanocomposites were produced on a Noble and Wood Machine Company (1967) pilot scale paper machine with a 31.75 cm deckle, operated at ~3.2 m/min, to produce approximately 70 meters of composite "smart" paper in a continuous process. Paper composition was adapted from hand sheet studies to maximize carbon nanotube retention during continuous production, while maintaining rapid dewatering during sheet formation, utilizing a unique binding chemistry combining both anionic and cationic surfactants to achieve a layer-by-layer assembly technique, as described in section 2.2.1c.

A combination of SW and HW pulp was first prepared in a 75:25 ratio at 0.35% consistency and mixed for 24 hours prior to sheet formation. Pulp and as-prepared CNT-surfactant (CNT-AL, CNT-CTAB) solutions (5 wt%, 2:1 CNT: surfactant ratio) were combined immediately prior to sheet formation. Desired CNT content and grammage were controlled by adjusting the wire screen speed (3-3.5 m/min), and fan (150-250 mL/min) and stuff pump (15-30 L/min) flow rates. Dewatering is achieved by subsequent pressing at 50 PSIG and drying at 80°C. The resulting paper nanocomposite was then wrapped around a 10-cm diameter roll before being unwound and cut into sheets of 30 cm x 80 cm using an automated sheet slicer (Kunshan Dapeng Precision Machinery Co., Ltd., DP-360CQ).

2.2.7 Fabrication of cellulose nanofibril (CNF) films

CNF based films, prepared with varying PVDF contents, were fabricated by an aqueous solution casting process, and combined with a layer-by-layer assembly technique. Single layer, bilayer, and sandwich structure films were prepared for this study, as described below. All as-prepared films were then treated by a hot pressing technique (Rosin Tech. Products).

2.2.7a Preparation of CNF and CNF/PVDF solutions

Pure CNF solutions were fabricated by first magnetically stirring a desired volume of as-prepared TEMPO-oxidized CNF for 2 hours, followed by 45 minutes of bath sonication. The volume of CNF was adjusted based on the measured solution concentration, to achieve a final OD film mass of 0.25 g, resulting in an approximate film thickness of 29.6±2.7 μm.

Composite CNF/PVDF films were prepared following the same procedure as the pure films, with the addition of stirring 10 wt% of PVDF (68.9 μL) into the aqueous CNF solution immediately prior to the mixing and bath sonication processing step. For both pure and composite films, CNF prepared at all oxidation times studied (5 minutes, 30 minutes, 1hour 45 minutes, and 3 hours) were studied. The volume of aqueous PVDF based on a 10 wt% content was determined based on the technical specifications of the solution estimated by the supplier (Arkema), outlined here:

Table 1. Composition of aqueous PVDF (Kynar ARC) provided by Arkema

Material (aq)	Density (g/mL)	Solids (wt%)	PVDF content of solids (wt%)
Kynar ARC	1.178	44	70

2.2.7b Preparation of PVA and PVA/PVDF solutions

For multi-layered films, PVA and PVA/PVDF solutions were prepared for the additional layers. First, PVA was dispersed in DI water (5 wt%) by mechanically stirring at 50 °C for ~1 hour, or until all PVA crystals had dissolved. Pure PVA solutions were then prepared by first adding 1.54 mL of the as-prepared PVA solution (5 wt%) to 5.46 mL of DI water, to achieve a combined 7 mL solution at a solids content of 1.1 wt%. The aqueous PVA mixture was magnetically stirred for 2 hours at room temperature, followed by 45 minutes of bath sonication.

Combined PVA/PVDF solutions were prepared in a similar manner, maintaining an overall solids content of 1.1 wt% in the solution, taking into account both PVA and 3 wt% of PVDF in the solids, and a total solution volume of 7 mL. A desired volume of PVA (1.494 mL, 5 wt%) was first stirred into 5.49 mL of DI water for five minutes, followed by the addition of 6.37 μL of PVDF. The combined PVA/PVDF solution was then magnetically stirred at room temperature for 2 hours, followed by 45 minutes of bath sonication, yielding an opalescent solution when fully mixed.

2.2.7c Single layer CNF film preparation method

Prepared CNF solutions, pure CNF or CNF/PVDF, were poured into 80x40 mm glass crystalizing dishes (Pyrex), and oven dried at 50°C for 32 hours. The crystallizing dishes were then removed from the oven and continued to dry under an infrared lamp in air for ~4-6 additional hours, rotating the dish every ~30 minutes, or until the film appeared completely dry. The dried films were then removed from the crystalizing dish, and the rough edges were trimmed off prior to hot pressing. A simplified schematic of the film fabrication process is shown in **Figure 10**.

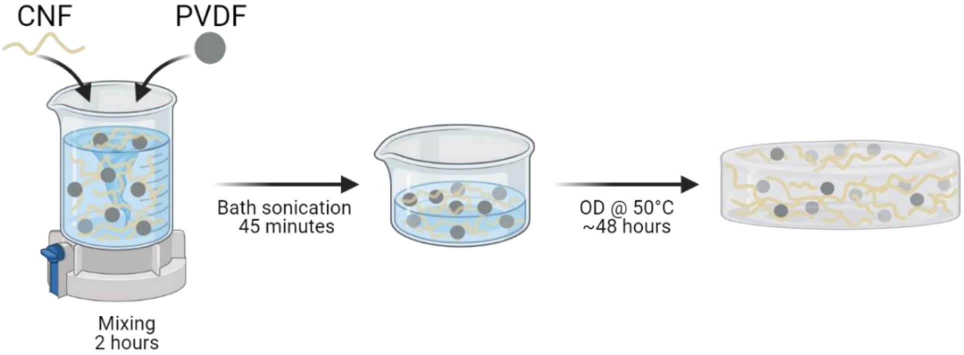

Figure 10. Representative schematic of single layer composite CNF/PVDF film preparation method. Note: pure CNF films are prepared the same way, but without the addition of PVDF nanoparticles shown here. Image created with BioRender.

2.2.7d Bilayer CNF film preparation method

Bilayer structure films were prepared by topping a CNF layer with a PVA based layer, as indicated in the simplified schematic in **Figure 11** below. Pure CNF or composite CNF/PVDF solution was first poured into an 80x40 mm glass crystalizing dish (Pyrex), and oven dried at 50°C for 32 hours. After the first 32 hours in the oven, the semi-dried CNF solution appeared gel-like with a relatively firm film on the top. The dish was then removed from the oven and a 7mL solution of either pure PVA or PVA/PVDF, was gently pipetted onto the top of the CNF layer, taking care to minimally disrupt the surface of the partially dried layer. The bilayer films were then left to finish drying under an infrared lamp for ~ 18-24 more hours, or until completely dry. Dishes were rotated every 30 minutes or so, as needed, to ensure even drying across the surface of the film. Bilayer films were then removed from the crystallizing dish, and the rough edges were trimmed prior to hot pressing.

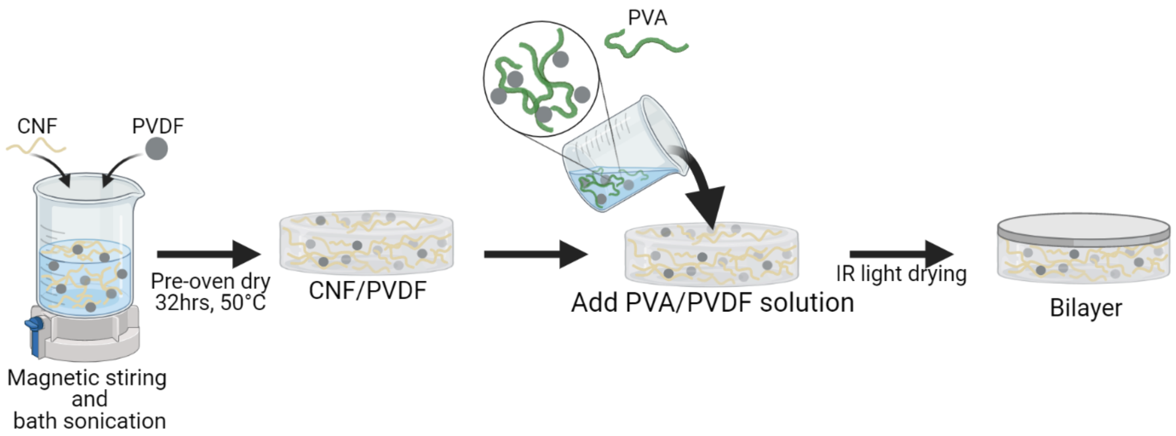

Figure 11. Representative schematic of bilayer film preparation method. Note, the added PVA/PVDF solution also indicates a pure PVA solution, as both pure PVA and composite PVA/PVDF solutions were added as the top layer in this study. Image created with BioRender.

2.2.7e Sandwich structure CNF film preparation method

Sandwich structure films were prepared by layering a PVA based bottom layer, followed by a CNF middle layer, and topped with another PVA based layer, as indicated in the simplified schematic presented in **Figure 12**. A 7mL PVA or PVA/PVDF solution was first cast into an 80x40mm glass crystalizing dish, and dried under an infrared lamp for ~1.5 hours, or until there was no visible wet solution remaining. The crystalizing dish was rotated and shaken every 15 minutes through the drying time to ensure even drying within this base layer. As-prepared CNF solutions (pure CNF, CNF/10wt% PVDF) were then slowly poured on top of the base layer, and oven dried at 50°C for 32 hours. Films were then removed from the oven and a final 7 mL top layer solution (PVA, PVA/ 3wt% PVDF) was slowly pipetted on top, taking care to let the solution run down the sides of the crystallizing dish, so as to not disturb the middle CNF layer. Sandwich structure films were then left to finish drying under an infrared lamp for ~18-24 more hours, or until completely dry. Dishes were rotated every 30 minutes or so, as needed, to ensure even drying across the surface of the film. Sandwich films were then removed from the crystallizing dish, and the rough edges were trimmed prior to hot pressing.

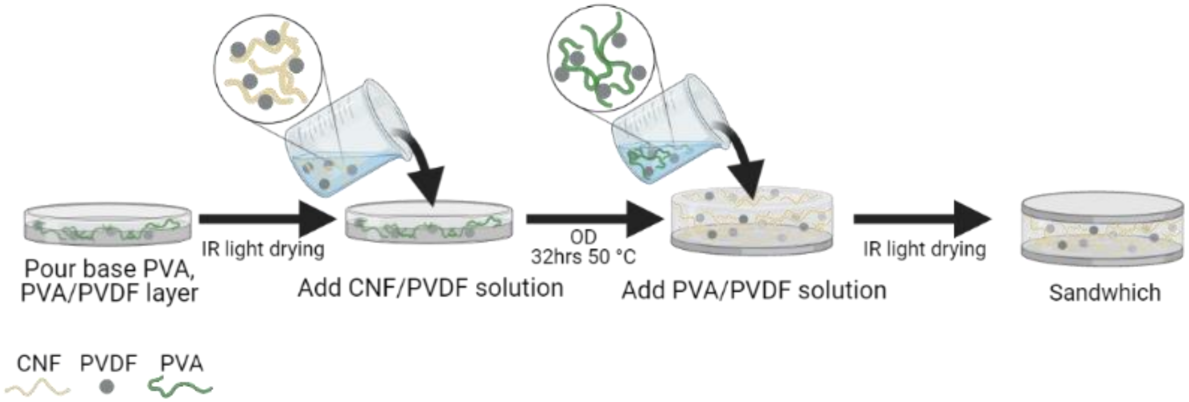

Figure 12. Representative schematic of sandwich structure film preparation method. Note, the added PVA/PVDF solution also indicates a pure PVA solution, as both pure PVA and composite PVA/PVDF solutions were added as the top layer in this study. Image created with BioRender.

2.2.8 Hot pressing

A Rosin Tech Products hot press (Rosin Tech Smash) was used to hot press as-prepared CNF composite films. Films were first sandwiched between two layer of Kapton film (Professional Plastics), held together by Kapton tape, before being placed on the bottom metal platen in the hot press. Once the hot press had reached temperature, the metal platens were pressed together and held at 100 °C for 5 minutes. Films were then removed from the press and stored until further testing.

2.3 Characterization Techniques

This section will describe the different characterization techniques used throughout this work to gain insight into the chemical composition, morphology and microstructure, and physical and electrical properties of the as-produced conductive paper nanocomposites and CNF dielectric films.

2.3.1 Characterization of morphology, microstructure and chemical composition

2.3.1a Charge density

Prior to use in paper nanocomposites or films, the morphology and chemical composition of CNF was studied. As the surface charge of CNF directly effects their ability to successfully disperse CNTs in aqueous solution, conductometric titration was used to determine the charge density of CNF, an indication of the quantity of negatively charged carboxylate ($COO^{-}Na^{+}$) groups on the surface of each nanofibril. Briefly, 50 mL of 0.1 wt% CNF dispersion and 1 mL of hydrochloric acid (0.1M) were mechanically stirred for 10 minutes to protonate carboxylic acid groups on the CNF surface. Sodium hydroxide (NaOH, 0.02M) was then added to the suspension in 100 µL allocates, and the solution conductivity was measured (Oakion Cond 6+ TDS 6+ Salt 6+ meter) after each addition. The volume of NaOH needed to stabilize the charge due to the protonated COOH groups was calculated, yielding the concentration of COOH per gram of CNF (mmol COOH/g CNF). The volume of NaOH needed to stabilize the reaction is determined by plotting the measured solution conductivity (µS) as a function of volume of NaOH (µL) added, and extracting the equations for the three distinct regions (decreasing slope, slope~0, and increasing slope) of the plot. The equation for the decreasing slope portion is set equal to the equation of the portion with a slope~0 to determine the initial NaOH volume. The same is done for the portion of the plot with an increasing slope and that of a slope~0 to determine the final volume of NaOH. The volume of NaOH needed to protonate the carboxylate groups on the fibrils surface is calculated by subtracting the starting volume from the final volume. The moles of NaOH are calculated based on the knowledge that NaOH was added at 0.02M. Since the moles of NaOH and COOH (COONa) are at a 1:1 ratio, this also determines the moles of carboxylate groups present.

From the starting volume (50 mL) and concentration (0.1 wt%) of CNF used in this experiment, the quantity of COONa groups present on the CNF can be determined.

2.3.1b Atomic Force Microscopy

Atomic force microscopy (AFM) was used to determine the morphology of individual nanofibrils. All AFM measurements were taken in tapping mode with a bluedrive photothermal excitation and a scan rate of 1 Hz (Asylum Research Cypher, ArrowUHF probes). Depending on the measured charge density, AFM samples were prepared in one of two ways, described below.

i. Samples with a charge density greater than ~0.5 mmol COOH/g CNF:

Mica discs (TedPella Inc., 12 mm) were first cleaved using scotch tape until a minimum of three full cleaves were achieved. CNF solution was diluted to 0.0005 wt% by first magnetically stirring in DI water for 5 minutes, followed by 10 minutes of bath sonication, immediately prior to sample preparation. Prepared CNF dilutions were then drop cast (10 µL) onto freshly cleaved mica discs, within 10 minutes of being cleaved, and left to air dry for ~1 hour before being imaged.

ii. Samples with a charge density less than ~0.5 mmol COOH/g CNF:

Low charge density fibrils with less surface charge resulted in severe aggregation on the mica discs when prepared following the aforementioned AFM preparation method, as they were unable to remain as individualized in solution when drying. A new technique was adapted to help adhere individual CNF to the mica discs without aggregation, allowing for better imaging of individual fibrils. Mica discs (TedPella Inc., 12 mm) were first cleaved using scotch tape until a minimum of three full cleaves were achieved. Poly-L-Lysine (Advanced BioMatrix, 0.1 mg/mL) was removed from cold storage and allowed to come to room temperature (~30 minutes) before being drop cast (~75-100 µL) onto the freshly cleaved mica and left to sit for 10 minutes before being rinsed off in DI water and dried with forced air. Dilutions of CNF were prepared in the same way as described in AFM sample preparation technique a, where as-prepared CNF solutions were first magnetically mixed with DI water for 5 minutes, followed by 10 minutes of bath sonication to achieve a resulting dilution concentration of 0.0005 – 0.001 wt %, depending on the charge density. CNF dilutions were then drop cast onto the lysine treated mica discs (~50-75 µL), ensuring to wet the entire surface, and allowed to sit for 30 seconds before being rinsed off with DI water and dried with forced air.

2.3.1c Optical microscopy

Optical microscopy (Zeiss Axiocam ERc5s digital camera mounted on a Zeiss Axiolab light microscope) was used to study the morphology of individual cellulose pulp fibers when in the dry and wet states. Bleach Kraft SW pulp dispersions (~0.5mL, 0.3 % consistency) were drop cast on glass microscope slides and dried on a hot plate at 50 °C for approximately 30 minutes, or until pulp suspensions appeared dry. Prepared slides were then placed in the microscope and imaged in the dry state. Imaged pulp fibers were then subject to 0.5mL of liquid solutions (i.e. DI water, organic solvents), and allowed to soak for 60 seconds, after which time wet fibers were re-imaged using the microscope and camera. The glass slides were then re-dried on a hot plate at 50 °C for 30 minutes to ensure fibers had completely dried, and were re-imaged to assess the ability of swollen wet fibers to return to their original size. Optical microscopy measurements of dry, wet, and re-dried fibers were measured an average of 30 times to ensure statistical soundness in fiber diameter analysis. ImageJ software was used to analyze fiber diameter in the dry and wet states for all solvents tested.

2.3.1d Scanning Electron Microscopy (SEM)

The morphology of as-prepared paper nanocomposites and CNF films were examined using a scanning electron microscope (SEM, Sirion XL30). All samples were coated with a 4 nm layer of gold-palladium and observations were conducted under high vacuum conditions at an accelerating voltage of 5 kV. Paper nanocomposites were adhered to carbon tape on SEM stages, and the surface was imaged to assess composite morphology, and CNT distribution.

CNF films were first cryo-fractured by soaking in liquid nitrogen for 5 minutes before being broken with applied pressure from a razor blade, to achieve a clean fractured edge. Cryo-fractured film samples were then mounted vertically in the SEM, with the fractured edge facing up on a vertical stage, allowing for imaging of the films cross-section.

2.3.1e Raman Spectroscopy

Raman spectroscopy was used to analyze the interfacial properties of the fiberous paper nanocomposites. Raman spectra were recorded over the range of 800-1800 cm-1 with a spectral resolution of 1 cm^{-1} by a Reinshaw InVia Raman microscope equipped with a 785 nm laser. Samples were prepared by adhering either CNT-OH or conductive paper nanocomposites, prepared at a variety of CNT loadings and ratios, onto a small section of double sided tape on a glass slide. Samples were measured as-prepared without any additional treatment.

2.3.1f Fourier transform infrared spectroscopy (FTIR)

Interfacial interactions between all compounds in either the paper nanocomposites of CNF films were examined by Fourier transform infrared spectroscopy (FTIR). FTIR spectra were collected on a Shimadzu FTIR spectrophotometer with a resolution of 1 cm^{-1} in attenuated total reflectance mode, in which the background had already been subtracted from the obtained spectra. Paper nanocomposite and CNF film samples were used as-prepared and measure in the same way, in which the sample was placed on the sample stage and secured by tightening the top of the stage clamp onto the sample.

2.3.1g X-ray diffraction spectroscopy (XRD)

2D X-ray diffraction (XRD) was used to characterize the crystallinity index of cellulose pulp and CNF films, and gain insight into the reversibility of the hygroexpansion of cellulose fibers. Diffractograms were collected using a Bruker D8 powder diffractometer equipped with a high-efficiency Cu (1.54056 Å) anode at 50kV and 100 μA, a microfocus X-ray source, and a Pilatus 100K large-area 2D-detector. Angular scanning was measured at 11° increments from 0° to 90°. All samples were mounted directly onto a silicon dioxide wafer and held in place with double sided tape along the sample edges, taking care not to have any tape overhang into the measured area under the sample.

For dry XRD measurements, samples were used as-prepared. For wet XRD measurements, used to assess the reversibility of hygroexpansion of cellulose fibers within the nanocomposite, samples were first analyzed dry, then 10 μL of DI water was drop cast onto the center of the sample and left to soak for 60 seconds. Excess water was wicked away prior to loading into the XRD for measurements. Samples were then left to dry in air on a hot plate at 50°C for ~1 hour before being re-analyzed in the re-dried state, allowing for insight into the reversibility of the hygroexpansion of micro and nano cellulose fibers.

For paper nanocomposites produced on the pilot-scale, described in Chapter 3, XRD was used to estimate the orientation of crystalline cellulose pulp fibers in respect to the direction of the continuous flow. Scans were taken from a 2ϴ of 10 to 30° and the beam angle was rotated 10° after each scan from 0° (in direction of continuous flow) to 90° (perpendicular to direction of low). An azimuthal integration of the crystalline cellulose peak at 2ϴ =22.5° was performed in respect to the beam angle. *Equation 2* was then used to estimate the pulp fibers degree of alignment within the composite. Here, FWHM refers to the full width half maximum, in degrees, of the fitted integration peak.

$$f_c = \frac{180 - FWHM}{180} \qquad \textit{Eqn. 2}$$

Crystallinity index (CrI, %), a quantitative indicator of the crystallinity within a sample, was estimated using the Segal method[111,112], described below in *Equation 3*. Here, $I_{22.5}$ indicates the intensity of the crystalline peak at 2ϴ =22.5° and I_{18} indicates the amorphous peak intensity at 2ϴ =18°.

$$C_r I = \frac{I_{22.5} - I_{18}}{I_{22.5}} * 100\% \qquad \textit{Eqn. 3}$$

2.3.1h Optical absorption (UV-vis) spectroscopy

Optical absorption (UV-vis) spectroscopy quantifies the amount of light is absorbed as it travels through a sample compared to its blank counterpart, over a range of wavelengths in the electromagnetic spectra[113]. As the wavelength at which a particular material absorbs lights at is a function of the chemical composition, the amount of light absorbed is a direct indicator of both the type and amount of a chemical present in a specific material.

i. UV-vis spectroscopy on liquids:

As UV-vis spectroscopy is one of the most commonly used techniques to evaluate the quality of CNT dispersions, 1 wt% aqueous CNT dispersions were prepared at a 2:1 CNT: surfactant ratio, and used to compare dispersion capabilities of different surfactants. Aqueous CNT-OH solutions using CNF as the dispersant were prepared, and compared to dispersions using AL and two common petrochemical derived surfactants, sodium dodecylsulfate (SDS), cetyl-trimethylammonium bromide (CTAB) as the surfactants. Solutions were prepared by first dissolving a desired amount of surfactant in DI water, followed by bath sonication for 10 minutes. Nanotubes were then magnetically stirred into the solutions for 5 minutes, followed by double acoustic irradiation for 20 minutes. All UV-vis measurements were performed in quartz cuvettes at room temperature (25°C) using a Perkin Elmer Lambda 750 spectrophotometer operating in the 300-1200 nm range. Blanks were obtained as solutions of the dispersants in DI water (no CNTs) at the same dilution factor and prepared under the same conditions as the sample dispersions.

ii. UV-vis spectroscopy on solids:

Similarly to when used to assess CNT dispersion content and quality in the aqueous phase, optical absorption spectra of paper nancomposites prepared at various CNT loadings were recorded at spatial resolution of 1 nm with a Perkin Elmer Lambda 750 spectrophotometer equipped with a 100-mm InGaAs integrating sphere. Samples were used as-prepared without any additional treatment, and placed directly in front of the integrating sphere. Blanks were measured through the integrating sphere without any sample or other material present. CNF films were also measured using this same integrating sphere technique, and used to assess the transparency of the prepared films.

2.3.2 Characterization of physical properties

2.3.2a Caliper

The caliper of paper nanocomposites was measured by a Thwing-Albert Electronic Thickness Tester Model 2 at 7.3 psi in accordance with TAPPI T-411 standards. As-prepared paper nanocomposites were placed in between the upper and lower plates of the thickness tester and moved to a new location on the sample after each automatic measurement. To ensure statistical soundness and avoid the influence of temperature and moisture, five locations around each sample were measured under a controlled atmosphere (23°C and 50% RH).

2.3.2b Internal bond strength / Scotch Tape test

The internal bond strength of paper nanocomposites produced for the study presented in Chapter 1 were measured using a Scott bond tester following the TAPPI T-569 standard method. This standardized method defines a test that measures the energy required to rapidly delaminate a sheet-type paper specimen[114]. Paper nanocomposite samples were sandwiched between two pieces of double sided tape and pressed between a flat metal anvil and an aluminum platen. A pendulum was released and impacted the top inside surface of the platen, causing it to rotate and split the nanocomposite sample in the thin ‘Z’ direction. The energy absorbed from splitting the sample is calculated by measuring the peak excess swing on the pendulum. To ensure statistical soundness and avoid the influence of temperature and moisture, five samples from each type of nanocomposite were measured under a controlled atmosphere (23°C and 50% RH).

In the optimization study described in Chapter 2, the Scotch-tape peeling test was employed as a visual representation of the strong interfacial interactions achieved between the cellulose pulp fibers and the CNT-OH additives. Paper nanocomposite samples were cut into 4 cm x 4 cm square section and adhered at one end to a flat surface. A 4 cm x4 cm section of 3M Scotch was then evenly pressed onto the paper surface. After three minutes the tape was quickly ripped off at an approximately 30° angle to the paper at a constant speed. Each sample was subject to five peeling cycles to determine the progression of the interfacial properties after repeated applied stresses. The thickness of the sample (dig micrometer brand?) and in-plane electrical resistance (Keithly 2450 voltage current meter, 2-point probe mode) were measured before and after each peeling cycle. A representative schematic of the testing set-up is portrayed in **Figure 13**.

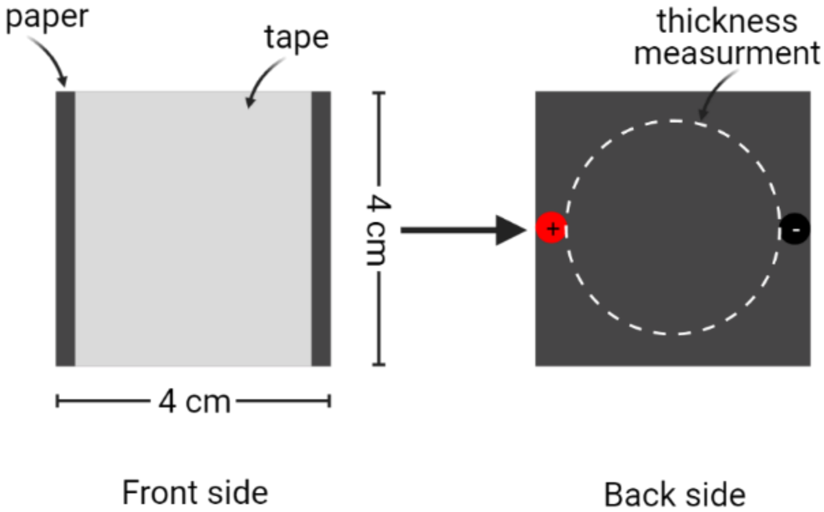

Figure 13. *Scotch tape test*. Representative testing schematic of Scotch tape test on conductive paper nanocomposite samples. Black and red circles on the back side of the tested sample indicate locations where in-plane electrical resistance measurements were taken before and after each peeling cycle. Image created with BioRender.

2.3.2c Tensile Strength

A tensile tester (Thwing-Albert Vantage^{TM}-10) was employed to measure both dry and wet tensile strengths of the different batch-scale produced paper nanocomposites, as well as the dry tensile strength of the pilot-scale produced nanocomposites described in Chapter 3. Strips of paper were cut to 25 mm x 180 mm dimensions and stored in a controlled atmosphere (50% RH, 23°C) for 24 hours prior to testing. For dry tensile tests, paper strips were vertically clamped into the tensile machine at either end, and were run until fracture was reached. A minimum of three replicates were measured for statistical soundness.

For wet tensile tests, depicted in **Figure 14**, paper strips were folded in half lengthwise around the metal rod of a Finch cup and clamped together at the top of the strip. Paper strips were them immersed in DI water for 10 seconds prior to tensile testing. The wet strength retention, defined as the ratio of the tensile strength of a paper in the wet state to that of the dry state, was then calculated (*Eqn. 4*).

$$wet\ strength\ retention\ (\%) = \frac{wet\ tensile\ strength}{dry\ tensile\ strength} * 100\% \qquad \textit{Eqn. 4}$$

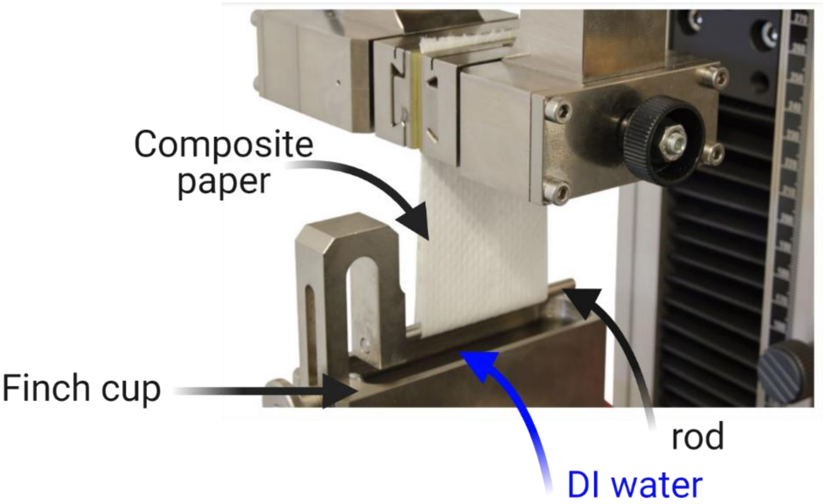

Figure 14. Wet tensile testing set up using Finch cup as per TAPPI T-456 standard. Image modified with BioRender.

2.3.3 Electrical characterization

Conductive paper nanocomposites were evaluated as liquid sensors for a water, organic solvents, and mixtures of water and organic solvents, and their electrical response was monitored.

2.3.3a 4-point probe

The special distribution of electrical sheet resistance across handsheets were collected by a 4-point probe method at 37 different locations across each sample, with probe spacing at 1$^{\pm}$0.01 mm, and an applied voltage of 10V. A mask with 37 evenly spaced cutouts, large enough for the four probe leads to fit, was placed on top of a conductive paper nanocomposite handsheet. With the Keithly 2450 voltage-current meter in 4 point probe mode, the four leads were connected to 4 probes spaced 1mm apart, and placed on the cutout in the mask. A weight with a known mass was placed on top of the probes to ensure the same contact between the probes and the nanocomposite was achieved for each measurement. The Keithly was then turned on to supply 10V, and measure the resulting resistance. A simplified testing schematic representative of how measurements were collected is depicted in **Figure 15**.

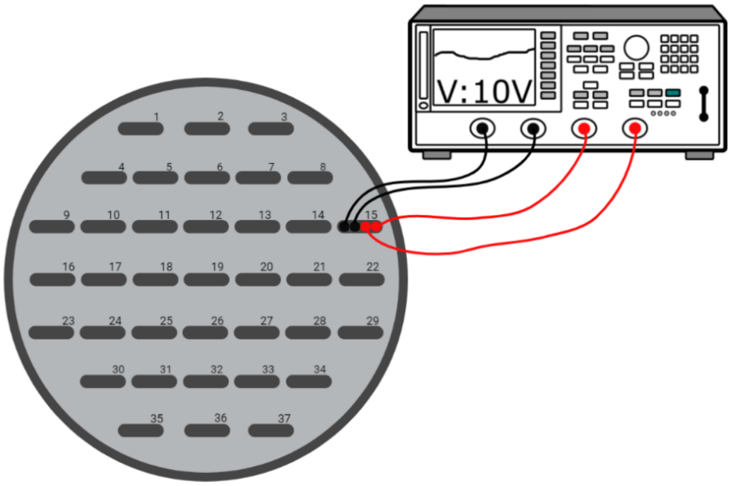

Figure 15. 4-point probe testing schematicRepresentative testing set-up for all 4-point probe measurements collected on batch-scale produced paper nanocomposites. Image created with BioRender.

2.3.3b Liquid sensing measurements

A Keithley 2450 voltage-current meter was used to monitor changes in electrical resistance across paper cutouts immersed in solution for all liquid sensing measurements. All liquid-sensing measurments were carried out using U-shaped samples cut from either the batch-scale handsheets or pilot-scale paper nanocomposite samples. Leads from the Keithly were connected to the tall edges of the U-shape with alligator clips. Using a lab-scale jack, a beaker of solutions (i.e. water, organic solvent) was slowly raised until the base of the 'U' was submerged in solution (~5 mm), and the electrical resistance response was monitored as a function of time for a given applied voltage, depicted in **Figure 16**.

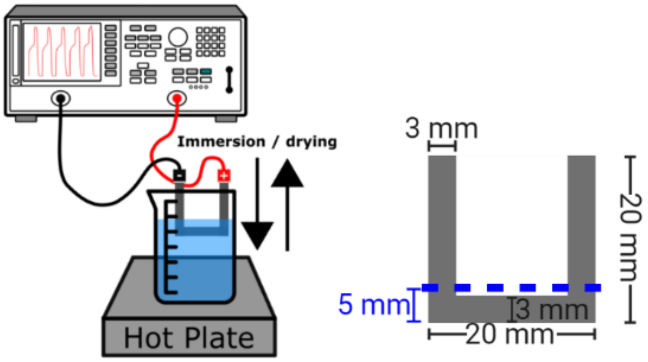

Figure 16. *Liquid sensing test set-up*. Schematic depicts representative liquid sensing test, where u-shaped paper nanocomposite sample is immersed and subsequently removed from solution. Enlarged u-shape shows dimensions of samples. Image created with BioRender.

A measurement cycle consisted of both an immersion and drying step, where the drying step was achieved by lowering the solution and wicking away excess drops of solution and allowing the sample to air dry for a desired amount of time. Liquid sensing performance was quantified based on the relative resistance (R_{rel}), defined as the ratio of the difference between the electrical resistances of the wet (R_t) and dry (R_0) specimen to the electrical resistance of the dry sample, as shown in the equation below:

$$R_{rel} = \frac{R_t - R_0}{R_0} * 100\% \qquad \textit{Eqn. 5}$$

Relative wet area measurements were estimated using photos and GIMP software to approximate the wet area with respect to the dry sheets. Relative wet length and wet width measurements were estimated by measuring the wet area determined in GIMP and comparing to the full length or width of the paper nanocomposite sample in the software.

2.3.4 Characterization of dielectric properties

This sub-section outlines the electrical testing procedures used to analyze the dielectric properties of CNF composite films described in Chapter 4 of this study.

2.3.4a Electrochemical impedance spectroscopy (EIS)

The films dielectric properties were recorded as a function of frequency, from 10^1 to 10^6 Hz at room temperature, using an impedance analyzer (MaterialsMates 7260, Italia). Prior to testing, films were dried in a vacuum oven at 90 °C for 24 hours to ensure any residual moisture was eliminated, and silver electrodes (ø~5 mm) were deposited on both sides of the film (90 seconds per side) using a Cressington 108 manual sputter coater with a 120 mm diameter chamber.

2.3.4b Breakdown strength

The breakdown strength of each film was measured by a PolyK ferroelectric polarization loop and dielectric breakdown strength system, with an increasing voltage rate of 200 V/s. Prior to testing, films were dried in a vacuum oven at 90 °C for 24 hours to ensure any residual moisture was eliminated, and silver electrodes (ø~5 mm) were deposited on both sides of the film (90 seconds per side) using a Cressington 108 manual sputter coater with a 120 mm diameter chamber. Film thickness at each electrode was measured using a digital micrometer. All breakdown measurements were performed in silicone oil at room temperature.

The measured electrical breakdown strength (E_b) values of pristine films were analyzed by the two-parameter Weibull statistical distribution described as

$$P(E_b) = 1 - \exp(-({}^{E_0}/_{E_b})^{\beta}) \qquad \textit{Eqn. 6}$$

where $P(E_b)$ is the cumulative probability of electric failure, E_0 is the experimental breakdown strength, E_b is a scale parameter representative of the characteristic E_b when the cumulative failure probability is 63.2%, and β is a shape parameter to analyze the scatter state of the data and indicate the reliability and uniformity of the film[99,115–117].

2.3.4c Electric polarization-electric field (P-E) loops

Electric polarization-electric (P-E) loops were measured by a PolyK ferroelectric polarization loop and dielectric breakdown strength system, at room temperature in silicone oil. Prior to testing, films were dried in a vacuum oven at 90 °C for 24 hours to ensure any residual moisture was eliminated, and silver electrodes (ø~5 mm) were deposited on both sides of the film (90 seconds per side) using a Cressington 108 manual sputter coater with a 120 mm diameter chamber. Film thickness at each electrode was measured using a digital micrometer.

III. Chapter 1. ‘Smart’ papers comprising carbon nanotubes and cellulose microfibrils for multifunctional sensing applications

Note: This chapter was published as an article in the Journal of Materials Chemistry A:

- B. Dichiara, A. Song, S. M. Goodman, D. He, J. Bai, *J. Mater. Chem. A* **2017**, *5*, 20161. (https://doi.org/10.1039/C7TA04329E)

Abstract

While historically, paper has been utilized in is most basic form, the large scale integration of lightweight and flexible materials in portable electronics has encouraged the use of paper based materials in novel ways, as it offers a renewable alternative to petrochemical substrates due to a low-cost, biodegradability, and biocompatibility. With the incorporation of electrically conductive fillers, such as carbon nanotubes (CNTs), paper can exhibit an electrical resistance response to external stimuli such as temperature shifts, mechanical deformations, and the presence of liquids and gasses[63,68–71,118]. Here, composite ‘smart’ papers were prepared combining cationic polyacrylamide and aqueous dispersions of hydroxyl-functionalized carbon nanotubes pre-adsorbed with alkali lignin on lignocellulosic wood microfibers, for the development of lightweight, flexible, and electrically conductive paper based sensors. The multifunctional sensing behavior of composite ‘smart’ papers to applied strain and liquid water was examined comprehensively, and demonstrated that papers possess superior tensile strain sensitivity compared to traditional foil gauges and opportunity for tailored liquid sensitivity based on material composition. Results indicate that these composite papers provide a low-cost and renewable alternative to traditional petrochemical-based materials for use in portable electronics and sensing applications.

3.1 Introduction

Historically, paper has only been utilized in its most basic form for the purpose of recording information. Recently, the large-scale integration of lightweight and flexible materials in portable electronics has encouraged the use of paper based materials in novel ways, as it offers a renewable alternative to petrochemical substrates due to a low-cost, biodegradability, and biocompatibility. Paper, consisting of a nonwoven network of randomly oriented fibers laid down to form a mat, is most typically made from cellulose, the most abundant natural polymer[19]. With the incorporation of electrically conductive fillers, paper can exhibit an electrical resistance response to external stimuli such as temperature shifts, mechanical deformations, and the presence of liquids and gasses[63,68–71,118]. This emerging field of 'smart' materials offer compelling alternatives for use in a variety of applications in healthcare, packaging, and wearable electronics. Among a variety of conductive fillers, carbon nanotubes (CNTs), comprising of one or several sheets of hexagonally packed carbon atoms rolled in concentric seamless tubes, have drawn considerable attention due to their exceptional electrically conductivity, mechanical strength, and thermal stability. Typically produced by catalytic chemical vapor deposition (CVD), which is becoming a more scalable fabrication technique, large scale CNT fabrication is being more widely studied[89]. Prompted by the possibility of the large scale integration of CNTs, numerous studies have focused on their incorporation into a cellulose matrix to prepare green composite films[119–121]. However, typical papermaking techniques are less studied even though they are known to offer a more efficient and eco-friendly approach than typical solution processes being studied that require additional and expensive solvents for dispersion.

The methods for preparing 'smart' paper sensors can be classified into two different categories. The first consists of coating a conductive layer, CNTs, on the external surfaces of an already existing paper specimen[19,73]. The second involves mixing the conductive component (i.e. CNTs) with cellulose fibers during papermaking to yield a percolated conductive network constituting electrical paths throughout the whole volume of the prepare paper[19,74]. Although both approaches offer short processing times and cost –effectiveness, the later exhibits higher potential for sensing applications due to increased interactions between CNTs and cellulose fibers. Since inter-fiber cohesion of cellulose consists of hydrogen bonding, one challenge associated with the introduction of CNTs however, is that the addition of carbon without hydroxyl groups to the pulp matrix inhibits the interaction between cellulose fibers, hence hindering the mechanical integrity of the paper. This is particularly relevant as most of the research about CNT-cellulose composite papers to date, reports extremely high CNT contents, up to 70 wt%[122,123]. However, it has been reported that at loadings higher than 15 wt%, CNTs are no longer well captured by the cellulose fibers and can easily detach from minimal bending or touching[124]. In addition, the incorporation of high loadings of CNTs is known to reduce the tensile strength of papers[75]. By incorporating a cationic fixing agent, Imai and coworkers were able to limit the loss of tensile strength and high CNT loadings of 9.1 and 16.7 wt%[76].

In the present work, the development of CNT-cellulose composite smart papers were prepared with substantial enhancements of paper strength properties with CNT loadings as high as 10 wt%. Handsheets were prepared with unbleached Kraft softwood pulp modified by a layer-by-layer nanoassembly technique[125], comprising subsequent coating of cationic polyacrylamide (CPAM) and pristine and hydroxyl-functionalized (CNT-OH) CNTs pre absorbed with alkali lignin (AL) on the surface of cellulose microfibers. The as-produced paper nanocomposites were thoroughly characterized, and their performance as strain sensors, pressure sensors and liquid water sensors were studied in detail.

3.2 Results and discussion

3.2.1 Microstructure of CNT-cellulose paper nanocomposites

Composite smart papers were prepared following a modified TAPPI T-205 standard method, described in detail in the Materials and Methods section of this text. Briefly, handsheets were formed by a filtration method, and then pressed and dried according to TAPPI standards. Prior to sheet formation, pristine or functionalized CNTs were first dispersed in alkali lignin using a double acoustic irradiation system, combining both probe and bath sonication, to promote individualization of CNTs in solution, contributing to a uniform distribution of conductive CNTs throughout the resulting paper nanocomposite[110]. An aqueous dispersion of CPAM was first added to a mixture of unbleached Kraft softwood pulp fibers, and combined at 50 °C for 30 minutes. The as-dispersed CNT: AL solution was then added to the pulp mixture, and combined under constant agitation for 30 minutes. The combined suspension was then filtered, pressed, and dried to form handsheets. The proportion of cellulose pulp fibers, CPAM, CNTs, and AL were adjusted to obtain handsheets with a final grammage of 60 g/m^2 and CNT loadings of 2.5 and 10 wt%. The ratio of CNT: AL was kept constant at 2:1 for all handsheets. Prior to all characterization and testing, handsheets were stored under controlled temperature and humidity (23 °C, 50 % RH) for 48 hours.

The morphology of the CNT-cellulose composite papers was examined by scanning electron microscopy, as illustrated in **Figure 17**. In all samples, the Kraft softwood microfibers are nested together creating a cellulose matrix, which is consistent with typical papers produced by papermaking techniques. At low CNT contents (1.e. 2.5 wt%), nanotubes were observed on the surface of the cellulose microfibers without forming and visible aggregates regardless of the surface functionalization of the CNTs (not shown). A proposed mechanism is that the CNTs coated with anionic alkali lignin form a complex with the cationic retention aid (CPAM) pre-absorbed on the surface of the cellulose microfibers (smart pap ref 21). At higher CNT loadings (i.e. 10 wt%) however, the presence of several large CNT aggregates were found on the cellulose matrix, as indicated by the red arrows in **Figure 17a**. Since the uptake of lignin-coated CNTs is driven by electrostatic attraction between oppositely charged constituents, the net surface charge of the cellulose microfibers becomes negative at high CNT-lignin concentrations. This hinders the adsorption of CNTs on the fiber surface and generated agglomerates in the mixture, yielding non-uniform CNT dispersions. These aggregates can interfere with hydrogen bonding of the cellulose microfiber network, hence decreasing the mechanical integrity of the paper. Interestingly, it can be seen in **Figure 17b** that the hydroxyl-functionalized CNTs are evenly distributed with limited to no traces of agglomeration under the same conditions. Moreover, the high magnification inset indicates that CNT-OH dispersed between adjacent cellulose microfibers act as bridges interconnecting neighboring fibers with each other. The improved dispersion of CNT-OH can be attributed to the interfacial interactions between oxygen groups on the CNTs and the cellulose microfibers, as demonstrated by the FTIR spectra shown in **Figure 17c**. It is well accepted that the band ranging from 3600 to 3100 cm^{-1}, indicative of various hydroxyl moieties, is sensitive to hydrogen bonding[126]. The characteristic shift toward lower wavenumbers reveals the presence of strong hydrogen bonds between –OH groups[127]. In particular, the –OH stretching vibration band at ~3321 cm^{-1} in the plain cellulose paper gradually shifts to lower wavenumbers with increasing CNT-OH contents (i.e. 3306 cm^{-1} at 2.5 wt%, 3294 cm^{-1} at 10 wt%), confirming the presence of hydrogen bonding between the hydroxyls on the CNT surface and the –OH groups in the cellulose microfibers.

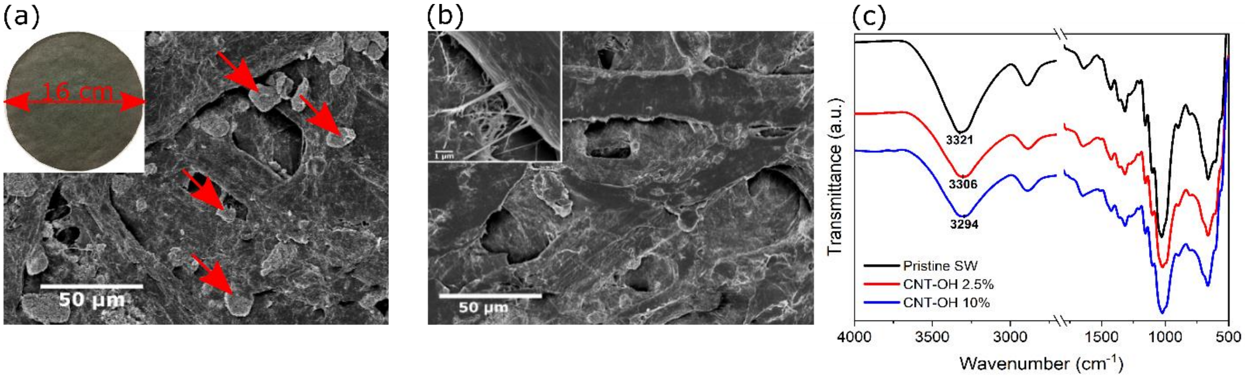

Figure 17. Morphology of unbleached softwood paper nanocomposites. Representative SEM images of Kraft softwood papers reinforced with 1 wt% CPAM and (a) pristine CNTS and (b) CNT-OH at 10 wt% loading. A photograph of a typical 10 wt% CNT-cellulose composite paper is shown in the inset in (a). (c) FTIR spectra for pristine, 2.5, and 10 wt% CNT-OH composite papers.

3.2.2 Mechanical properties of CNT-cellulose composite papers

As the paper nanocomposites were developed as multifunctional sensors, their mechanical robustness was of great importance in understanding their durability in a variety of sensing applications. **Figure 18** compares the breaking length and internal bonding strength of papers at different CNT and CNT-OH loadings. The breaking length, a common metric used in the pulp and paper industry as a normalization of tensile strength by paper grammage (g/m^2), is defined by TAPPI T-494 standards as the limiting length a strip of uniform width, beyond which, if such a strip was suspended by one end, it would break of its own weight. The incorporation of CNTs into the cellulose microfibers network diminishes the breaking length of paper. The decrease in breaking length is more drastic at higher CNT loadings, which is consistent with previous works reporting the reduction of papers' tensile strength after the introduction of CNTs[75,76]. This can be attributed to the presence of large CNT aggregates interfering with inter-fiber bonding, as observed in the SEM images in **Figure 17a**. Interestingly, the breaking length of paper is improved when CNTs functionalized with hydroxyl groups are added to the cellulose microfibers. This reinforcing effect, however, is weakened at high CNT-OH content (i.e. 10 wt%). Compared to the control sample, the breaking lengths of the papers reinforced with 2.5 and 10 wt% CNT-OH increase by ~10 and ~5 %, respectively.

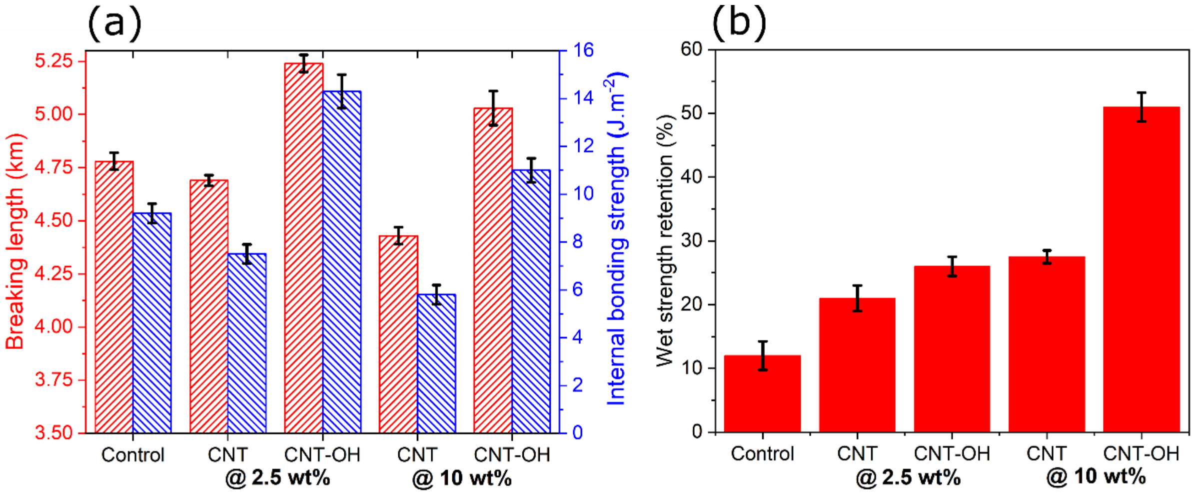

Figure 18. *Dry and wet strength properties.* (a) Dry strength properties of CNT-cellulose composite papers prepared with various contents of pristine and functionalized CNTs and (b) wet strength properties of CNT-cellulose composite papers prepared with various contents of pristine and functionalized CNTs.

Hydroxyl-functionalized CNTs can be evenly dispersed throughout the entire cellulose matrix, and the strong interfacial hydrogen bonding as demonstrated by FTIR, promotes the stress transfer in the interfacial region, thus enhancing the breaking length of the material. Moreover, paper strength is known to be governed by two mechanisms: (i) the gradual failure of interfiber bonds, and (ii) the rupture of individual fibers. Since pulping and papermaking operations were the same regardless of the presence of CNTs, indicating the intrinsic strength of the cellulose microfibers remained constant across all samples, it is reasonable to assume that the former is the dominant mechanism. For further validation, the internal bonding strength of the CNT-cellulose composite papers, conventionally defined as the energy required for breaking bonds per unit area of paper (J/m^2) at a 90° angle to the plane of the fibers was analyzed. To this aim, the Scott bond test, one of the most commonly employed methods for meausing the internal coherence of papers, was used. Although this technique is understood to overestimate the internal bonding strength due to its dynamic nature which may cause the occurrence of rupture in the fiber wall, such effect is typically limited at low basis weights (i.e. 60 g/m^2) as were used in this study[128]. From **Figure 18a**, it can be seen that the internal bonding strength results are indeed correlated with the breaking length data. This indicates that the interfiber bonds of paper substrates can be modulated by adding CNTs with varying degrees of surface functionalization. Furthermore, the increase in internal bonding strength with the incorporation of CNT-OH most likely derives from the enhancement of relative bonded area. This is consistent with SEM observations showing CNT-OH bridging neighboring cellulose microfibers together, increasing the number of contact points between adjacent fibers.

Since one of the sensing applications of particular interest was the detection of liquid water, it is critical to evaluate the paper's ability to handle mechanical stress when wet. Therefore, the tensile strength of the paper nanocomposites was measured after immersion in DI water for 10 seconds using a Finch cup, as described in the Materials and Methods section of this text. **Figure 18b** reports the wet strength retention of samples prepared with different contents of CNT and CNT-OH, defined by TAPPI T-456 standard as the ratio of the tensile strength of a paper in the wet state to that of the same composition in the dry state. The wet strength retention increases with CNT content and, at the same loading, is higher for samples containing hydroxyl-functionalized CNTs. The invasion of water among the fiberous cellulose network causes the destruction of the hydrogen bonds by increasing the distance between individual fibers. The hydrophobic nature of the CNTs prevents the infiltration of water via the formation of a CNT network surrounding the cellulose microfibers and creating water-resistance bonds at fiber-fiber crossings. With a loading of 10 wt% CNT-OH, the wet strength of the paper is more than half its dry strength, which is nearly five times higher than that of the control papers. Since the papers with CNT-OH exhibit higher mechanical integrity, composites prepared with functionalized CNTs were used for the remainder of multifunctional sensing application studies, and henceforth reported as “CNT-cellulose composite papers”.

3.2.3 Stress/strain sensing

CNT-cellulose composite papers at both CNT-OH loadings were evaluated as strain sensors. **Figure 19** exhibits the typical evolution of the relative electrical resistance (R_{rel}) and mechanical stress (σ) as a function of strain (ε) until fracture for composite papers with both 2.5 and 10 wt% CNT-OH loadings. The R_{rel} (%) defined in Chapter 1 as the ratio of the difference between the electrical resistance at a given time (R_t) and the initial resistance (R_0) to the initial electrical resistance of the paper (R_0), such that $R_{rel} = (R_t-R_0) / R_0 \times 100\%$. For all samples, it can be observed that for strain below 0.02, the resistance change (R_{rel}) is zero, indicating that there is no difference between the electrical resistance of the deformed and undeformed specimens under these conditions. When the strain increases further, R_{rel} increases monotonically, and beyond a certain strain, R_{rel} increases exponentially until the ultimate failure of the composites. This qualitative behavior with a linear piezoresistivity at low strains, followed by a nonlinear piezoresistivity at larger strains is consistent with previous studies reporting the piezoresistive properties of CNT composites[120,129]. Although the resistance change increases until fracture, these different stages suggest that different piezoresistive behaviors are dominant. Considering typical piezoresistive behavior of CNT-composites[130], percolation-based scaling rule is dominant in the linear resistance-strain region, while tunneling effects become significant in the non-linear resistance-strain region. Moreover, since limited deformation is expected in the CNTs, the contribution of piezoresistivity of CNTs themselves to the total piezoresistivity of the composites can be neglected. Initially, the CNT within the undeformed composite can be considered as overlapping at the contact locations, instead of being arranged in an end-to-end configuration. In the linear resistance-strain region, the CNTs are still overlapping and the percolation-based scaling rule applies. For strain levels beyond the linear region, CNTs lose overlapping contact with each other, and thus tunneling resistance becomes the dominant phenomenon as the number of CNT-CNT junctions reduces rapidly.

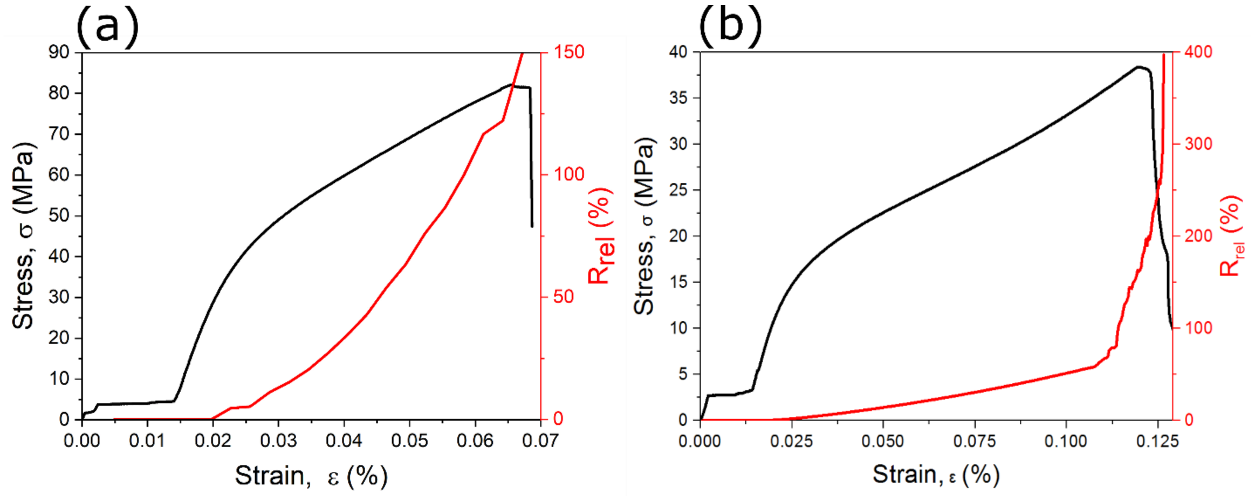

Figure 19. *Electrical response to mechanical stress/strain*. CNT-cellulose composite papers with a CNT-OH content of (a) 2.5 wt% and (b) 10 wt%.

To investigate the application of CNT-cellulose composite papers as strain sensors, their sensitivities are compared to those of metal alloys commonly utilized for conventional foil type strain gauges. The strain sensitivity of the specimens in the linear region is comparable to that of the metal alloys, while in the nonlinear region the CNT-cellulose composite papers exhibit much higher sensitivity than conventional foil gauges. For the composite with a CNT-OH content of 10 wt%, the abrupt change in resistance in the nonlinear region suggests the papers can function like a switch. Furthermore, the composite papers are operational over a wider strain range, up to a strain of 0.11, whereas previous studies have reported measurements below strains of 0.07[131,132]. Given their low-cost, flexibility, and piezoresistive properties, these CNT-cellulose composite papers can serve as tunable strain sensors for a variety of applications.

3.2.4 Liquid water sensing

The water sensing meausrements were carried out using u-shaped samples cut from the as-prepared CNT-cellulose composite papers, as illustrated in the Materials and Methods section of this text. The evolution of R_{rel} for CNT-cellulose composite papers with different CNT loadings as a function of time immersed in water during multiple immersion/drying (120 s/600s) cycles is shown in **Figure 20a**. In each case, drastic changes in R_{rel} can be observed when the specimen are immersed in aqueous media, indicating that both compositions are extremely sensitive to water. For all samples, R_{rel} rapidly increases in the presence of water until the resistance value jumps to reach an extreme. During the drying process of the papers in air at room temperature for 10 minutes, the R_{rel} values return almost to their initial base level. The signals are quite stable and reproducible over three immersion/drying cycles with all R_{rel} values increasing/decreasing to almost the same level during the entire experiment, indicating that not only are the CNT-cellulose composite papers extremely sensitive to water, but they also exhibit excellent recovery properties.

In typical CNT composites for liquid sensing, the resistance change of the sensing material can be attributed to (i) changes in the carrier concentration due to adsorbed molecules on the surface of the CNTs, and (ii) swelling of the polymer matrix, altering the electron transport between the conducting CNT networks. Although the former is often considered the dominant mechanism, it usually yields much smaller changes in resistance (smart pap ref 32), indicating the water adsorbed on the CNTs cannot solely be responsible for the speed and amplitude of the observed electrical response in **Figure 20a**. As a result, the swelling of the cellulose plays a major role in the water sensing mechanism of the CNT-cellulose composite papers. Furthermore, water molecules need to interact with hydroxyl groups to be adsorbed by either the cellulose microfibers or CNTs, indicating the adsorption of water depends on the number of available hydroxyl groups, not those linked with each other. Since CNTs are dispersed in the cellulose matrix via hydrogen bonding, they are unlikely to interact with water molecules. Therefore, the contribution of water adsorption on the CNT surface to the variations in electrical resistance is extremely limited. Similarly, the crystalline region of the cellulose microfibers is tightly bonded, with minimal access to water. Thus, the water uptake occurs only in the amorphous regions of the cellulose microfibers, where large amounts of free hydroxyl groups are available[63]. As the water molecules enter or leave the amorphous regions, the cellulose chains either move apart or draw closer together, altering the electron transport by varying the intertube distance between neighbored CNTs above or below the tunneling distance, causing the unique reversibility of the composites electrical resistance. Noteworthy, the water-induced electrical resistance changes strongly depend on the CNT-OH content of the composite, suggesting the responses can be tailored by the composite composition. Besides the obvious differences in their absolute values, the electrical resistance exhibits an opposite trend with the CNT-OH content of 2.5 wt% compared to 10 wt%. When immersed in water, the R_{rel} of the composites with 2.5 wt% CNT-OH decreases, while it increases in the case of higher CNT-OH loading (i.e. 10 wt%). At low CNT-OH content there are limited contacts between CNTs in the initial dry state, hence neighboring CNTs are actually pushed closer together as the cellulose matrix swells, resulting in higher electrical conductivity (i.e. decrease in resistance). On the other hand, the probability to disrupt existing conductive networks by the swelling cellulose becomes significant at higher CNT-OH contents. Moreover, the slight reduction of electrical resistance for the composites with 10 wt% CNT-OH in the initial dry state may be attributed to the reconstruction of some damaged conductive CNT networks originating from the highly hygroscopic swelling of the cellulose[120]. These observations are in good agreement with the percolation theory and suggest that optimal sensitivity may be achieved for CNT content close to the percolation threshold. In addition, the reduction of the composite grammage (g/m^2) tends to increase paper porosity, which may be beneficial to water absorption, increasing the hygroscopic expansion effect[133]. Although further work is needed to thoroughly examine the influence of grammage, CNT content, and nature of cellulose microfibers on the electrical response, the maximum R_{rel} obtained thus far, 3,100%, is among the highest values reported to date[63], which makes the CNT-cellulose composite papers very compelling for fast and reversible water sensing applications.

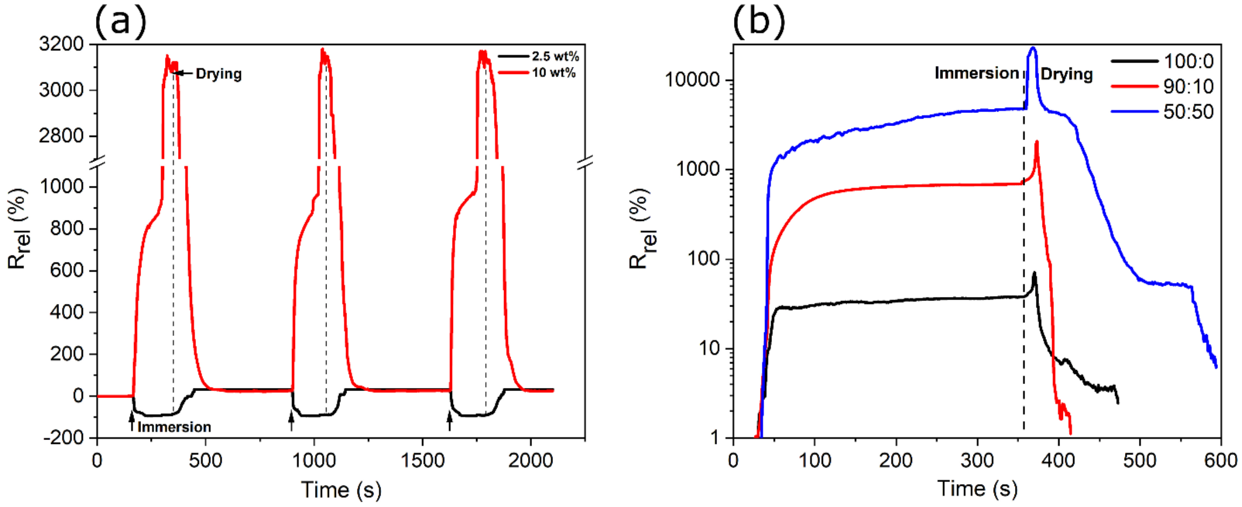

Figure 20. *Electrical response to liquid sensing measurements*. (a) Relative resistance (R_{rel}) change of CNT-cellulose composite papers with different CNT-OH contents as a function of time during multiple immersion/drying (120s/600s) cycles. (c) Relative resistance (R_{rel}) change of CNT-cellulose composite papers comprising 10 wt% CNT-OH as a function of time immersed in different water/ethanol solutions.

It has been well established that the swelling of cellulose depends on the solvent nature, and especially on its hydrogen-bonding parameter[134,135]. Dark field optical microscope observations, shown in **Figure 21**, exhibit the swelling behavior of cellulose fibers exposed to air, water, and ethanol. After two minutes of immersion, the cellulose fibers show a dramatic increase in thickness when exposed to water, with nearly threefold augmentation of the average fiber diameter compared to that of the dried fiber. The swelling capability of the cellulose fibers is significantly reduced in ethanol and the average fibers diameter increases by less than 10 μm. These results are consistent with other observations of the swelling behavior of cellulose in various solvents[135]. Prompted by this, we demonstrated the possibility to discriminate water from other solvents, by investigating the ability of the CNT-cellulose composite papers to analyze different water content in ethanol solutions. The development of a simple, affordable, fast, and reliable technique for the detection of water in organic solvents is particularly critical not only for chemical industries producing dry solvents, alcoholic beverages, and moisture-sensitive chemicals but also for industries manufacturing oils and petroleum products, in which water is a common contaminant and impurity. **Figure 20b** shows the R_{rel} of the CNT-cellulose composite paper with a CNT-OH loading of 10 wt% in water-ethanol solutions with different ethanol/water (v/v) ratios at room temperature. It can be seen that pure ethanol leads to a maximum R_{rel} of on 30% after immersion for 5 minutes, which is more than two orders of magnitude lower than that of pure water after immersion for only 2 minutes (3,100%). Different mixtures of water and ethanol can be easily distinguished, and water content as low as 10% v/v still yields high R_{rel} of 550%, as illustrated in **Figure 20b**. Compared to other techniques such as Karl Fischer titration[136] or fluorescence[137], the monitoring of the electrical resistance change of immersed CNT-cellulose composite papers is much simpler and more affordable, and offers opportunities for remote and *in situ* diagnostics.

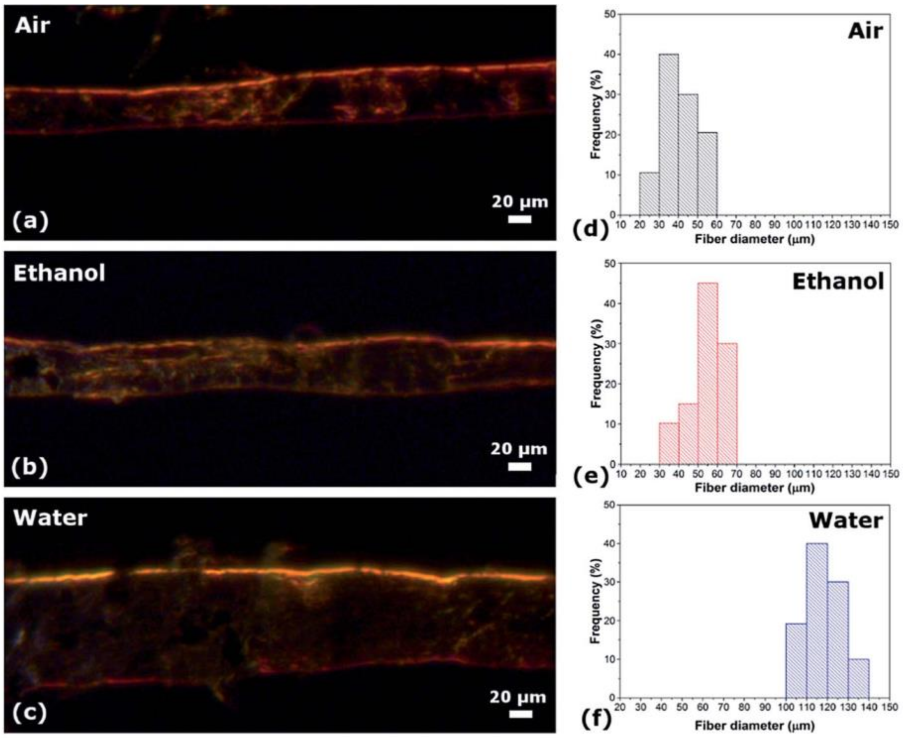

Figure 21. Microscopic swelling of unbleached pulp fibers. (a-c) Dark field optical microscopy images and (d-f) diameter distribution of pulp fibers when exposed to air, ethanol, and water for 120 seconds.

3.3 Conclusion

In summary, composite smart papers were prepared from a simple, low-cost, and "green" papermaking process using unbleached softwood microfibers modified by a layer-by-layer nanoassembly process, where CPAM and lignin-coated CNTs act as cationic and anionic polyelectrolytes, respectively, to create subsequent layers of oppositely charged components on the surface of cellulose fibers. The resulting papers are lightweight, flexible, and exhibit improved dry and wet strength properties, which can be attributed to the enhanced interfacial interactions between functionalized CNTs and cellulose fibers, originating from hydrogen bonding. The embedded CNT network forms electrically conductive pathways endowing the smart papers with extreme sensitivity to various external stimuli, In particular, the as-prepared CNT-cellulose composite papers were successfully employed as highly sensitive, well reversible and reproducible detectors for the presence of water. Furthermore, their superior tensile strain sensitivity compared to conventional foil gauges makes them ideally suited for a large variety of applications ranging from the remote detection of water leakages to water content determination and actuators. These findings are extendable to the fabrication of other renewable materials for multifunctional applications. These results have fueled the continuation of this work to further optimize the material properties, especially at higher CNT loadings, and develop a scale-up continuous flow process for commercialization.

IV. Chapter 2: Optimization of ‘Smart’ paper nanocomposites for multifunctional liquid sensing applications

Note: This work is under review as a portion of an article submitted to NanoToday in April 2021.

Abstract

Cellulose-based paper electronics is an attractive technology to meet the growing demands for naturally abundant, biocompatible, biodegradable, flexible, inexpensive, lightweight and highly miniaturizable sensory materials. The price reduction of industrial carbon nanotube (CNT) grades offers opportunities to manufacture electrically conductive papers whose resistivity is responsive to environmental stimuli, such as the presence of water or organic solvents. Here, a highly sensitive paper nanocomposite is developed by integrating CNTs into a hierarchical network of pulp fibers and nanofibrillated cellulose (CNF). Composite material properties, including cellulose type, CNT content, CNT:CNF ratio, and density are optimized to achieve the highest response as multifunctional liquid sensors, such as leak detectors and wave monitoring. The sensitivity to liquid water spans an outstanding four orders of magnitude, even after 30 cycles and 6-month natural aging, due to the hydroexpansion of the hierarchical cellulose network, which alters the intertube distance between neighboring CNTs.

4.1 Introduction

While a fifth of the world population lacks safe water, leaky pipes and wasteful irrigation systems are major contributors to water scarcity on the planet. The American Society of Civil Engineers indicates that about a quarter-million water line breaks occur each year in the U.S., representing more than 26 billion liters lost each day due to leaky pipes and costing public water utilities up to \$2.8 billion annually[138]. In addition, 37% of U.S. homeowners are reported to have suffered losses from water damage, costing another $2.5 billion annually to insurance companies[139]. Worldwide, the World Bank estimates that global non-revenue water, which refers to the cost of water lost to leaks and billing errors approaches $14 billion. Although existing systems can detect and quantify the extent of water losses, they typically attempt to infer leak location via flow rate variations, a process which is time consuming and requires human intervention to confirm. An ideal leak monitoring system would consist of a low cost array of optimally spaced remote sensors to minimize the reaction time to patch a leak and power off sensitive instruments when necessary. However, sensing liquid water in a reliable and affordable way poses a major challenge. Existing technologies remain expensive and either have weak or slow responses to water due to the non-polar nature of the materials employed, or is partially soluble in water, like most polymer-based systems, which produce inconsistent signals due to material degradation in aqueous environments[77–82].

Given its bio-renewable and hygroscopic nature, cellulosic paper provides an excellent platform for building sustainable and affordable water sensors with superior performance. To date, most research has focused on hosting various types of electrodes onto the surface of paper using pencil drawing, inkjet printing, sputtering, and other forms of coating techniques[73,140–142]. These methods, however, are characterized by the low accuracy and non-uniformity of the electrode films formed on the paper surface, which adversely affect device performance and reliability, besides making the fabrication process at large scale very challenging. In contrast to these efforts, my previous work proposed to incorporate electrically conductive nanoparticles into the fibrous network prior to sheet formation, which offers greater control over the percolated network of fillers constituting electric paths in the material, as described in Chapter 1[19]. The present research describes the optimization of electrically conductive paper nanocomposites by tailoring the cellulose type, CNT content, surfactant type, ratio of CNT: surfactant, and the resulting paper density. A key element of this approach consists of a unique binding chemistry ensuring a strong adhesion between the nanoparticles and the pulp fibers even at high loading (*i.e.* up to 15 wt.%), and the introduction of nanofibrillated cellulose (CNF) as a unique dispersing agent. The resulting paper nanocomposites material properties were thoroughly characterized, and their functionality of fast and reliable liquid water sensors was examined in detail.

4.2 Results and discussion

4.2.1 Comparison of cellulose microfiber and surfactant type

While it is understood that the physical adsorption of surfactants onto the surface of CNTs is a successful approach to individualize CNT aggregates and take full advantage of their superior mechanical and electrical properties, the majority of surfactants used are petroleum-based chemicals. Although previous work established alkali-lignin (AL), the second most abundant natural polymer, as a viable surfactant with enhanced CNT dispersion capabilities[110], its large molecular structure may inhibit electrical conductivity by diminishing available CNT surface area. Recently, the use of CNF as a surfactant for CNTs has been investigated, and indicate that due to fluctuations of counter ions on the surface of both the CNTs and CNF, long-term stable colloidal dispersions can be achieved for high CNT contents[62]. Taking into account the potential for increased dispersion quality, CNF was evaluated as a sustainable surfactant for the preparation of aqueous CNT dispersions. Solutions were prepared comparing CNF to AL and two of the most common petrochemical based surfactants, sodium dodecyl sulfate (SDS) and cetyl-trimethylammonium bromide (CTAB), using optical absorption (UV-vis) spectroscopy. All solutions underwent the same preparation method, described in detail in the Material and Methods section of this text. Briefly, the surfactant was first dispersed in DI water and mechanically stirred for 5 minutes, followed by 5 minutes of bath sonication. A desired content of CNTs were then added into the aqueous solution, keeping the ratio of CNT: surfactant at a 2:1 ratio. The combined dispersions were then double sonicated, combining both bath and probe sonication[110]. Resulting dispersion where characterized with optical absorption (UV-vis) spectroscopy. UV-vis spectroscopy is one of the most commonly used techniques to evaluate the quality of CNT dispersions as individual CNTs are active in the UV-vis range, displaying characteristic absorption bands, while CNT aggregates diminish the photoluminescent effect[113,143]. As aggregates do not absorb light in the measured UV-vis range, the degree of individualization of CNTs is correlated to the intensity of the absorbance spectra, where a higher absorbance indicates a higher degree of individualization. **Figure 22** confirms that CNF promotes the individualization of CNTs in aqueous solution, and yields a comparable dispersion quality to traditional petrochemical based surfactants.

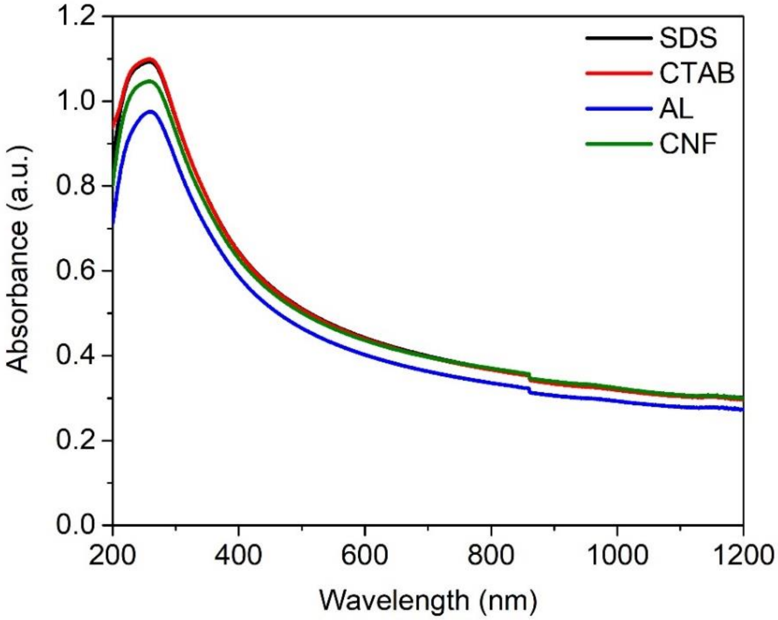

Figure 22. CNF *dispersion quality*. Optical absorption spectroscopy of aqueous CNT suspensions (1 wt%) using different dispersants, SDS, CTAB, AL, and CNF in a 2:1 ratio CNT: dispersant.

Based on the success of CNF as a dispersant, it was employed as a surfactant to disperse hydroxyl-functionalized (CNT-OH) CNTs in solution prior to embedding in paper nanocomposites to form CNT: CNF complexes. Prior to dispersing CNT-OH, CNF was extracted from cellulose microfibers following a previously reported TEMPO-mediated oxidation process, described in detail in the Materials and Methods section of this text[50]. Preliminary handsheets were then prepared based on the previously reported procedure, as described in detail in the Materials and Methods section of this text, to evaluate different types of cellulose fibers as well as CNF as components in conductive paper nanocomposites[19]. While the CNT-OH content, ratio of CNT: surfactant, and paper density were kept constant at 15 wt%, 2:1 and 60 g/m^2, respectively, the type of cellulose microfiber (softwood, SW), whether bleached or unbleached, and the type of surfactant, AL or CNF, were used to prepare handsheets with different material compositions to study their effect on the paper nanocomposites response to liquid water. Optical microscopy confirms that bleached SW fibers exhibit a similar swelling behavior to unbleached SW fibers when exposed to water and ethanol, experiencing over a 27.5% diameter increase when exposed to water, compared to a 7.4% increase when exposed to ethanol, as shown in **Figure 23**. These observations are consistent with other studies and suggest that polarizability and molar volume are the main solvent characteristics influencing the swelling behavior of cellulose.[19,135,144–146] The superior swelling behavior of bleached SW fibers in water compared to organic solvents confirmed their potential as a sustainable matrix material for the preparation of paper nanocomposites for use in water sensing applications.

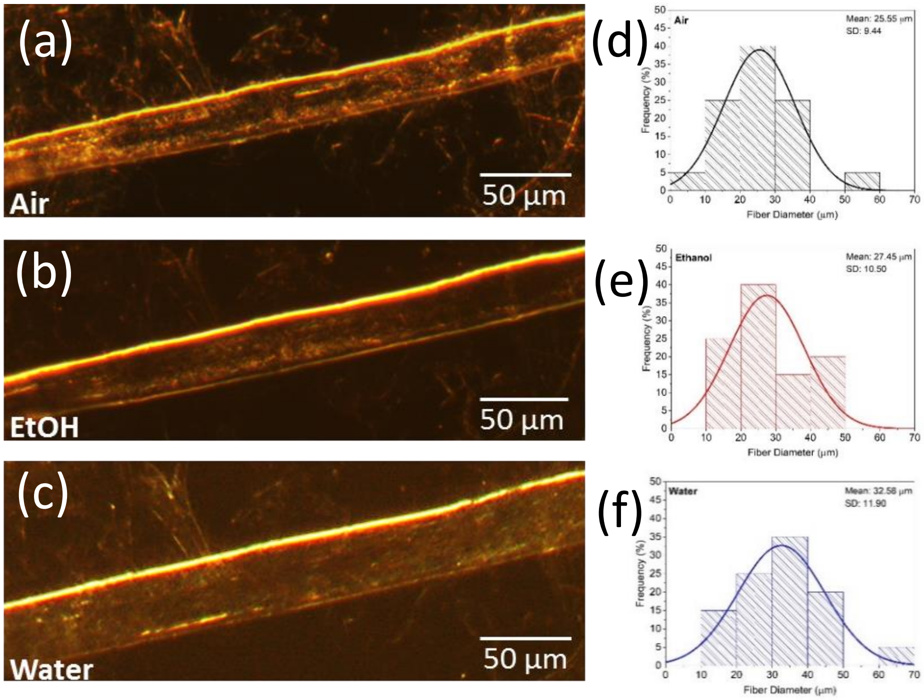

Figure 23. *Microscopic swelling of SW pulp fibers*. Dark field optical microscopy images (a-c) and diameter distribution (d-f) of modified pulp fibers in air (a,d) and after immersion in ethanol (b,e) and water (c,f) for 30 s.

It is clear from **Figure 24a** that a significant improvement in sensitivity was achieved for the handsheets prepared with bleached cellulose microfibers and CNF compared to those prepared with unbleached cellulose microfibers and AL. Compared to previous work where unbleached cellulose microfibers were used[19], the bleached cellulose microfibers have undergone an additional delignification process to remove up to 99% of the residual lignin. The sensitivity of the paper nanocomposites to liquid water is known to stem from cellulose expansion, due to their hygroscopic nature, where the extent of cellulose expansion depends on the uptake of water molecules, which occurs mainly in the amorphous regions of cellulose where larger numbers of free hydroxyl moieties are available.[63,147].

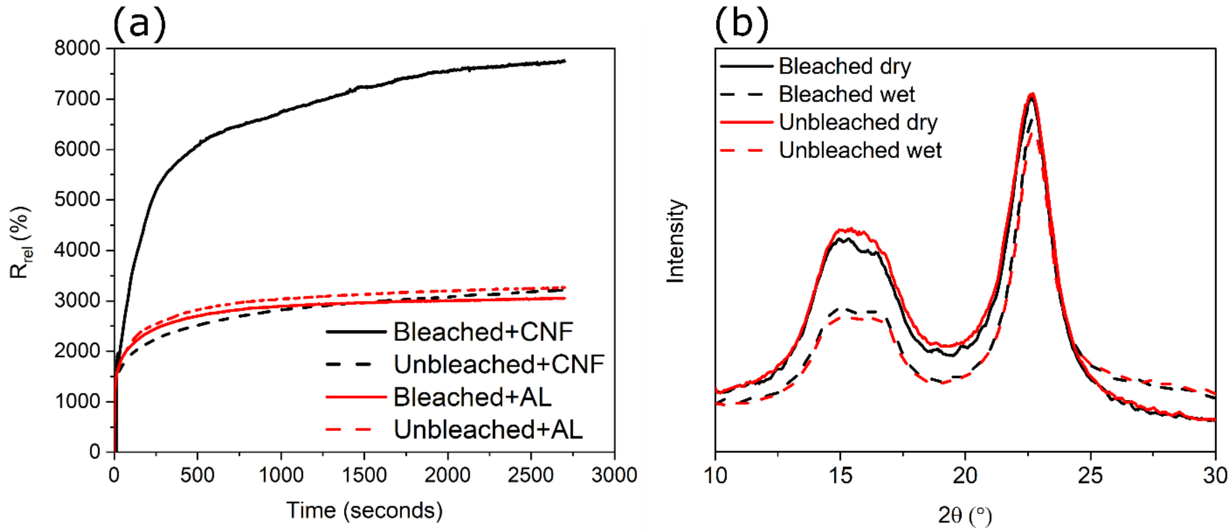

Figure 24. *Evaluation of cellulose nano and microfibers in paper nanocomposites*. (a) Relative resistance (R_{rel}) curves comparing handsheets prepared with different types of cellulose microfibers and different surfactants (AL, CNF), when immersed in DI water. (b) X-ray diffractograms of pristine handsheets prepared with bleached and unbleached softwood pulp fibers in their dry and wet state, after soaking in DI water for 60 s.

Comparing the X-ray diffractograms of dry and wet bleached and unbleached softwood pulp (**Fig. 24b**), the same shift in the characteristic 2θ cellulose peak is observed for both types of wet pulp (**Table 2**). This indicates that each sample experienced the same level of strain in their cellulose crystalline regions after soaking in water for 60 seconds. Despite presenting the same magnitude of expansion – *i.e.* each swollen sample have similar crystallite size[112], the presence of lignin in the unbleached pulp considerably limits the extent of water sorption, reducing the total swellable area within the sample. Replacing the AL dispersing agent with CNF effectively delignifies the cellulose microfibers further, increasing the wettable area and resulting in an increase in sensitivity explained in part by ability of the CNF to swell in the presence of water, creating a hierarchically swellable structure[148–150].

Table 2. 2D-XRD parameters for bleached and unbleached cellulose pulp, dry and after being soaked in DI water for 60 seconds.

Sample ID	FWHM	(200) peak 2θ (°)	CrI (%)	Crystallite size (L_{200}, nm)
Bleached dry	2.17	22.54	82.39	3.59
Bleach wet	1.89	22.72	92.74	4.11
Unbleached dry	2.26	22.51	79.64	3.44
Unbleached wet	1.93	22.72	95.09	4.03

4.2.2 Characterization of microstructure and morphology

Based on the success of CNF as a surfactant, it was employed to disperse hydroxyl-functionalized (CNT-OH) CNTs in solution prior to embedding in paper nanocomposites to form CNT: CNF complexes. Handsheets were then prepared using bleached cellulose microfibers based on the previously reported procedure, as described in detail in the Materials and Methods section of this text[19]. Prior to handsheet preparation, CNF was extracted from cellulose microfibers following a TEMPO-mediated oxidation process. Electron microscopy confirms the even distribution of nanoparticles in the paper without significant aggregation despite loadings as high as 15 wt.% (**Fig. 25a-c**).

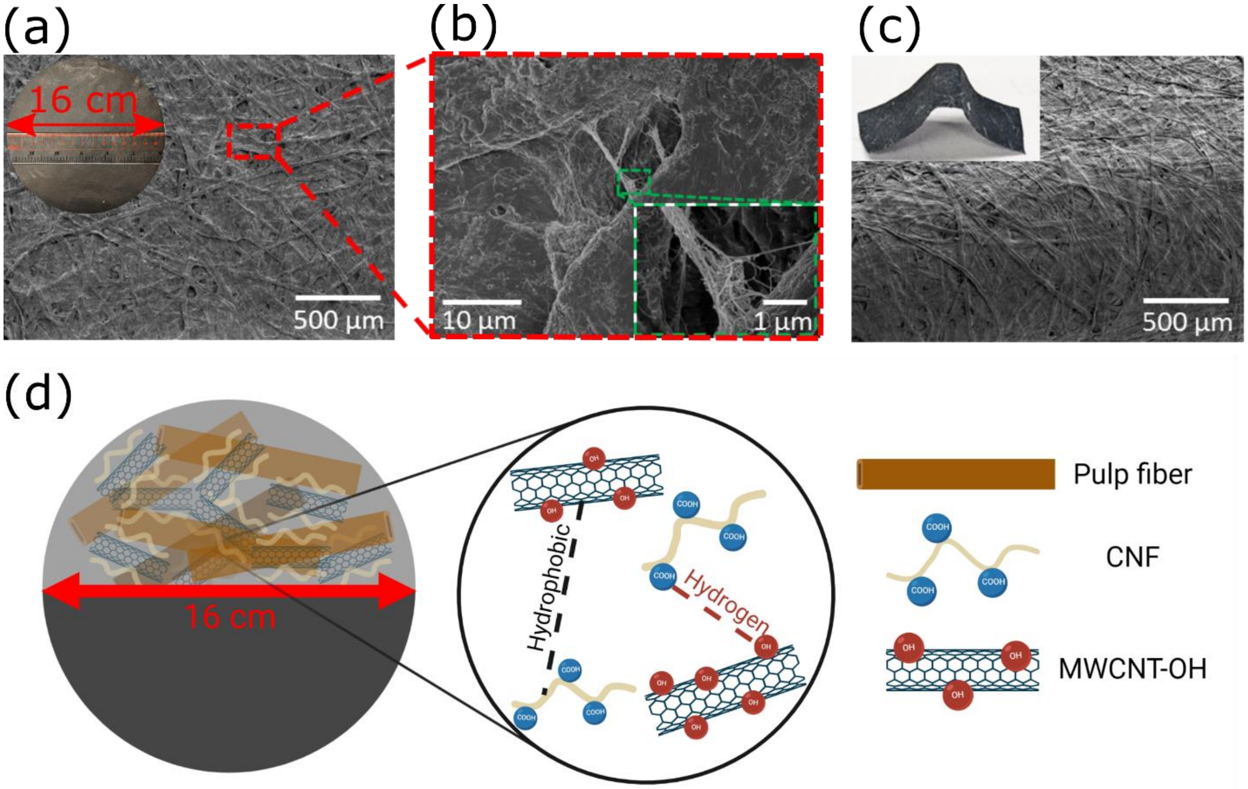

Figure 25. *Microstructure of paper nanocomposites*. Representative SEM micrographs of paper nanocomposites when flat (a-b) and after repeated bending (c). Photographs of the handsheets are shown in the insets. (d) Depiction of the paper microstructure and interfacial bonding (image created with BioRender).

This is attributed to the presence of CNFs playing two roles: (*i*) that of a dispersing agent for the hydrophobic CNTs and (*ii*) that of an interfacial reinforcing agent between the CNTs and the pulp fibers, as illustrated in **Figure 25d**. The former role can be ascribed to the polarization of electrons in the sp^2 CNT lattice induced by the fluctuations of counter-ions on the surface of the TEMPO-oxidized CNFs[62], which promotes the colloidal stabilization of CNT:CNF complexes in water by means of electrostatic repulsion and steric hindrance, as shown by absorption spectroscopy (**Fig. 22**). The latter role is evidenced by the red-shift observed with the addition of CNT:CNF complexes in the graphitic D-band around 1350 cm^{-1} of the Raman spectra of papers with the highest CNT content of 15 wt%, which is indicative of strong bonding interactions between the nanoparticles and the pulp fibers, shown in **Figure 26a**. The favorable interfacial properties are confirmed by tape peeling tests, where the thickness and the in-plane electrical resistance of paper nanocomposites with 15 wt% CNTs decreased respectively by less than 1 and 2% on average after peeling (**Fig. 26b**). Representative SEM images (**Fig. 26c-d**) show that the material removed during the peeling tests include both cellulose microfibers and CNTs, further confirming the strong interfacial properties achieved during sheet formation. The fortified interface between the different components allows the paper nanocomposites to maintain their structural integrity even after repeated bending (**Fig. 25c**).

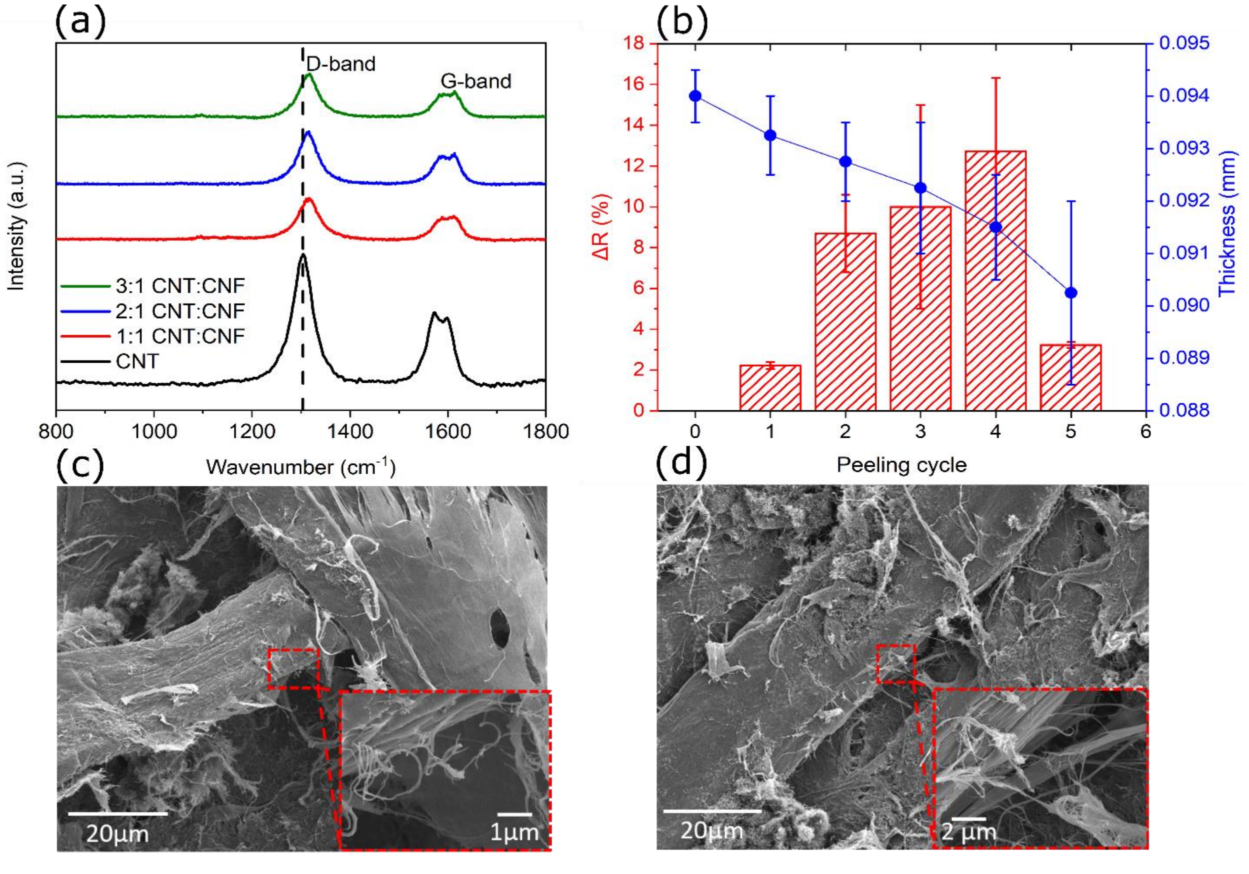

Figure 26. *Interfacial properties of paper nanocomposites*. (a) Raman spectra of 15 wt% paper nanocomposites prepared at different ratios. (b) Resistance and thickness changes of paper nanocomposites after each peeling cycle during the Scotch tape test. Representative SEM images of the (c) paper and (d) tape after the fifth peeling cycle.

The strong interfacial properties achieved within the paper nanocomposites also contributed to the ability to retain such high CNT contents (i.e. 15 wt%) with minimal nanoparticle loss, while typical reports indicate CNTs are no longer well-captured by cellulose fibers at this weight fraction and can be easily detached[124]. Paper nanocomposites were subjected to varying degrees of agitation in DI water to assess the extent of nanoparticle loss. UV-vis spectroscopy was employed to measure the absorbance of solution after agitation compared to a black counterpart of pure DI water. **Figure 27** indicates that after both soaking and stirring in solution for 24 hours, minimal to no CNTs were dislodge from the paper, as evidenced by the negligible absorbance. Although solutions that were bath sonication for 1 and 5 minutes do show an increase in absorbance compared to the soaked and stirred solutions, it can be seen from the optical micrographs that both CNTs and cellulose microfibers are being dislodged. This confirms that CNTs remain strongly attached to pulp fibers even after the cellulose fibers have been dislodged from the sheet, and make way for future work in understanding the environmental impact of deploying paper nanocomposites as remote water sensors.

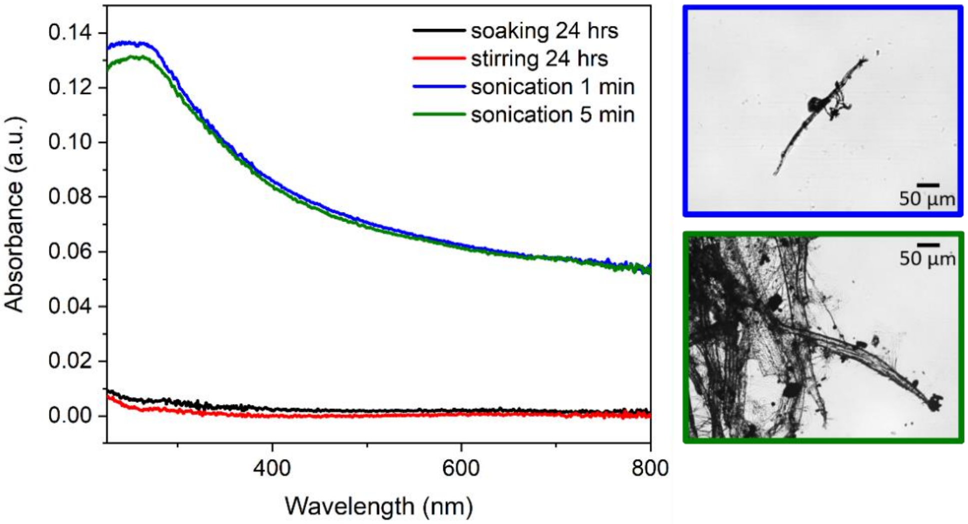

Figure 27. *Aqueous leaching study*. Aqueous leaching study depicted by optical absorption spectroscopy of solutions containing 1 cm^2 sections of 15 wt% 2:1 paper nanocomposites subjected to varying degrees of agitation in DI water. Insets show representative optical microscope images of sonicated solutions.

4.2.3 Optimization of paper nanocomposite composition on sensitivity to liquid water

Although strong interfacial properties allowed for CNT loadings as high as 15 wt% in preliminary work, a systematic study of the CNT content and ratio of CNT:CNF within the paper nanocomposites was performed to maximize the response of the composites to liquid water. Using CNF as a dispersing agent and bleached SW cellulose microfibers at a final paper grammage of 60 g/m^2, handsheets were prepared at CNT loadings of 5, 10, and 15 wt% with CNT:CNF ratios of 1:1, 2:1, and 3:1, and evaluated based on their sensitivity to liquid water. Papers were evaluated based on their relative resistance change (R_{rel}, %) defined as the ratio of the difference between the electrical resistances of the wet (R_t) and dry (R_0) specimen to the electrical resistance of the dry sample, as shown in the equation below:

$$R_{rel} = \frac{R_t - R_0}{R_0} * 100\% \qquad \textit{Eqn. 6}$$

As can be seen from **Figure 28**, the nanocomposites sensitivity to the presence of liquid water is highly dependent on not only the concentration of CNTs, but also the distribution of CNTs through the matrix, based on the ratio of CNT:CNF used. While handsheets prepared at higher CNT loadings (i.e. 10 and 15 wt%) exhibit an increase in R_{rel} when immersed in water, handsheets prepared with a 5 wt% CNT content exhibit either an unstable electrical response, or minimal change in R_{rel}, depending on the ratio. As was previously reported[19], at low CNT contents there are limited contacts between CNTs in the initial dry state, hence neighboring CNTs are actually pushed closer together as the cellulose matrix swells, resulting in an increase in conductivity (i.e. decrease in resistance). However, since an unstable or minimal increase in R_{rel} is observed, rather than a clear decrease, the evidence suggests a loading of 5 wt% is nearing closer to the percolation threshold than previous reports at 2.5 wt%[19]. At higher CNT loadings, a clear increase in R_{rel} is observed upon immersion in water, giving insight into the rate of swelling in the paper nanocomposites.

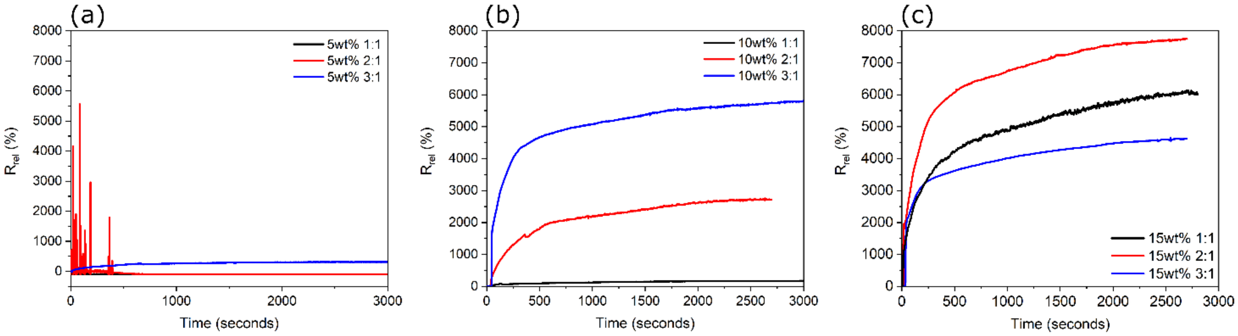

Figure 28. *Evaluation of liquid water sensitivity*. Relative resistance (R_{rel}) as a function of time immersed in DI water for (a) 5 wt%, (b) 10 wt%, and (c) 15 wt% CNT content handsheets prepared at three different CNT: CNF ratios.

Cellulose fibers are commonly understood to demonstrate two distinct swelling phases when immersed in water: an initial short but fast phase where the swelling rate reaches a maximum, followed by a longer and slower phase where the swelling rate approaches zero[147]. The resistive response of fully immersed paper sensors at 10 and 15 wt% CNT contents follows the same behavior, with a steep linear increase at short times before leveling off after a few minutes of exposure (**Fig. 28b-c**). Interestingly, while the sensitivity increases almost linearly with dispersion ratio (1:1, 2:1, 3:1) for the 10 wt% composites, this trend does not hold at a higher CNT content of 15 wt%. This indicates that the CNT dispersion ratio is not universal for paper nanocomposites, but is also dependent upon the concentration of CNTs. Of all CNT contents and ratios studied, composites prepared at 15 wt% with a 2:1 ratio achieved the highest sensitivity, reaching an R_{rel} of ~8,000% after 45 minutes of immersion.

In an effort to understand the difference in sensitivity of the composites prepared at different ratios, 15 wt% samples underwent additional characterization. X-ray diffraction angles of bleached pulp handsheets prepared with various CNT:CNF ratios, shown in **Figure 29**, reveal that the crystallinity index (CrI, %) is less significantly reduced by the presence of CNTs when a specific quantity of CNF is introduced in the composite, despite the same CNT content of 15 wt% being used in each case. This result suggests that a better dispersion state with higher degree of CNT individualization is achieved at the CNT:CNF ratio of 2:1, while more compact CNT loadings are obtained both below and above this value, hindering the formation of crystalline regions along cellulose chains, resulting in a greater decrease in crystallinity[67,151].

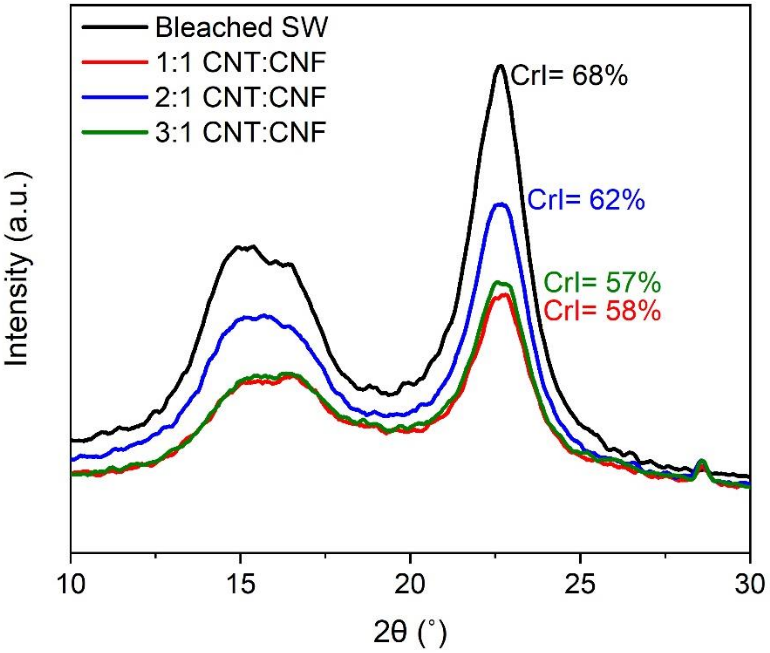

Figure 29. X-ray diffraction patterns of paper nanocomposites prepared at a CNT loading of 15 wt% with varying CNT:CNF ratios.

XRD results are consistent with electrical resistance measurements collected by four-point probe at 37 different locations across each sample sheet. The paper nanocomposites prepared at a CNT:CNF ratio of 2:1 yield the most uniform sheet resistance, as indicated by the narrow distribution curve compared to the other two ratios tested, shown in **Figure 30a**. The spatial distribution of the sheet resistance for a 15 wt% 2:1 ratio sample is shown in **Figure 30b** and indicates a relatively uniform surface which suggests an even distribution of CNTs throughout the sheet.

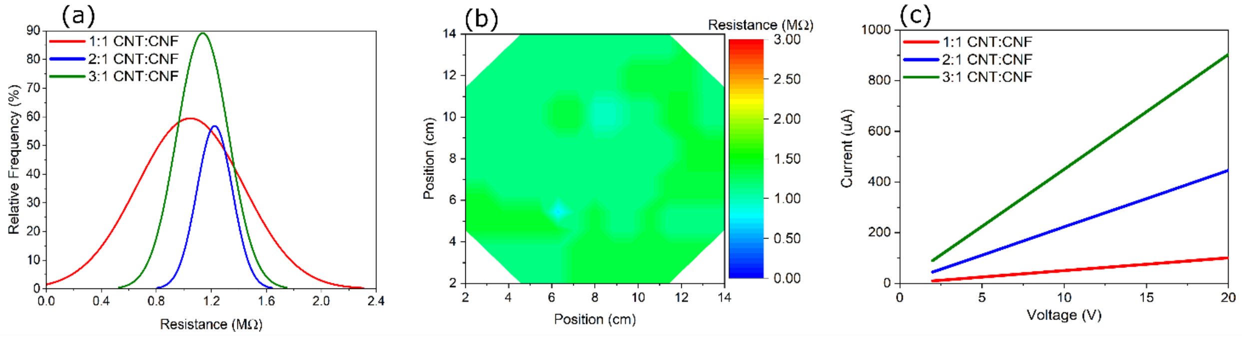

Figure 30. *Electrical characterization of 15 wt% paper nanocomosities with varying CNT:CNF ratios*. (a) Histograms of resistance measurements collected by a 4-point probe method at 37 locations across each sample for all three CNT:CNF ratios. (b) Spatial distribution of electrical sheet resistance of a 2:1 CNT:CNF nanocomposite collected by 4-point probe. (c) Current-voltage (I-V) characteristics of paper nanocomposites prepared at 1:1, 2:1, and 3:1 CNT:CNF ratios.

Moreover, while the current-voltage characteristics of paper nanocomposites exhibit linear Ohmic behavior with excellent stability (**Fig. 30c**), the initial dry resistance of the u-shaped samples used in liquid sensing tests vary across all three ratios. As the CNT content is kept at a constant 15 wt% across all samples, the amount of conductive material remains constant. Only the ratio of CNT:CNF is varied from 1:1, 2:1, or 3:1 between the samples, indicating the distribution of CNTs as the only changing variable. These observations confirm what was seen by XRD and 4-point probe analysis, that the distribution of CNTs within the cellulose matrix varies as a function of CNT:CNF ratio. These results are in agreement with the proposed percolation theory governing the electrical resistance response at different CNT contents and distributions upon the swelling of cellulose[152]. The material composition for future handsheet preparation was selected as 15 wt%

at a 2:1 CNT:CNF ratio based on its superior sensitivity to water, achieved through an optimized distribution of CNTs throughout its matrix.

The sheet density and porosity are other important factors governing the resistive response of materials to liquids.[133,153] In low density sheets, the fibers can occupy the surrounding empty space when swollen.[67] As the sheet density increases, the spacing between fibers decreases and the number of interfiber contacts increases. Therefore, there is an optimum sheet density to maximize the disruption of the percolated electrical network on the surface of individual fibers, while minimizing the reformation of CNT junctions between adjacent fibers. Here, sheet density and porosity are indicated by the grammage (g/m^2), a common metric used by the pulp and paper industry for conveying the area density of paper products.

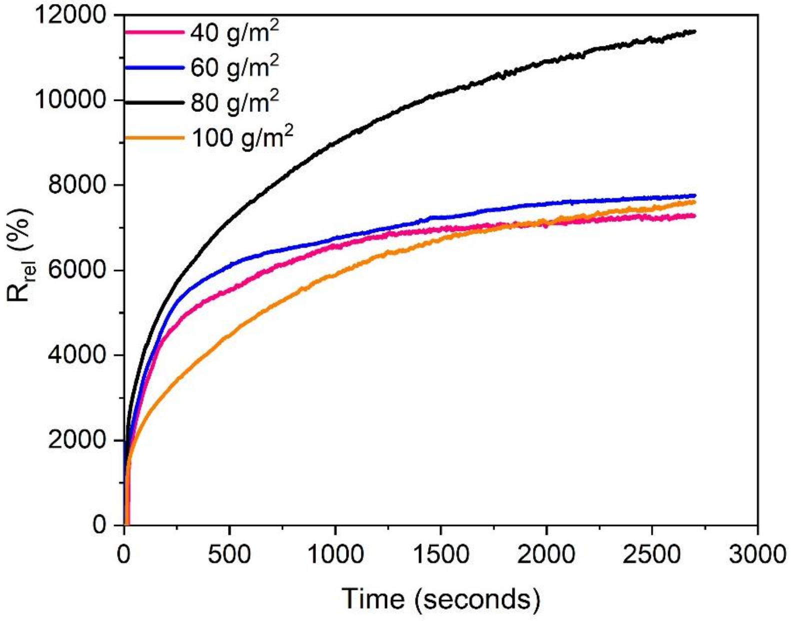

Figure 31. Effect of grammage on relative resistance (R_{rel}) response. Relative resistance (R_{rel}) as a function of time immersed in DI water for 15 wt% 2:1 paper nanocomposites prepared at varying grammages.

As can be seen in the plot in **Figure 31**, compared to the 15 wt% 2:1 60 g/m^2 sample that has been previously studied in this text, the 80 g/m^2 sample exhibits a much higher electrical response to the presence of liquid water due to an optimized sheet porosity and density, achieving one of the highest sensitivities reported to date[19,63,67,120,154–156]. Although the 80 g/m^2 sample achieved a higher sensitivity, in an effort to minimize material usage and maintain high nanoparticle retention, additional samples were prepared at 60 g/m^2 for all additional batch scale multifunctional aqueous sensing measurements.

4.2.4 Multifunctional liquid sensing applications

Paper nanocomposites, prepared at a 15 wt% 2:1 60 g/m^2 composition, were applied as multifunctional resistive sensors in aqueous environments, as illustrated in **Figure 32**. Optimized material composition, resulting in record sensitivity to liquid water, enabled the detection of water volumes as small as 0.25 µL with great accuracy (**Fig. 32-droplets**). This can be attributed to the unique swelling behavior of cellulose in the presence of water – the diameter of pulp fibers in water increases by 28% on average compared to their original drying state after only 30 seconds of immersion (**Fig. 23**). While conventional sensors rely on changes in charge carrier concentration due to adsorbed water molecules, the swelling mechanism of cellulosic fibrous network allows for dramatically faster and greater responses. The presence of free water molecules can affect the interfiber spacing by disrupting hydrogen bonding between adjacent pulp fibers, although its contribution to the sheet hydroexpansion is negligible compared to the swelling of individual fibers[120,133,157]. Based on the solvent-specific swelling response that was seen for bleached SW fibers (**Fig. 23**), the paper nanocomposites have the necessary sensitivity and specificity to detect the presence of water in organic solvents (**Fig. 32-organic solvents**). The detection limit is as low as 250 ppm for water in toluene, which is comparable to fluorescence methods reported in the recent literature[158]. The temperature of aqueous solutions can also be measured accurately and reliably based on linear relationships between the electrical resistance and the liquid temperature with correlation coefficients approaching unity regardless of the sensing time (**Fig. 32-temperature**).

The presence of ionic species in solution is another important factor influencing the resistive response of paper nanocomposites. The effect of salinity on the sensing performance is studied using sodium chloride solutions to simulate seawater (**Fig. 32-ionic strength**). Results reveal that the signal intensity decreased with the increase of salt concentration. This can be attributed to the reduced Donnan osmotic pressure between the porous paper structure and the external solution at high salt concentrations, which is caused by the ionic interactions between mobile ions and the fixed charges on the cellulosic material[147]. This result explains the different sensitivity values obtained in deionized and tap water. Furthermore, the paper nanocomposites exhibit the same predictable electrical response with correlation coefficients approaching unity when immersed in either deionized or tap water spiked with sodium chloride ranging from 0.05 to 1 wt.%. Beyond this concentration range, the salt quantity is either too low or the solution conductivity is too high to yield statistically significant variations in electrical resistance.

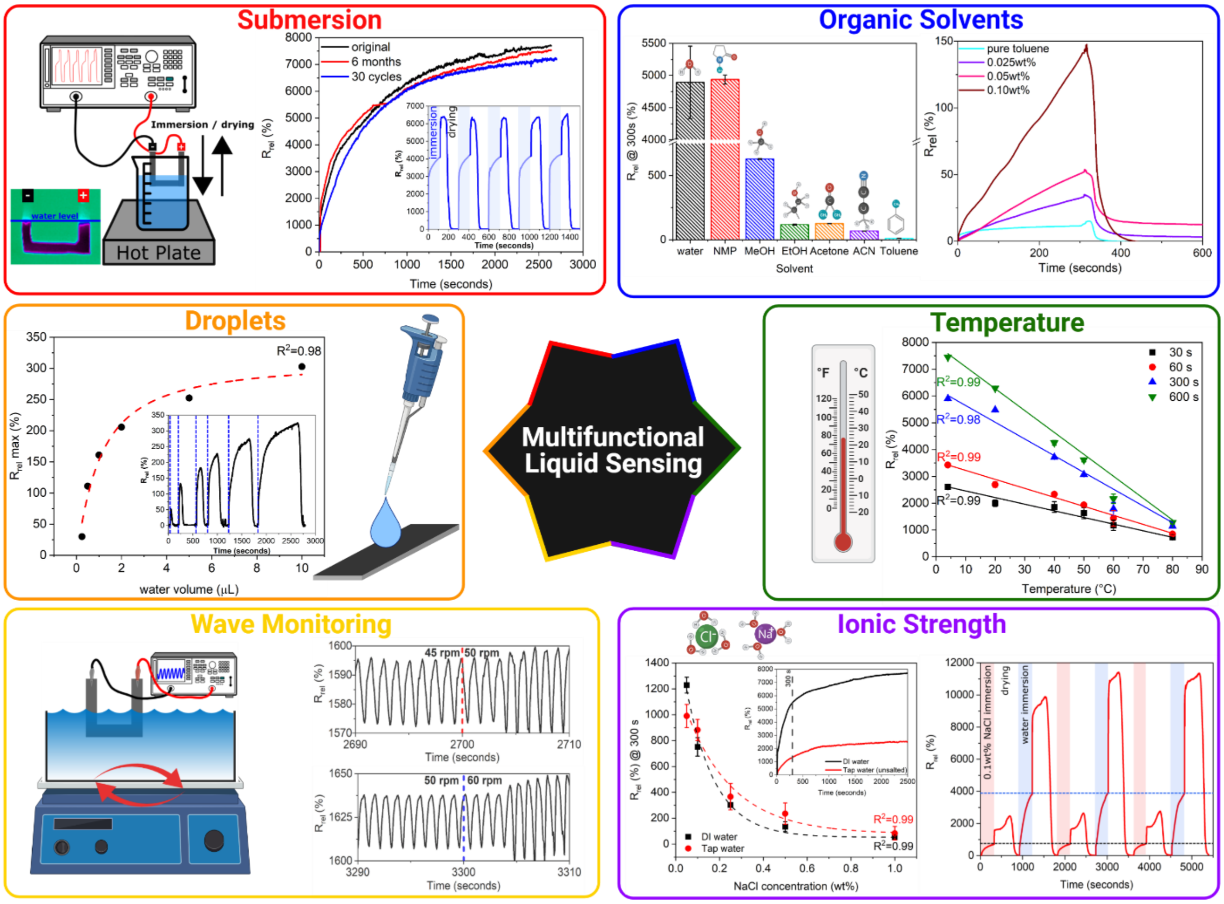

Figure 32. *Multifunctional liquid sensing performance of nanocomposites with 15 wt.% and 2:1 CNT:CNF ratio.* (*Submersion)*: The apparatus used for the submersion analysis includes thermal imaging to ensure there was no direct contact between the electrodes and the test solution. R_{rel} as a function of time immersed in DI water for a pristine and a 6-month aged specimen after their first and 30th immersion/drying cycle. Inset shows the time profile for the first 5 immersion/drying cycles. (*Droplets)*: The maximum R_{rel} achieved for small volumes of DI water incrementally drop casted onto the sensor (0.25, 0.5, 1, 2, 5, and 10 µL), with the corresponding time profile shown in the inset. (Wave *Monitoring)*: R_{rel} as a function of time immersed in DI water under constant agitation using an orbital shaker successively operated at 45, 50 and 60 rpm. (*Organic Solvents)*: R_{rel} response at 300 s of immersion in various solvents (left graph) and R_{rel} time profile for different mixtures of water in toluene with increasing water content from 0.025 to 0.10 wt% (right graph). (*Temperature)*: Linear relationship of relative resistance response (R_{rel}) as a function of liquid temperature at increasing immersion times of 30, 60, 300, and 600 seconds in DI water. (*Ionic Strength)*: Evolution of R_{rel} at 300 s with the NaCl concentration of DI and tap water solutions, fitted with a power law. Inset shows the time profile in pure DI and tap water (left graph). R_{rel} as a function of time for 6 immersion/drying cycles in alternating solutions of 0.1 wt.% NaCl and DI water (right graph).

The expansion mechanism of cellulose fibers is fully reversible, as evidenced by XRD and optical microscopy (**Fig. 33**). As liquid successively enters and leaves the material, the cellulose chains either move apart or drew closer together, altering the electron transport by varying the intertube distance between neighbored CNTs above or below the critical tunneling distance, which is approximately 1.8 nm, indicated by the shift in the XRD spectra[19,130,159,160]. This translates to very reproducible sensing responses over at least 30 immersion/drying cycles (**Fig. 32-submersion**).

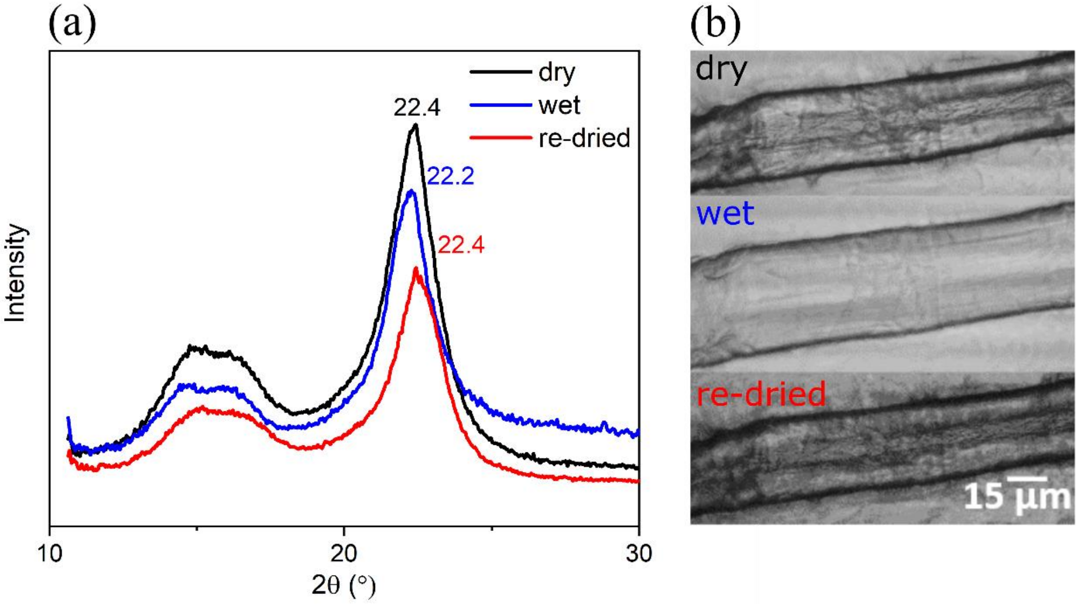

Figure 33. *Reversibility of cellulose expansion mechanism.* (a) X-ray diffractograms of pristine bleached softwood fibers when dry, immersed in water for 30 seconds, and re-dried and (b) Optical microscopy images of the corresponding dry, wet, and re-dried samples.

Notably, the sensor performance is not affected by aging and similar signals are obtained with the same paper-based sensor after a six-month interval. Sensing stability also remains excellent after multiple immersion/drying cycles in alternating aqueous solutions containing various levels of salts (**Fig. 32-ionic strength**). Furthermore, Laplace pressure increases as the water is withdrawn from the paper, bringing pulp fibers closer to each other through capillary forces[161]. This rapid reorganization of the wet fibrous network contributes to fast response times, enabling applications like wave monitoring and water level measurement. The former, exemplified in **Figure 32-wave monitoring**, shows consistent variations in the signal period with the rotation speed of the wave generator. When the rotation speed increases by 11% (*i.e.* from 45 to 50 rpm) and 20% (*i.e.* from 50 to 60 rpm), the average signal period is raised by 10% (*i.e.* from 1.22 to 1.11 s) and 19% (*i.e.* from 1.11 to 0.90 s), respectively. The latter reveals that the electrical resistance of the paper nanocomposites varied linearly with the depth of immersion, exhibiting a sensitivity of 45 kΩ/mm and a correlation coefficient of 0.97, as shown in **Figure 34**. This implies that resistive paper sensors can monitor liquid levels in the millimeter range, which can be beneficial in various applications, such as offshore engineering constructions, overflow prevention systems and early warning of marine disasters[162,163].

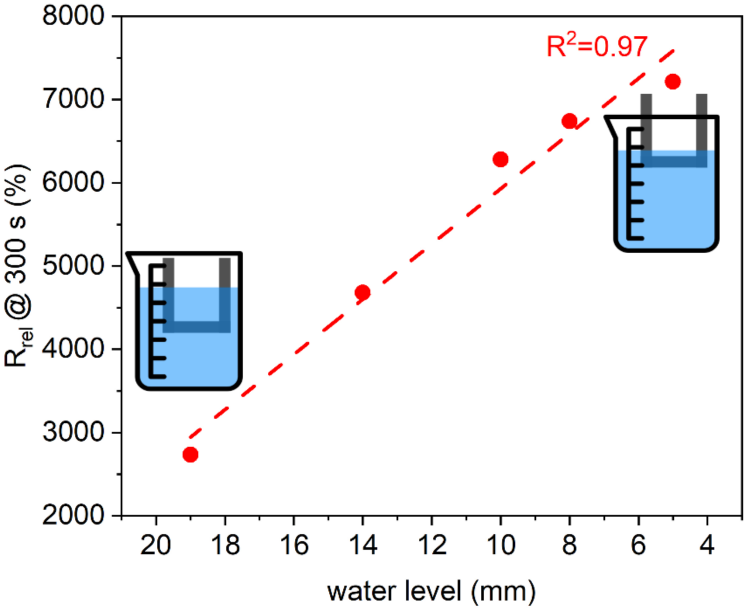

Figure 34. *Relative resistance response (R_{rel}) as a function of immersion depth in DI water.* A U-shaped sample was initially immersed 19 mm into DI water, and then subsequently raised out of the water every 300 s to a final immersion depth of 5 mm. The electrical response was continuously monitored by a Keithley 2450 voltage-current meter. Similar setups can be implemented as applications in overflow monitoring systems.

4.3 Conclusion

‘Smart’ paper nanocomposites have been optimized for aqueous sensing applications by controlling the type of cellulose microfiber and dispersing agent, CNT content, CNF:dispersant ratio, and paper grammage. The use of CNF not only as a dispersing agent, but also as an interfacial reinforcing agent, promotes the uniform distribution and retention of CNTs, allowing for CNT loadings as high as 15 wt% with minimal nanoparticle loss to the aqueous environments being sensed. The combination of bleached cellulose microfibers and CNF in the composite matrix contribute to a hierarchically swellable structure due to the hygroscopic nature of cellulose, resulting in one of the highest sensitivities to liquid water reported to date (R_{rel} ~12,000%). While conventional sensors rely on changes in charge carrier concentration due to adsorbed water molecules, the swelling mechanism of cellulosic fibrous network allows for dramatically faster and larger magnitude responses. Heightened sensitivity enables small volume detection, as low as 0.25 μL, suggesting optimized paper nanocomposites can be employed as reliable water detectors. Sustainable cellulosic composites, made via a facile paper making technique, show promise as inexpensive and biodegradable water sensors.

V. Chapter 3: Scalable manufacture of ‘Smart’ paper nanocomposites

Note: This work is under review as a portion of an article submitted to NanoToday in April 2021.

Abstract

Cellulose-based paper electronics is an attractive technology to meet the growing demands for naturally abundant, biocompatible, biodegradable, flexible, inexpensive, lightweight and highly miniaturizable sensory materials. The price reduction of industrial carbon nanotube (CNT) grades offers opportunities to manufacture electrically conductive papers whose resistivity is responsive to environmental stimuli, such as the presence of water or organic solvents. Here, the fabrication of paper nanocomposities is adapted from the batch scale and produced using an aqueous-phase dynamic web forming process which enables the scalable production of sensory paper nanocomposites with minimal nanoparticle loss due to the tailored interfacial bonding between CNT and cellulose components. The resulting material is applied in a remote leak detection device. The re-organization of percolated CNTs modifies the electron transport in wet areas of the sheet, behavior which can be predicted by an equivalent circuit of resistors for the rapid detection and quantification of various liquids over large surfaces.

5.1 Introduction

While a fifth of the world’s population lacks access to clean drinking water, inadequate infrastructure and unidentified leaks are major contributors to the global water scarcity crisis. The Environmental Protection Agency (EPA) reports that an estimated 16-30 % of treated water is lost during transportation due to crumbling pipeline infrastructure, leading to unidentified leaks[164,165]. The American Society of Civil Engineers indicates that about a quarter-million water line breaks occur each year in the U.S., costing public water utilities up to $2.8 billion annually[138]. Worldwide, the World Bank estimates that global non-revenue water, which refers to the cost of water lost to leaks and billing errors approaches $14 billion. Ideally, a leak monitoring system would consist of a low cost array of optimally spaced remote sensors to minimize the reaction time to patch a leak and power off sensitive instruments when necessary. However, sensing liquid water in a reliable and affordable way poses a major challenge. Existing technologies remain expensive and either have weak or slow responses to water due to the non-polar nature of the materials employed, or are partially soluble in water, like most polymer-based systems, which produce inconsistent signals due to material degradation in aqueous environments[77–82].

Cellulosic paper, given its biodegradability, flexibility, and low cost, provides an excellent platform for building sustainable and affordable liquid water sensors with favorable performance. To date, most efforts have focused on hosting various types of conductive electrodes on the surface of a pre-prepared cellulose matrix[73,140–142]. However, these methods are characterized by low accuracy and non-uniformity, on top of making production at the larger scale extremely challenging and expensive. Previous work has demonstrated the superior performance of embedding electrically conductive carbon nanotubes (CNTs) into the fiberous cellulose matrix prior to sheet formation, offering greater control over the percolated network[19]. However, the process of embedding nanoparticles in commercial-scale papermaking remains a challenge as the viscosity must be controlled, dewatering should remain fast to achieve uniform sheet formation, and nanoparticle loss through existing filter membranes can be profound at high processing speeds[166]. The present research describes the fabrication of electro-conductive papers adapted from the batch scale for an easy-scale-up process involving the continuous-flow filtration of cellulosic suspensions. Aqueous suspensions of wood pulp pre-adsorbed with alternatingly charged suspensions of CNTs and cetyl-trimethylammonium bromide (CTAB, +) or alkali lignin (AL, -) are combined to establish a layer-by-layer assembly process for the formation of structured fibrous mats, which are further dewatered by subsequent pressing and drying. A key element of this approach involves the unique binding chemistry between oppositely charged ‘layers’, ensuring strong adhesion between the nanoparticles and the pulp fibers, even at loadings as high as 18 wt.%. This allows the manufacture of paper nanocomposites using a pilot-scale web former, mimicking industrial papermaking conditions with minimal nanoparticle loss. Resulting pilot-scale-produced paper nanocomposites are evaluated as remote leak detectors when used in tandem with an inexpensive microcontroller, which can be modelled as an equivalent circuit of resistors for the rapid detection of small-volume leaks over wide areas.

5.2 Results

5.2.1 Characterization and sensing performance of pilot-scale-produced nanocomposites

In continuous flow processing, colloidal retention and dewatering time are frequently identified as limiting factors for sheet formation[166]. Since the pore size of the wire screen on the pilot-scale machine is too large to retain the nanoparticles, filler retention is promoted by mechanical entrapment and electrostatic adsorption. First, the sheet grammage is increased from 60 to 80 g/m^2 and 25 wt% bleached hardwood (HW) pulp is incorporated into the paper composition to diminish the number and size of pores in the fibrous mat[167]. Then, the CNT feed is split into two filler streams of opposite charges to enhance electrostatic interactions between CNTs and pulp fibers based on the previously reported layer-by-layer nanoassembly technique.[19] The first filler addition comprises a cationic dispersion of CNTs and Cetyl Trimethyl Ammonium Bromide (CTAB 5 wt%, 2:1), which is supplied at the fan pump to ensure sufficient time and shear forces for adequate mixing with the anionic pulp. The second filler addition consisting of an aqueous mixture of CNTs and anionic alkali lignin (AL) is introduced prior to entering the forming section (**Fig. 35**).

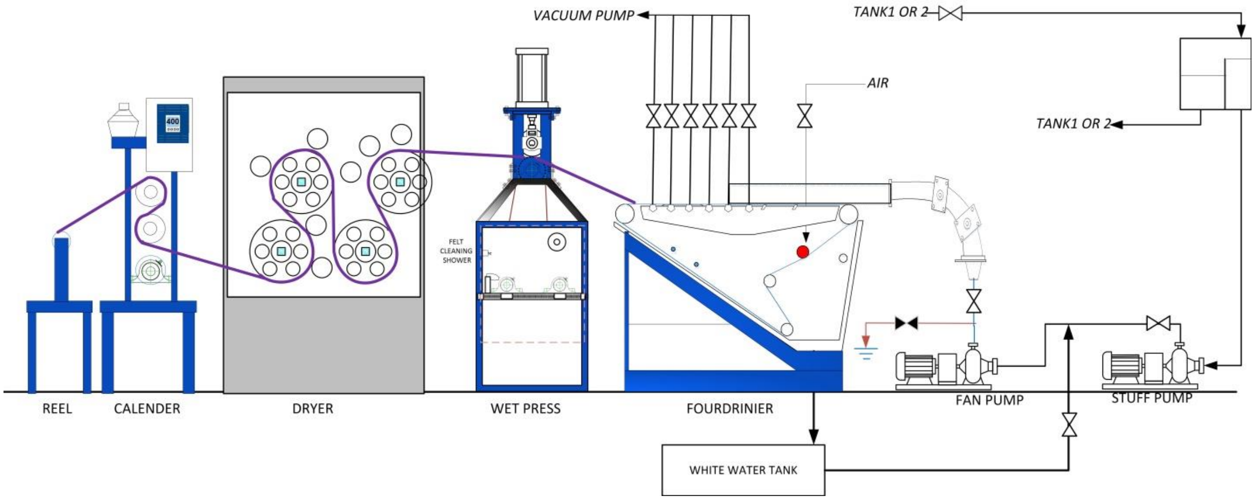

Figure 35. *Process flow diagram of pilot-scale web former.* Softwood and hardwood fibers were prepared in tank 1 and combined with the aqueous CNT:CTAB and CNT:AL dispersions (5 wt%, 2:1) at the fan pump prior to sheet formation. The machine was operated at 3.2 m/min and the formed sheet was dewatered by subsequent pressing and drying. More than 70 meters of paper nanocomposite with 18±2 wt% CNT were produced in this continuous flow fashion.

As a result, the wood pulp is modified by the successive adsorption of alternating layers of oppositely charged CNTs on the surface of cellulose fibers. CNTs that are not retained in the fibrous mat during their first pass are recirculated back to the web forming section to minimize nanoparticle loss. This approach yields CNT retention higher than 90% in the final sheet. Given the non-polar nature of CNTs, the dewatering was fast, enabling an operating speed of 3.2 m/min with excellent sheet formation and uniform CNT distribution, as indicated by the photo and SEM inset shown in **Figure 36a**. Paper nanocomposites were cut from the full length of material produced to generate sheets with dimensions of 30 cm x 80 cm and exhibit homogeneous sensing performance with negligible change in sensitivity along the width and less than 10 % variation along the length (**Fig. 36b**). Notably, when the sensing performance is compared to that of a batch-scale produced handsheet with at the same composition and density, there is no loss in sensitivity when produced on a continuous-flow system.

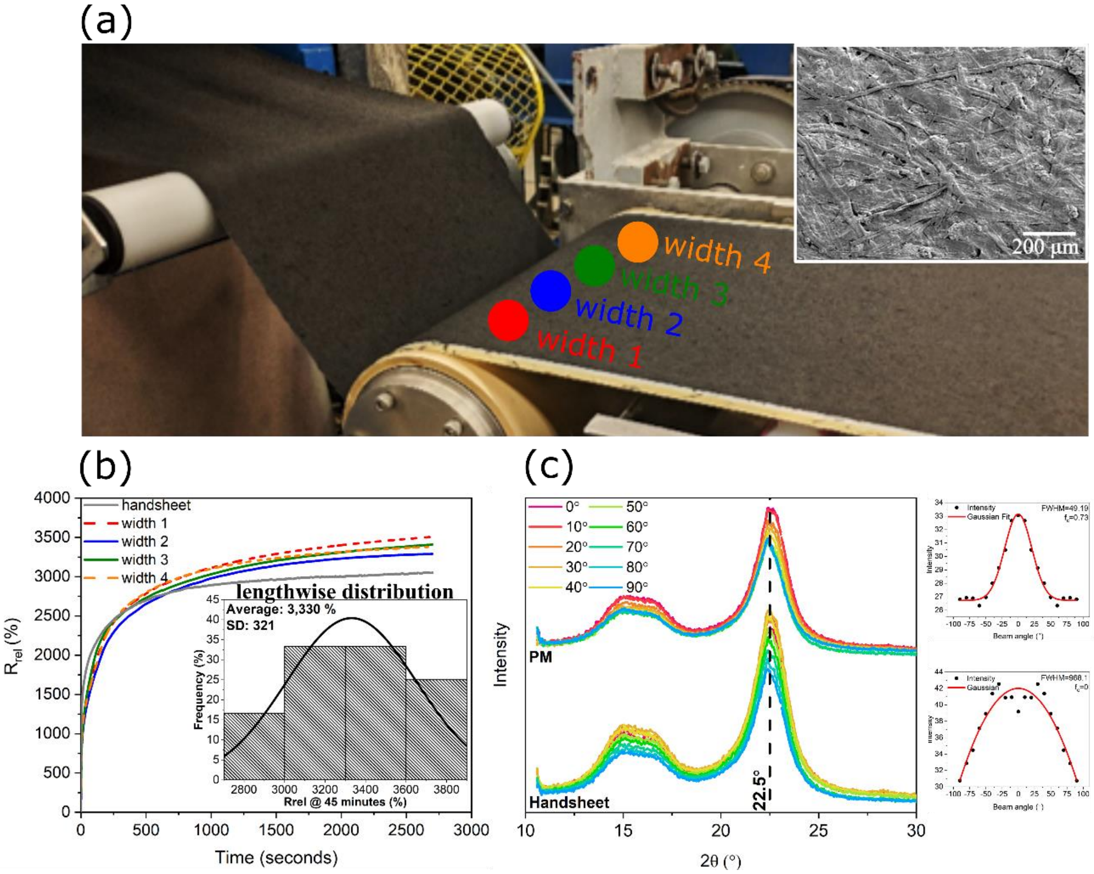

Figure 36. *Structural characterization and sensing performance of continuous flow processed paper nanocomposites*: (a) Photo of the pilot-scale dynamic web forming process, with a representative SEM image in the inset. (b) Relative resistance response (R_{rel}) as a function of time immersed in water for samples taken across the full width (30 cm) of the sheet, compared to similar samples prepared at the bench scale. The inset demonstrates the relatively narrow lengthwise distribution in sensitivity along the 70m long sheet with over 35 replicates. (c) 2D-XRD profiles of paper nanocomposites produced by continuous-flow and batch scale processes, where the beam angle was rotated from 0 (in direction of continuous flow) to 90° (perpendicular to flow). The insets show the azimuthal integration of the peak at 22.5° with respect to beam angles.

Unlike in batch processing, the dynamic web forming method induced the alignment of pulp fiber along the machine direction creating anisotropic sheets, as demonstrated by 2D-XRD measurements collected at 10° increment beam angles with the paper from 0 (in machine direction) to 90° (perpendicular to machine direction) (**Fig. 36c**). Insets indicate the azimuthal integration of the cellulose crystalline peak at 22.5° with respect to beam angles. *Fc* values of 0.73 and 0 calculated for pilot- and batch-scale respectively, indicate some degree of fiber alignment during dynamic web formation, as an *Fc* value of 1 indicates perfect alignment and an *Fc* value of 0 is characteristic of no alignment, or a randomly oriented fibrous network.

Tensile testing indicates that mechanical strength is improved when the stress is applied in the direction of the fiber alignment compared to when fibers are oriented perpendicularly to the applied stress (**Fig. 37a**). When randomly oriented, a the strength of a paper sheet relies upon the interfiber hydrogen bonding achieved during mixing aqueous pulp suspensions, and the innate fiber strength remains untapped, resulting in low ultimate tensile strengths. However, with the alignment of cellulose fibers in the direction on an applied stress, the innate fiber strength can contribute to the strength of the overall composite as fibers now have an almost infinite number of interfaces at which to slide over one another, maintaining contact through intact interfiber hydrogen bonds[168,169]. While this preferred orientation of pulp fibers in the sheet has a clear impact on the mechanical properties (**Fig. 37a**), the resistive response of the paper sensor to water remains isotropic (**Fig. 37b**).

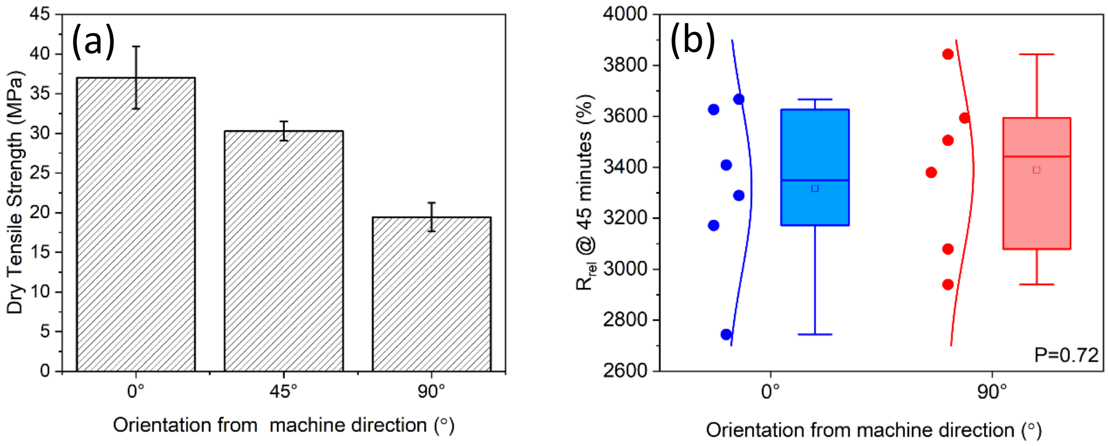

Figure 37. *Effect of fiber orientation on mechanical and electrical properties.* (a) Tensile strength of anisotropic paper nanocomposites produced by pilot-scale web forming as a function of the angle between the stretching direction and the fiber orientation in the sample. At 0°, the pulp fibers are aligned parallel and perpendicular to the stretching direction, respectively. (b) Statistical analysis comparing the means of maximum relative resistance achieved after 45 minutes of immersion in DI water for specimens prepared with different fiber orientations. At 0° and 90° orientations, fibers are aligned vertically and horizontally along the bottom part of the immersed U-shaped samples, respectively. The calculated p-value of 0.72 at a 95% confidence level confirmed that the resistive response of paper nanocomposites to water remained isotropic.

5.2.2 Application of pilot-scale-produced nanocomposites as remote leak detectors

Successful continuous pilot-scale processing, with maintained sensitivity compared to the batch scale, indicates that paper nanocomposites show promise as scalable liquid water sensors. As water damage due to unrecognized leaks is one of the major insurance claims made by homeowners each year[170,171], and water loss along transportation pipelines accounts for a majority of treated water waste in the U.S., the use of paper nanocomposites as remote water leak detectors is of great interest. To demonstrate their comercializability, an inexpensive and portable leak monitoring system was developed using paper nanocomposites in tandem with an inexpensive NodeMCU microcontroller. The 'If This Then That' (IFTTT) platform was used to send wireless text messages to a remote cell phone or computer as soon as the presence of liquid was detected through a hole in the pipe, indicative of an active leak (**Fig. 38a**). The response times of the remote leak detection system were on the order of seconds and the system remained operational with pipes and surfaces of various material and size by adequately adjusting the resistance threshold for triggering an alert to compensate the reduced sensitivity caused by bending or/and by contact with an electrically conductive surface (**Fig. 38b**).

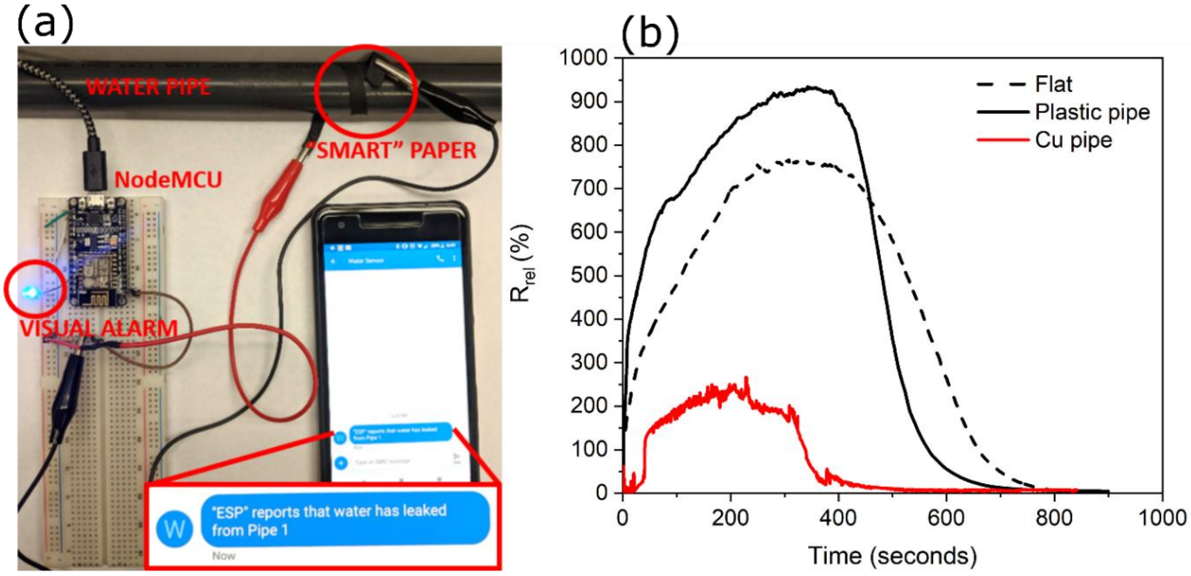

"ESP" reports that water has leaked from Pipe 1

Figure 38. *Versatility of remote water leak detector*. (a) Depiction of remote water leak detector system comprising paper nanocomposite and NodeMCU microcontroller. Image indicates when water has just been sensed as visual (LED) and electronic alerts (text message) are displayed. (b) Time profile of the relative resistance response (R_{rel}) for flat and bent paper nanocomposites exposed to 10 µL of DI water. Water was applied at t=0 seconds, and the electrical response was monitored continuously by a Keithley 2450 voltage-current meter. Samples were either lying flat or bent around insulating (plastic) or conductive (copper) pipes.

To evaluate real-world performance, pilot-scale-produced paper nanocomposites were tested in collaboration with a team at the CERN ATLAS facility in Switzerland, where the papers served as leak detection devices. The rapid and reliable detection of water is of great importance at CERN, as a vast network of water coolant pipes extend over miles throughout an underground cavern, populating server racks that host read-out electronics and power supplies for high energy physics experiments, distributed between two floors. One of the major leak-related issues conveyed by

CERN is the tendency for second-level leaks to penetrate the permeable floor, extending the reach of the liquid to the floor below. As experiments in this facility can span years, the impact of a transient leak is not limited to the monetary cost associated with damaged hardware, but the intellectual value of any data stored on the now-destroyed equipment as well. Engineers collaborating on this project indicated that they needed a new leak monitoring system that could rapidly and reliably detect a leak from both a coolant water pipe and within the racks under read-out electronics, which could trigger an immediate shut down sensitive equipment to prevent irreplaceable damage. Given the flexible nature of the as-prepared paper nanocomposites, they are able to conform to a sensor design of virtually any shape. To mimic practical applications, the leak monitoring device was placed around a 30-cm wide section of a 13-cm diameter metallic pipe in an underground cavern of the CERN ATLAS facility and tested over a 30-hour period (**Fig. 39**). Water from the cooling water circuit was drop casted (0.25 mL) onto the pilot-scale produced paper nanocomposite to stimulate a leak 8 hours into the 30-hour testing period.

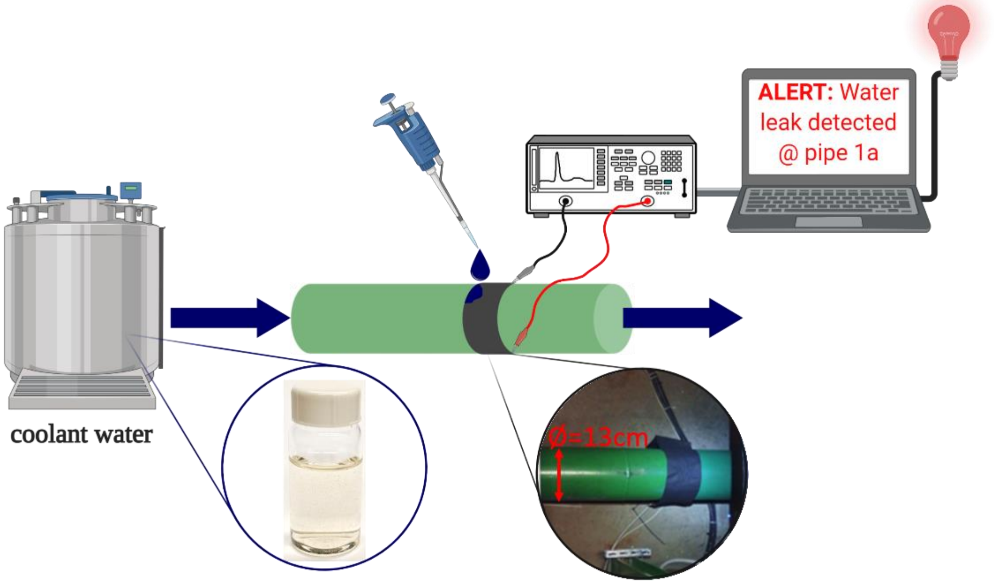

Figure 39. Schematic depicting the implementation of paper nanocomposites at CERN ATLAS facility Paper nanocomposite is connected to a Raspberry PI that runs an OPC UA server capable of sending alerts to the ATLAS Detector Control System upon the detection of water in an underground network of cooling pipes at the CERN facility.

Figure 40 reveals that the sub-milliliter leak is clearly identified despite fluctuations in humidity (10%) and temperature (~3 °C). A chasing average algorithm (ESI) was employed by ATLAS engineers as an additional signal processing technique to prevent false positives in remote leak detection, given the possibility of even greater fluctuations in temperature and humidity in their underground facilities. These results demonstrate that the as-prepared leak sensors are capable of rapidly detecting water leaks of very small volumes and can both monitor large surfaces as well as be deployed in spaces with a complicated geometry by enabling 2D or 3D surface sensing, moving away from single point detection.

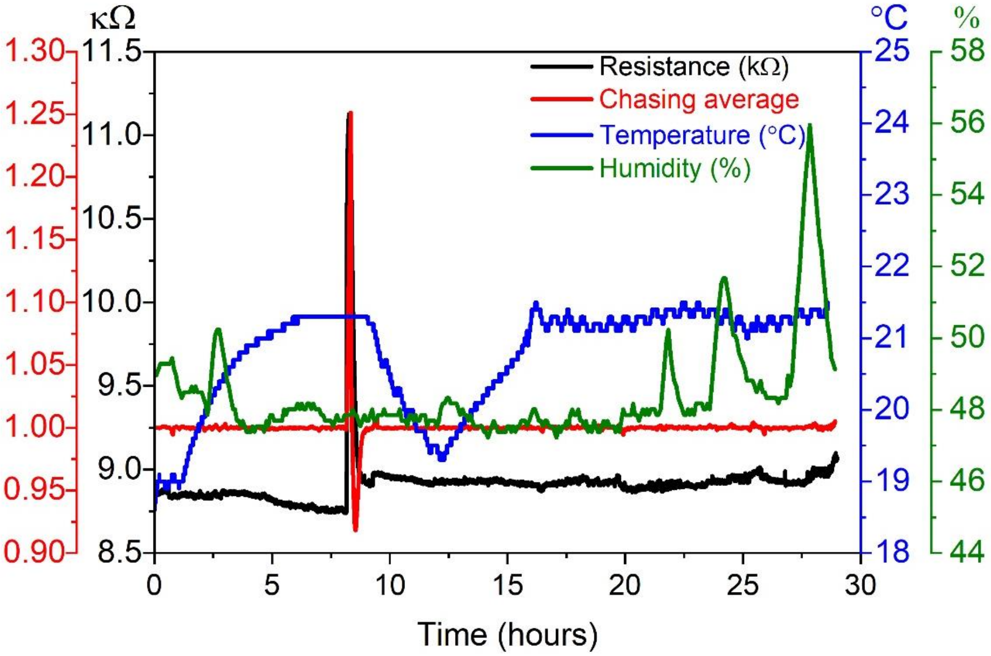

Figure 40. *Long term stability test*. Raw electrical resistance and processed response using a chasing average algorithm for a 30 cm x 80 cm sheet wrapped around a pipe and exposed to 0.25 mL coolant water.

To explore the concept of surface detection further, the sensitivity of 30 cm x 80 cm sheets is examined as a function of the relative wet area, which is computed by image analysis of the wet samples (**Fig. 41a**). Two linear regimes are clearly observed depending on whether water bridges both ends of the sensor width perpendicular to the direction of the electrodes. When water completely crosses the width of the sensor, the linear resistive response exhibits a steeper slope, indicating that the paper nanocomposites are more sensitive to variations in relative wet area in the full wet width regime. In this case, the resistive signal becomes linearly proportional to the relative wet length regardless of the sensor dimensions (**Fig. 41b**). This result is consistent with the linear relationship observed between sensitivity and depth of immersion in the fully submerged experiments. On the other hand, when the sensor width was partially wet (**Fig. 41a-inset**), the electrical response has a lower slope and is predominantly sensitive to the relative wet width (**Fig. 41c**). Both regimes can be modeled by dividing the paper width as a set of parallel resistors, which are linked in series along the length of the sheet, represented as an overall equivalent resistance (R_{eq}) of the paper nanocomposite. *Equation 7* shows the relationship between R_{eq} and an *MxN* matrix, where *M* and *N* represent the length and width of the sample in centimeters, respectively.

$$R_{eq}(M) = R_{eq}\begin{bmatrix} r_w & r_w & r_d \\ r_w & r_w & r_d \\ r_w & r_w & r_d \\ r_d & r_d & r_d \\ r_d & r_d & r_d \\ r_d & r_d & r_d \end{bmatrix} \qquad \textit{Eqn. 7}$$

As water spreads through the paper, the value of the resistors gradually shifts from dry to wet levels, thereby increasing the equivalent resistance of the sensor. A step change is apparent when a low-resistance path through a parallel group of resistors is no longer available (*i.e.* full wet width). In this case, the equivalent resistance increases abruptly and its relationship with the wet area enters a second linear regime, where the electrical response becomes proportional to the relative wet length of the sensor. The dry resistance (r_d) was calibrated for each sample by solving

Equation 8 for R_{ij} based on the measured R_{eq} operating under the assumption that in the dry state, r_d remains constant. *Equation 8* defines the model as a group of parallel resistors along the width in which are in series along the length of the paper nanocomposite.

$$R_{eq} = \sum_{i}^{n}\left(\sum\nolimits_{j}^{m}\frac{1}{R_{ij}}\right)^{-1} \qquad \textit{Eqn. 8}$$

The simulated change in resistance (ΔR) is then obtained by the difference between the wet (R_{eq}^{wet}) and dry (R_{eq}^{dry}) resistances, as reported in *Equation 9*.

$$\Delta R = R_{eq}^{wet} - R_{eq}^{dry} \qquad \textit{Eqn. 9}$$

This simple model agrees very well with all experimental data as long as the sensor is not saturated with water, which happens when the relative wet surface approaches unity. At this point, the simulation underestimates the resistive signal. Furthermore, the electrical response at a given relative wet area is also correlated with the volume of water, as demonstrated by both experimental and simulation data (**Fig. 41d**). This work provides a framework for the quantification of various liquids over large surfaces, which bears important implications for the sustainable and efficient management of fluids.

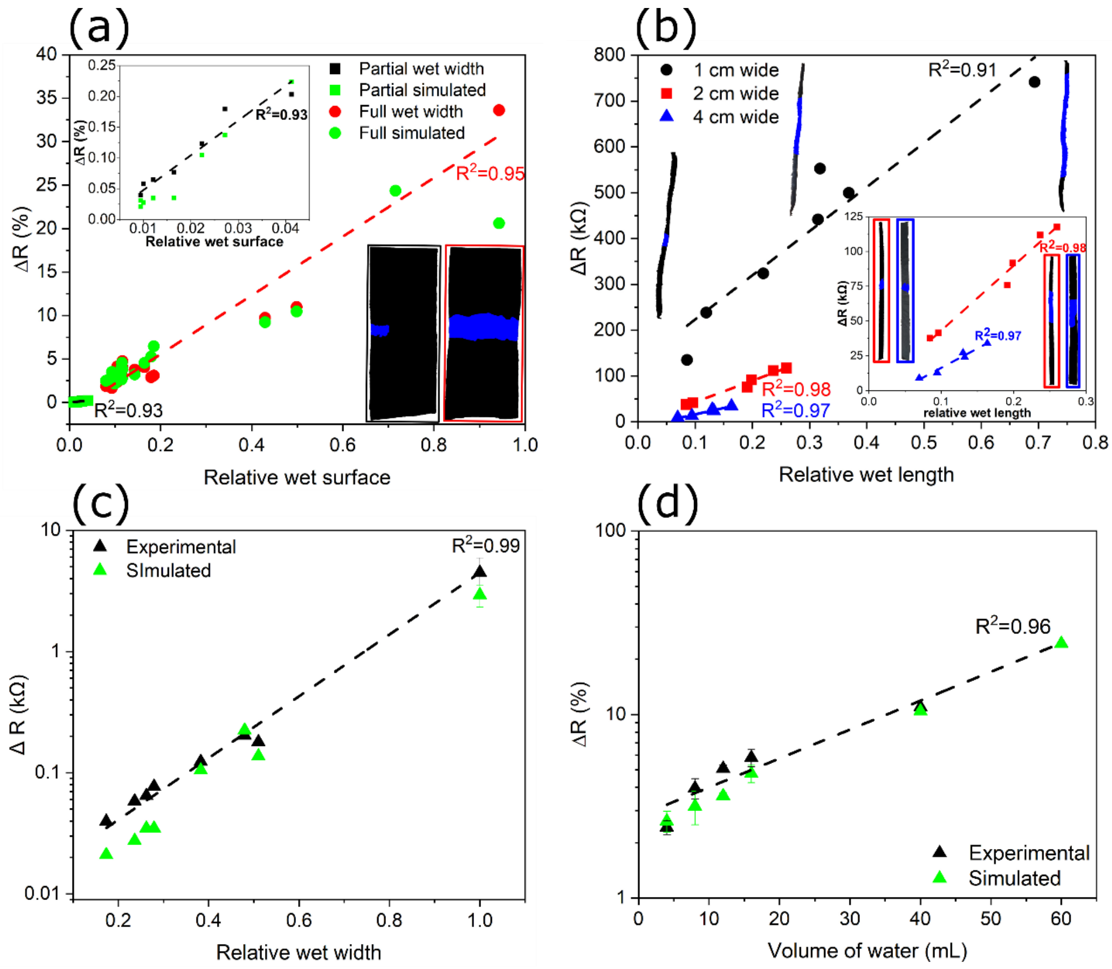

Figure 41. 2D mapping using pilot-scale-produced paper nanocomposites. (a) Change in electrical resistance (*ΔR*) as a function of the relative wet area determined by image analysis. Inset shows expanded view of the partially wet data. (b) Linear evolution of the change in electrical resistance (*ΔR*) as a function of the relative wet length for paper nanocomposites with different dimensions (*i.e.* 1 cm x 80 cm, 2 cm x 80 cm and 4 cm x 80 cm). The insets show images of the wet (blue) and dry (black) portions of the various paper strips, as analyzed by GIMP software. Coolant water was used in this test. (c) Experimental and simulated linear evolution of the change in electrical resistance (*ΔR*) as a function of the relative wet width for 30 cm x 80 cm paper nanocomposite sheets. Coolant water was used in this test. (d) Change in electrical resistance (*ΔR*) as a function of the volume of water applied to the sheet. Simulated data points in (c) and (d) are modeled as described in ESI, where the dry unit resistance (r_d) is calibrated to equate the experimental and simulated dry sheet resistance, depicted in *Equations 7-9*. GIMP software is used to estimate the relative wet area, length, and width.

Finally, there are no statistical differences in resistance when the relative wet area is computed either from multiple discrete small wet spots or from a single wet spot of larger dimensions (**Fig.**

42a). Similarly, no statistical differences are observed between data collected with a single strip of paper sensor and data obtained from a specimen of the same size but comprising multiple strips connected to each other with aluminum tape (**Fig. 42b**). This means that paper nanocomposites can be cut and reattached easily using conductive media without altering sensing performance. Their versatility combined with their innate flexibility makes it possible to design sensory papers with nearly any imaginable shape for various applications in buildings, distribution lines, household manifolds, miniaturized cooling pipes and mobile tanks in ships and trucks.

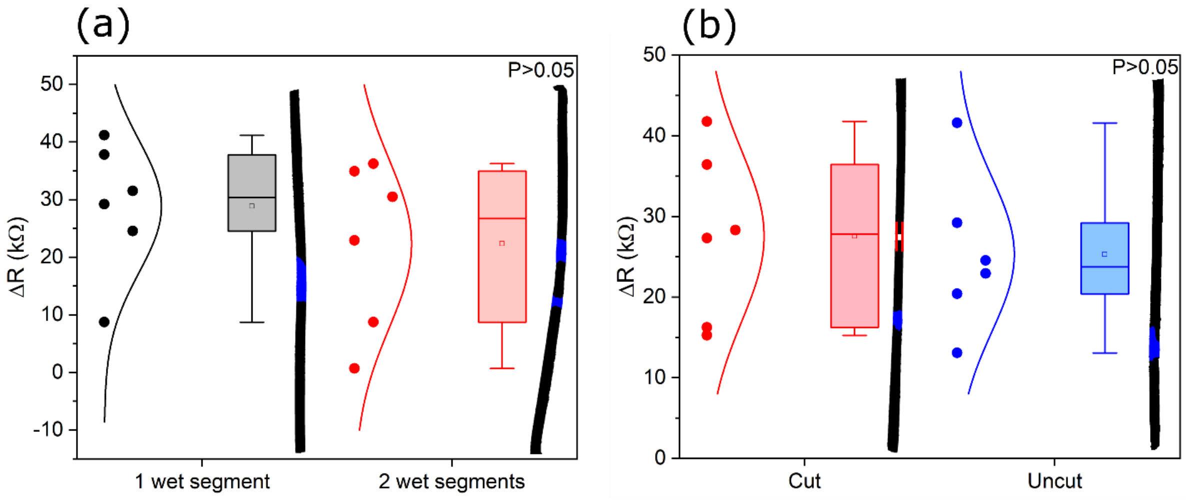

Figure 42. Statistical analysis comparing the means of changes in electrical resistance for 2 cm x 80 cm paper nanocomposite sheets as a function of (a) the number of wet segments and (b) the number of sheets stitched together with aluminum tape. Both studies showed no statistical significance between the means, as indicated by p-values >0.05 at a 95% confidence level.

5.3 Conclusion

In summary, the feasibility of producing conductive paper nanocomposites on a continuous flow filtration system at the pilot-scale demonstrates their commercial viability. The tailored and cost-efficient web forming process is based on mature industrial systems, allowing the transfer of laboratory scale sensors to commercial applications. Sensitivity to liquid water is maintained from the batch to pilot-scale, while the unique binding chemistry achieved through a layer-by-layer-assembly process results in minimal nanoparticle loss with CNT loadings as high as 18 wt%. In collaboration with the ATLAS team at CERN, paper nanocomposites were tested in practical applications at an underground facility to assess their reliability when deployed in non-environmentally-controlled locations and in unique 2D configurations. A preliminary analytical model was developed and used to predict the response to liquid water. When combined with an inexpensive microcontroller, low-cost arrays of highly sensitive and responsive liquid sensing devices can be deployed over large areas, in inaccessible spaces, and challenging configurations to mitigate liquid damage and reduce utility bills by rapidly powering off sensitive instruments and locating leaks.

VI. Chapter 4: Water based fabrication of cellulose nanofibril films as dielectric media

Note: This chapter was based on research funded by the 2019 STEM Chateaubriand Fellowship. Dielectric characterization was collected in collaboration with Centre de Recherche Paul Pascal (CRPP) CNRS, in Bordeaux, France.

Abstract

Cellulose nanofibrils (CNF) have shown considerable promise as a sustainable alternative to traditionally studied petrochemical based polymers as novel dielectrics. While typical polymers are processed into films using harsh chemicals or energy intensive extruding processes (i.e. electrospinning), CNF based films can be processed in water and fabricated using a facile film casting technique. Here, composite TEMPO-oxidized CNF and poly(vinylidene fluoride) (PVDF) films are synthesized and characterized for their resulting dielectric properties and breakdown strength. The effect of oxidation time on CNF dielectric response was studied in detail and demonstrates a twofold enhancement in breakdown strength when the oxidation time was reduced from 3 hours to 5 minutes and used in composite films. When combined with poly vinyl alcohol (PVA) based layers, multi-layered CNF/PVDF composite films are characterized by an increase in dielectric strength while maintaining dielectric losses. Preliminary results demonstrate improved energy storage capabilities with a significant reduction in hysteresis compared to single layer films.

6.1 Introduction

With the ever increasing demand of electrical energy, energy storage technologies are becoming more and more crucial in advanced electrical power systems. Recently, dielectric capacitors have gained significant interest in the literature due to their ability to rapidly release energy, intrinsically high power density and extended life span[26–28]. Dielectric energy storage is defined as the storage of electrical energy due to the polarization of a material in the presence of an external electric field, causing the distribution of positive and negative charges to orient themselves on opposite electrodes. The efficacy of dielectric materials is commonly defined by the energy density of that material, calculated as

$$U_e = \int EdD = \varepsilon_0 \int Ed_{\varepsilon_r}E \qquad \textit{Eqn 1.}$$

where E represents the electric field (breakdown) strength and ε_r denotes the relative permittivity, both of which are key metrics in assessing the applicable range in which dielectric devices can be optimally employed[95]. However, it remains a challenge to develop a material with both a high breakdown strength and a high energy density. When looking for a high energy density material with a high permittivity, a variety of materials are known to be polarizable in the presence of an electric field. The highest response is typically attributed to ceramic materials with a perovskite structure, such as barium titanate ($BaTiO_3$), boron nitride (BN) and zinc oxide (ZnO)[172,173]. However, these materials tend to suffer from limited flexibility and sometimes lower breakdown strengths, hindering their commercial viability.

Compared to the traditionally employed ceramic materials, polymer based dielectrics are being increasingly considered for their superior flexibility and scalability of processing conditions[26,29]. As the most naturally occurring polymeric material on Earth, combined with its biodegradability, flexibility, and innate dielectric properties, cellulose appears to be a sustainable and compelling alternative to commonly studied polymers. Specific interest has been given to the nano-form of cellulose microfibers, such as cellulose nanofibrils (CNF) and cellulose nano crystals (CNC), due to their increased surface area, optical properties, and dispersive qualities[30,32,33,168]. While the dielectric response of CNCs is theoretically higher than that of CNF due to the more ordered crystalline regions contributing to an increased dipole moment, the increased flexibility of CNF from the higher aspect ratio allows for increased versatility in device design. However, recent literature reports of CNF based dielectrics still have not demonstrated achieving commercially competitive dielectric performance while maintaining commercially viable fabrication techniques. Even when implemented as composite structures through the addition of inorganic fillers with known high dielectric constants such as $BaTiO_3$, BN, and ZnO, improvements in dielectric response have come at the cost of reduced breakdown strength[98,104,174]. This is likely due to the challenges associated with the solution processing of organic and inorganic components, leading to non-uniform filler distributions, and contributing to a non-scalable fabrication process, limiting applied use[26,175]. Combining CNF and other polymers to form a polymer-polymer composite, however, allows for improved miscibility and easier processing conditions, capable of large-scale implementation. In this work, a water-based film casting technique is employed to easily fabricate CNF/PVDF composite films for use as flexible, inexpensive, and sustainable dielectrics. The effect of CNF morphology and surface charge on resulting film performance is studied in detail, while preliminary work demonstrates that multi-layered composite film structures with enhanced breakdown strength and energy storage capabilities are possible.

6.2 Results and discussion

6.2.1 Characterization of TEMPO-oxidized cellulose nanofibrils

Cellulose nanofibrils (CNF) were prepared following a TEMPO-mediated oxidation process of bleach Kraft softwood, outlined in subsection 2.2.2 of the Materials and Methods section of this text[50]. Briefly, catalytic amounts of TEMPO, a water soluble and stable nitroxyl radical, and sodium bromide (NaBr) were added to a suspension of bleached Kraft softwood pulp, followed by the addition of sodium hypochlorite (NaClO), which mediates the oxidation of the native cellulose pulp fibers. Resulting fibers underwent mild mechanical defibrillation by blending and probe sonication to achieve nanofibrils[50]. As the oxidation reaction is known to reduce the degree of polymerization of CNF compared to the native cellulose pulp by way of side reactions generating hydroxyl or other radicals that can cut the β-1,4-glycosidic bonds, the effect of oxidation time (3 hours, 1 hour 45 minutes, 30 minutes, and 5 minutes) on resulting fibril morphology was studied in detail using atomic force microscopy (AFM). Diluted dispersions of resulting CNF fabricated at different oxidation times were analyzed, and the resulting fiber height (Gwyddion Software), representative of fiber diameter, and length (ImageJ) were estimated using image analysis software. As can be seen from the distributions shown in **Figure 43**, fiber diameter and length remained relatively constant at 2.1±0.14 nm and 0.71±0.04 μm, respectively, regardless of oxidation time. It is important to note that additional analysis is necessary to confirm oxidation time does not have an effect on fiber morphology or aspect ratio, as fibers oxidized for a shorter time more readily aggregated, making image analysis more challenging.

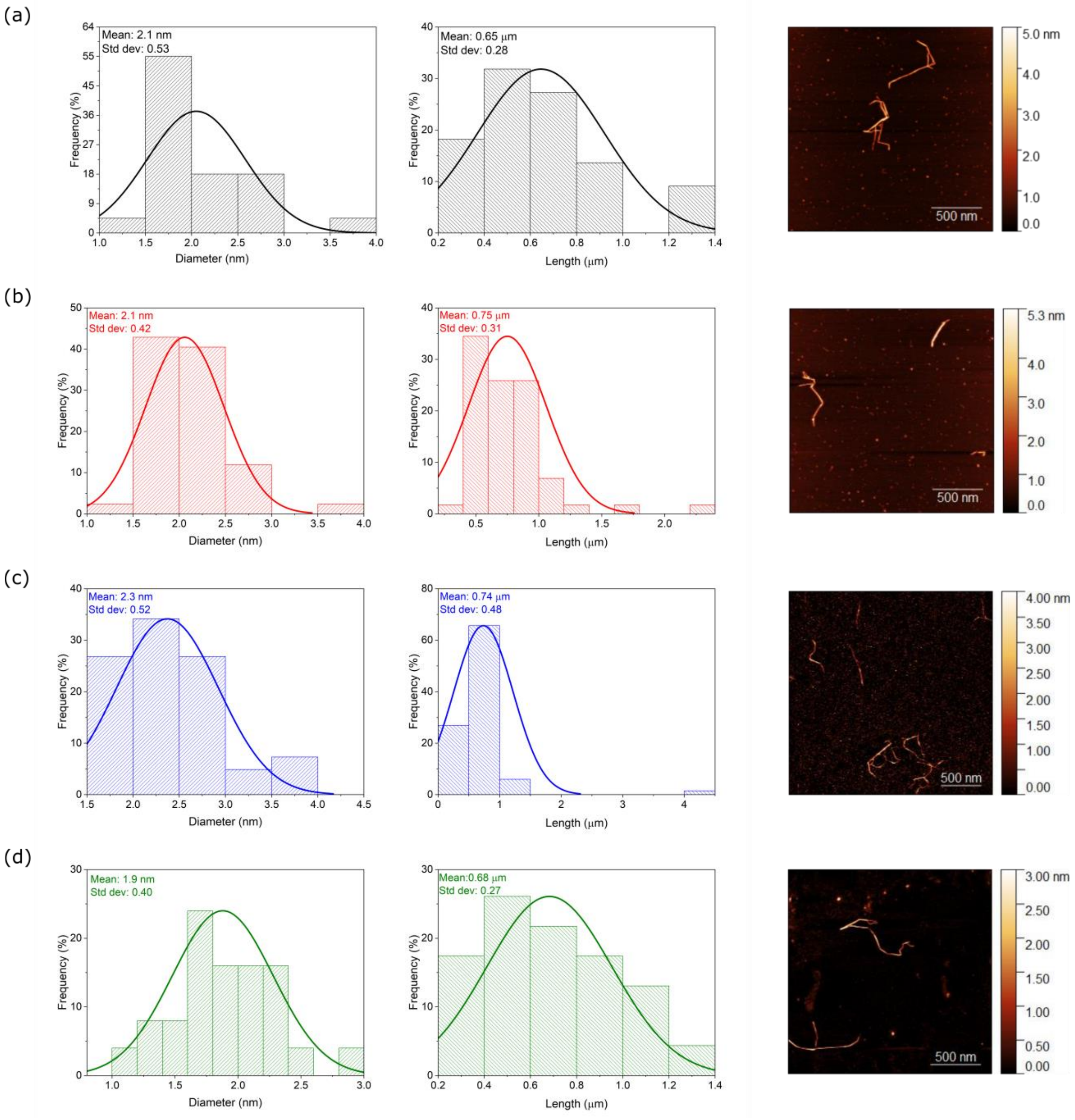

Figure 43. *Fiber morphology analysis as a function of oxidation time*. The effect of oxidation time on fiber diameter and length, as indicated by histograms and representative AFM images are shown for (a) 3 hours, (b) 1 hour and 45 minutes, (c) 30 minutes, and (d) 5 minutes of oxidation.

As TEMPO-oxidation is known to generate nanofibers with a large content of anionically charged carboxylate groups on the surface at high densities[50,60], which may affect resulting dielectric properties of interest, the effect of oxidation time on charge density was studied using conductometric titration, described in detail in subsection 2.3.1a of the Materials and Methods section of this text. Results indicate that as oxidation time increases, the charge density of the fibrils also increases, up to a maximum of approximately 0.75±0.06 mmol COOH/g CNF after 3 hours of oxidation (**Figure 44**). Interestingly, the majority of carboxylate groups were produced in the first 30 minutes of the oxidation reaction, and production leveled off soon thereafter, which is consistent with other reports in the literature[59]. The effect of oxidation time on charge density can be approximated by a Langmuir adsorption isotherm ($R^2=0.99$). While the oxidation reaction is not a true adsorption system of COOH groups onto the fibril surface, and is rather the result of a reaction, the isotherm assumes an operational monolayer, which is still representative of the regioselective conversion of C6 hydroxyls to carboxylates on the fibril surface[50]. The Langmuir isotherm can therefore be used as an initial prediction of the charge density for a given oxidation time. **Figure 44** shows the effect of oxidation time on charge density and fiber morphology.

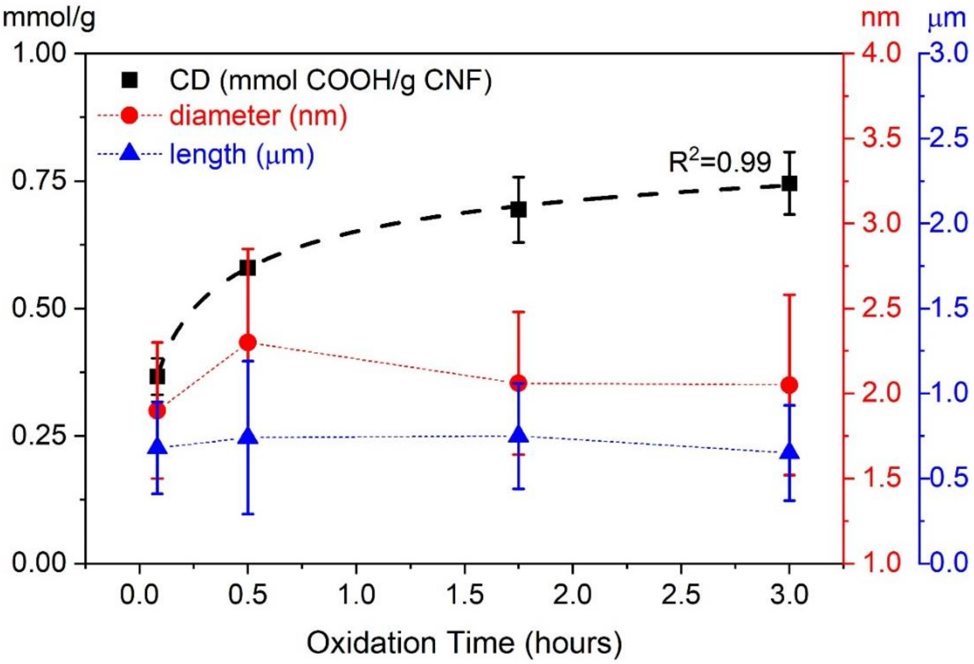

Figure 44. *Effect of oxidation time of fiber morphology* (diameter, nm and length, μm) and surface charge (charge density, mmol COOH/g CNF).

Interestingly, as the charge density of the CNF increases, so did the apparent transparency of the CNF solutions. Although it was confirmed that the majority of carboxylate groups were produced within the first 30 minutes of the oxidation reaction, the longer oxidation times resulted in an increase in solution transparency, quantified by optical absorption (UV-vis) spectroscopy, shown in **Figure 45**. Light transmittance is related to particle size, or fibril width in the case of this study, as larger particles more effectively scatter light, reducing the amount of transmitted light[176,177]. Since the nanofibers produced from all oxidation times studied resulted in approximately the same fiber diameter of 2.1+0.14 nm, the difference in solution transparency and light transmittance can be understood by the degree of agglomeration with the different dispersions. Nanofibrils smaller than the wavelength of visible light are known to cause the dispersion to appear transparent, as should be the case with fibrils produced across all oxidation times. However, at the lower charge densities, fibrils have fewer annionically charged carboxylate groups on their surface, resulting in less electrostatic repulsion between fibers in solution, allowing for increased agglomeration. This in turn increases the absorption of light, thus reducing the amount of light transmitted[3,50,178].

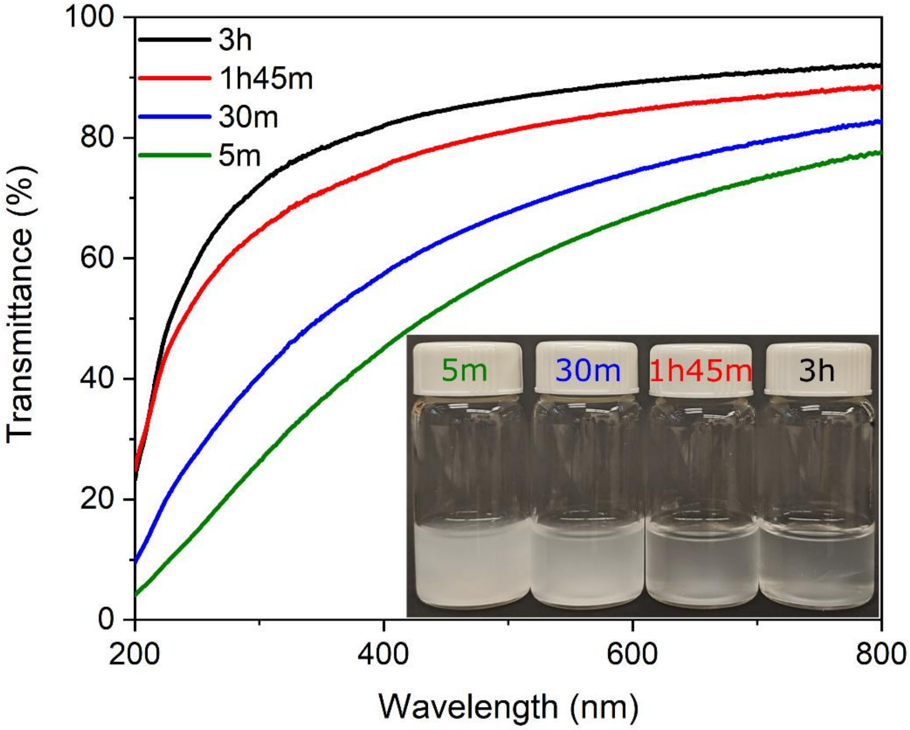

Figure 45. *Optical absorption (UV-vis) spectroscopy of as-prepared CNF*. (a) UV-vis spectroscopy of CNF dispersions produced at different oxidation times. Inset shows an image of CNF dispersions produced at different oxidation times. (b) UV-vis spectroscopy of films prepared from CNF fabricated at different oxidation times. Inset shows transparency of CNF film prepared from 5 minute oxidized CNF.

Although all charge densities measures, regardless of oxidation time, resulted in relatively transparent solutions with no visible agglomerations, solution charge density should be taken into consideration when utilizing CNF as a dispersant for composited formulation. The increased agglomeration of fibrils present in solution at lower charge densities is also known to increase solution viscosity[59]. This increased viscosity, along with the reduced electrostatic repulsion between fibrils achieved, may lead to a reduction in dispersion quality, particularly when additional particles or constituents are added to the CNF solution. This becomes of paramount importance when additional polymers are combined with CNF to develop composite formulations with enhanced dielectric properties and energy storage capabilities.

6.2.2 Characterization of pristine CNF and composite CNF/PVDF films

Pristine (CNF) and composite (CNF/PVDF) films were prepared following a water-based solution casting process, described in detail in subsection 2.2.7 of the Materials and Methods section of this text. Briefly, either pure CNF or a CNF/PVDF aqueous solution was mechanically stirred followed by bath sonication, before being oven dried at 50 °C. A reduced visual representation of the film casting process is depicted in **Figure 46**. Films were prepared using CNF treated at all four oxidation times studied (3 hours, 1 hour 45 minutes, 30 minutes, and 5 minutes), with a PVDF nanoparticle loading of 10 wt% used in all composite films. All films, both pristine and composite, were prepared based on the same final film weight of 0.25 g of solids, resulting in an average films thickness of 29.6±2.7 µm.

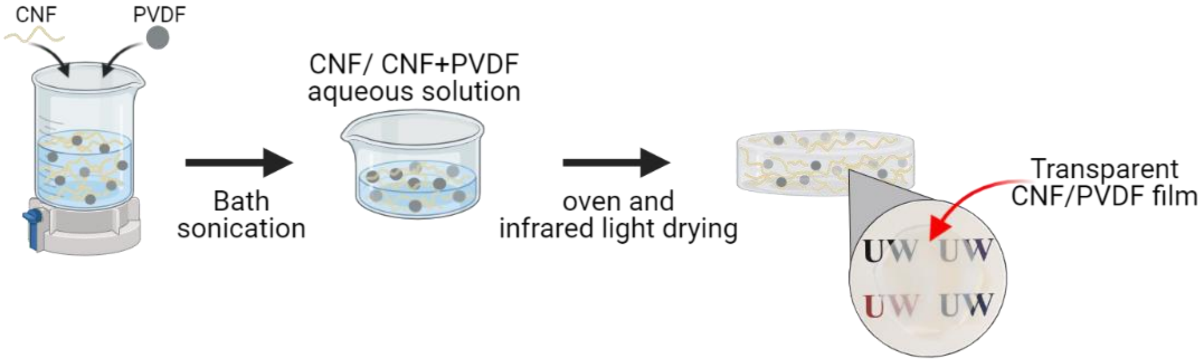

Figure 46. *Representative water-based fabrication technique* for both pristine CNF and composite CNF/PVDF transparent films. Image created with BioRender.

While both pristine and composite films formed easily following the film casting process and appeared visibly uniform regardless of PVDF nanoparticle addition, film microstructure was examined in greater detail to better assess the formation uniformity. UV-vis spectroscopy was used to examine film uniformity by way of assessing the transparency across all films (Ø~7 cm), indicated by the transmittance of light. **Figure 47a** shows representative UV-vis spectra of a pure film prepared from CNF oxidized for 3 hours and indicates the film has the same transparency across all five positions measured, suggesting uniform formation and individualization of fibrils. When comparing the transmittance of pure and composite films, it is clear that the addition of 10 wt% of PVDF decreases the film transparency compared to pristine films, regardless of oxidation time (**Figure 47b**). Interestingly, while there is minimal loss in transmittance for pristine films as oxidation time decreases, the oxidation time has a much greater impact on the transparency when PVDF nanoparticles are present. As shorter oxidation times were confirmed to decrease the charge density of CNF, this suggests that lower charge densities are unable to disperse PVDF nanoparticles as effectively, resulting in increased agglomerates in film formation. Regardless of the increased potential for agglomerates, films appeared visibly uniform and relatively transparent regardless of charge density or PVDF content as shown in the images in **Figure 47c-d**. Transmittance results suggest films may be implemented in wearable electronic devices where optical properties remain of great importance.

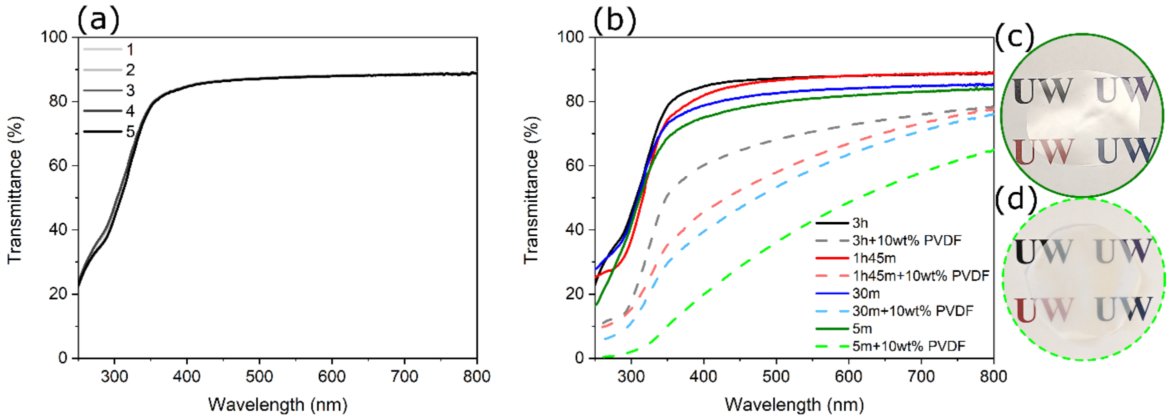

Figure 47. *Optical absorption (UV-vis) spectroscopy of pristine and composite CNF films*. (a) Uv-vis spectroscopy of pristine CNF film prepared from 5m oxidized CNF measured at five locations across the film. (b) UV-vis spectroscopy comparing pristine and composite films prepared from CNF oxidized for different lengths of time (3 hours, 1 hour 45 minutes, 30 minutes, and 5 minutes). Photos comparing transparency of (c) pristine CNF and (d) composite CNF/PVDF films.

Although composite films visually appeared to be macroscopically uniform, the microstructure of composite CNF/PVDF films still remained of great interest, as the effect of the PVDF nanoparticles as a filler material to enhance dielectric performance could be hindered by non-uniform distribution and agglomeration. Scanning electron microscopy (SEM) was used to examine the cryo-fractured cross section of composite CNF/PVDF films. **Figure 48** demonstrates that even at a high PVDF loading of 10 wt%, and when CNF oxidized for only 5 minutes were used in a film, PVDF nanoparticles are well dispersed throughout the cellulose matrix. The high magnification image shown in **Figure 48b** demonstrates that the PVDF nanoparticles are not only well dispersed, but that there is also minimal agglomeration within the composite.

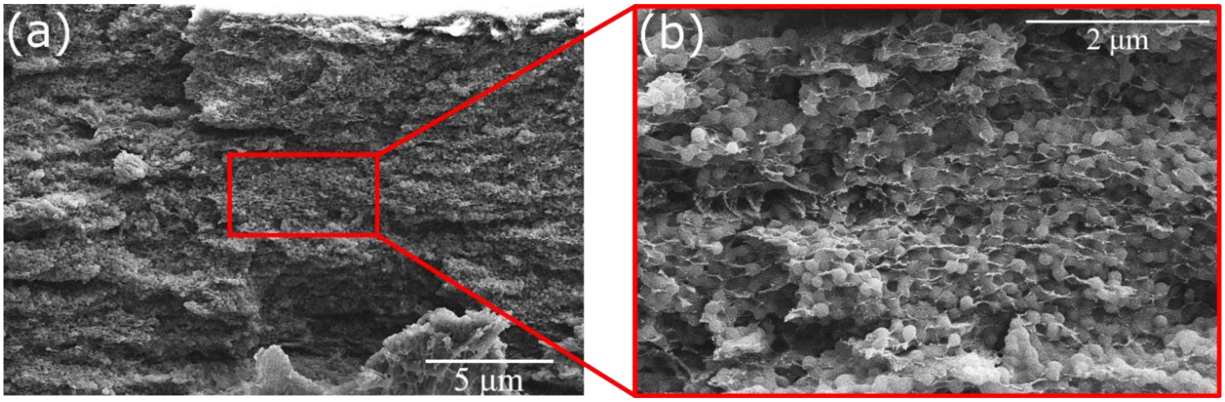

Figure 48. *SEM of 5m+10wt%PVDF composite film.* (a) Low magnification SEM of CNF/PVDF composite film. (b) High magnification of same CNF/PVDF composite film.

In composite films, PVDF was added to study the effect that a known polarizable structure had on film performance as an energy storage and generation material. Originating from the polymer chains crystal structure, PVDF exists in four possible configurations depending on how the dipoles are aligned: β, α, γ, and δ[179]. Although the α configuration is the most common, the β phase remains the most desired, as it produces the highest dipole moment due to an all-trans planar zig-zag conformation, where all fluorine atoms are located on one side of the polymer chain[108,180,181]. As the PVDF used in this study was received from Arkema as a proprietary dispersion of PVDF in a mix of surfactants, the conformation of the PVDF was unknown. Composite films prepared with the as-received PVDF were analyzed by X-ray diffraction (XRD) and Fourier transform infrared spectroscopy (FTIR) to assess the potential configuration of PVDF received and to gain additional insight into the formation of CNF/PVDF composite films. As shown in **Figure 49a**, the XRD spectra indicates the PVDF nanoparticles are mainly composited of a combination of the α- and β-phase configurations, as evident by the diffraction peaks at 18.4° and 41.1°, and 20.6°, respectively[181]. The corresponding FITR spectra (grey) is in agreement with XRD results, indicating the presence of both α- and β-phase configurations (**Figure 49b**). When analyzing FTIR of PVDF, the literature presents many conflicting analyses. A majority of peaks that occur are common to all chain conformations, resulting in inconclusive assessments of the polymer chain configuration present[181]. In the interest of gaining preliminary knowledge of the chain conformation present, only peaks exclusive to one or two conformations were considered in these approximations. One of the most commonly understood bands to indicate α-phase conformation is indicated by the 763 cm^{-1} peak which, although shifted here due to the presence of surfactants, is still present[180–182]. The small bands at 840 cm^{-1} and 1275 cm^{-1} indicate the presence of the β-phase, while the band at 1180 cm^{-1} could indicate the presence of either the β- or γ-phase, both of which possess electro-active properties[180,181]. When analyzing the FTIR spectra of the composite film compared to that of the pure CNF film and the PVDF sample, a shift in the main peak in the fingerprint region (>1500 cm^{-1}) is clearly visible. The band ranging from 3600 to 3100 cm^{-1} is well accepted to be indicative of hydroxyl moieties in cellulose components, and sensitive to hydrogen bonding between cellulose fibrils[19,126]. As this band is not present in the PVDF film, the shift to higher wavenumbers observed in this region in the composite sample can be attributed to the introduction of PVDF nanoparticles within the composite, disrupting the inter-fibril hydrogen bonding within the nanocellulose matrix and indicating potential binding between the CNF fibrils and PVDF nanoparticles. Preliminary results from XRD and FITR suggest that, depending on resulting dielectric performance, additional treatments such as heating/hot pressing[183], high voltage exposure[97,99], and applied mechanical strain[182] may be used to enhance film properties by favoring the β-phase conformations of PVDF.

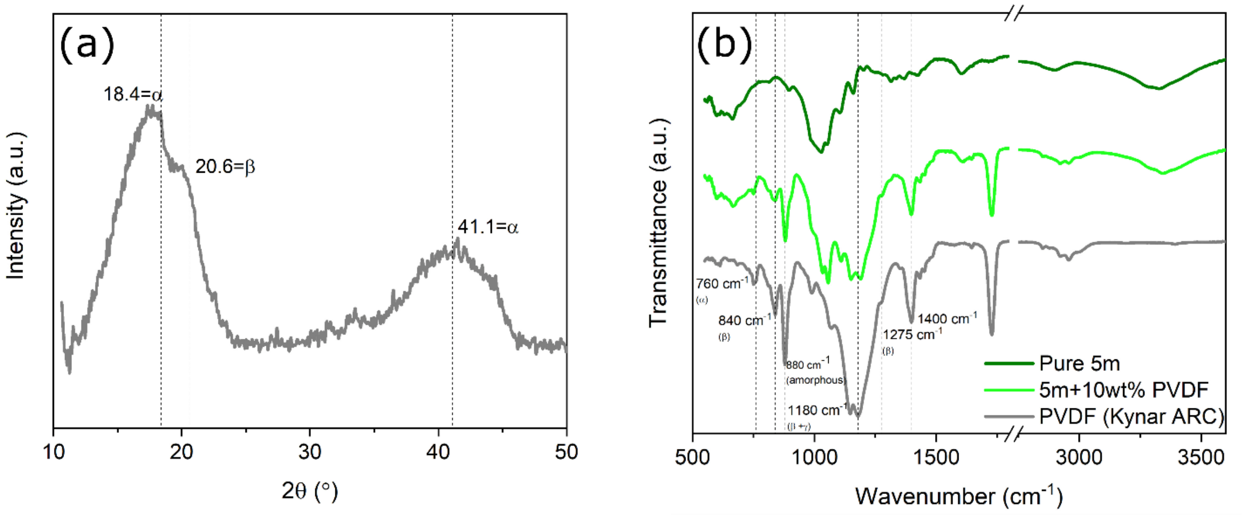

Figure 49. *Analysis of PVDF nanoparticle chain conformations*. (a) XRD pattern for PVDF nanoparticles provided by Arkema. (b) FTIR spectra of PVDF, pristine 5 minute oxidized CNF, and composite 5m+10 wt% PVDF films.

6.2.3 Dielectric performance of pristine CNF and composite CNF/PVDF films

The effects of varied CNF oxidation time and the addition of PVDF nanoparticles on the frequency-dependent dielectric properties, measured by electrochemical impedance spectroscopy (EIS), were studied in detail, and are presented in **Figure 50**. In EIS experiments, an AC sinusoidal voltage is applied through a material across a range of frequencies, and the resulting sinusoidal current is measured. The relative permittivity, AC conductivity, and loss tangent of a material can then be extracted from the measured data. The relative permittivity, also referred to as the dielectric constant, is defined as the ratio of the permittivity of a material to the permittivity of free space, and effectively describes the ability of a material to store charge for a given applied electric field[184]. The AC conductivity represents the frequency-dependent electrical conductivity of the material, and the loss tangent represents the dissipation of electrical energy that is not able to be stored within the material[185].

The relative permittivity of all films, regardless of oxidation time, tends to decrease with increasing frequency, as shown in **Figure 50a**. This response is consistent with other cellulose and PVDF based dielectric materials, and may be due to the relaxation phenomenon that occurs at high frequencies, or the momentary delay in dipole polarization, contributing to an increase in dielectric loss[33,99,184,186]. At each frequency, the dielectric constant decreases with decreasing oxidation time for pure CNF films, which can be attributed to the reduced number of anionically charged polarizable functional groups able to contribute to the net dipole of the material[187,188]. Regardless of oxidation time, the dielectric constant of pure CNF films at lower frequencies (i.e. 10^1) are some of the highest reported to date for cellulose based films[33,98,107]. When PVDF nanoparticles are added to the CNF matrix, a decrease in the dielectric constant is observed across all oxidation times. Although PVDF is typically understood to possess a high dielectric constant at certain chain configurations, the addition of nanoparticles into a polymeric matrix can cause significant changes in the resulting composites dielectric response, due to the formation of interaction zones[184]. As particle size of the filler material is reduced, the proportion of the composite that is the interface zone starts to become significant. At high frequencies, the CNF/PVDF composite films have lower dielectric constants that their pure CNF counterparts, regardless of oxidation time. This may be attributed to the nanoparticles restricting the end or side-chain dipole movements of the polymer matrix, as demonstrated by Nelson and Fothergill[189]. The significant reduction in dielectric constant of the nanocomposites compared to the pristine CNF films, is what Jonscher referred to as “low-frequency dispersion”, characteristic of charge carriers having limited freedom of movement within a composite[184,190]. This phenomenon may indicate that even at a higher loading of 10 wt% of PVDF nanoparticles, at such a low volume fraction (i.e. ~0.2 vol%), inadequate dispersion may have led to a non-uniform distribution of interaction zones throughout the composite. In regions where there is a sub-percolation level interaction zones, a mitigation of space charge accumulation may occur, resulting in a reduced dielectric constant[184].

The effect of oxidation time on AC conductivity indicates the same trend as permittivity, where a lower oxidation time leads to a reduction in the film conductivity, as shown in **Figure 50b**. This is likely due to the reduced number of charge transport routes throughout the CNF matrix as lower oxidation times generate fibers with lower charge densities. The addition of PVDF nanoparticles to form composite CNF/PVDF films reduces conductivity, likely due to the PVDF nanoparticles disrupting inter-fiber bonding within the CNF matrix, and further disrupting charge transport routes throughout the film[108]. While reducing oxidation time did decrease the AC conductivity of the pristine films, these films still remain too conductive for effective energy storage applications as they become semi-conducting at higher frequencies. However, at the lowest oxidation time (5 minutes), with the incorporation of 10 wt% PVDF nanoparticles, CNF/PVDF composite films remain below 10^{-6} S/m across all frequencies. Regardless of oxidation time or the presence of PVDF nanoparticles, AC conductivity increases with increasing frequency, likely due to the space charge effect, where the internal charges are forced to try and align faster than they are able to, creating a non-uniform charge displacement within the film. These disturbed charge arrangements can lead to localized changes in the internal electric field strength, resulting in localized areas within the films that appear more conductive[191].

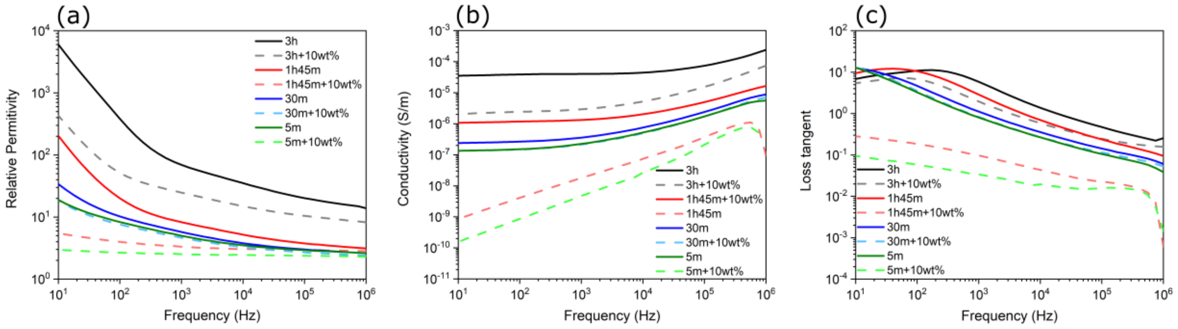

Figure 50. *Frequency dependent dielectric properties for pristine and composite CNF films*. (a) Relative permittivity, (b) AC conductivity, and (c) Loss tangent.

Although reducing the oxidation time also reduced the conductivity of pristine CNF films, raising the viability for energy storage applications, the losses remained high for films prepared from CNF at all oxidation times studied (**Figure 50c**). The incorporation of PVDF had the greatest reduction in losses for the lowest oxidation time studied, demonstrating significant improvement in composite film energy storage capabilities. Interestingly, composite films prepared from CNF which were oxidized for 1 hour and 45 minutes had the second largest reduction in losses. Combined with only slightly increased conductivity and a higher dielectric constant, this composite film formulation showed promise for energy storage applications as well.

In addition to the effect of oxidation time and PVDF on the dielectric properties of CNF-based films, the breakdown strength (E_b), was measured for all pristine CNF and composite CNF/PVDF films. The breakdown strength is defined as the maximum voltage required to cause dielectric breakdown, or the voltage at which the material in question is no longer insulating and allows current to flow through it[184]. The characteristic E_b values of all pristine and composite films were analyzed by the two-parameter Weibull statistical distribution, described as

$$P(E_b) = 1 - \exp(-({}^{E_0}/_{E_b})^{\beta}) \qquad \textit{Eqn. 6}$$

where $P(E_b)$ is the cumulative probability of electric failure, E_0 is the experimental breakdown strength, E_b is a scale parameter representative of the characteristic E_b when the cumulative failure probability is 63.2%, and β is a shape parameter to analyze the scatter state of the data and indicate the reliability and uniformity of the film[99,115,116]. **Figure 51** shows the Weibull distribution (linear fit) for representative E_b values (scatter plot) for all pristine and composite films. In general, the breakdown strength increased with a reduction in oxidation time, with the highest pristine film breakdown strength of 108 MV/m achieved for a pristine 5 minute oxidized CNF film. As was seen for the frequency dependent properties, this is likely due to the fact that with fewer anionically charged functional groups present on the CNF surface, there is a reduced charge transport route throughout films prepared from CNF at shorter oxidation times. However, it is important to note that although a higher breakdown strength was achieved for a film prepared at 5 minutes, as can be seen from the distribution of the measured E_b values, the spread of the data is much greater than for other pure CNF films. This is related to the shape parameter (β), indicative of the structural uniformity of the film. The low β-value of 5.2 suggests the film formation from the 5 minute oxidized CNF fibers is not as uniform as expected, and could potentially benefit from additional mixing and sonication during the film preparation process compared to when fibrils with a higher surface charge are used.

With the addition of PDVF, composite films showed an improved breakdown strength across all oxidation times studied, with the greatest improvement seen for the films prepared from CNF oxidized for shorter amounts of time (i.e. 30 minutes and 5 minutes). Composite films prepared from CNF oxidized for only 5 minutes resulted in the highest breakdown strength of 157 MV/m. Although EIS data indicated a similar dielectric constant, conductivity, and loss tangent for composite films prepared from 1 hour 45 minute and 5 minute oxidation times, the superior breakdown strength achieved for the 5 minute oxidized composite film demonstrates superior dielectric properties and the possibility of greater energy storage.

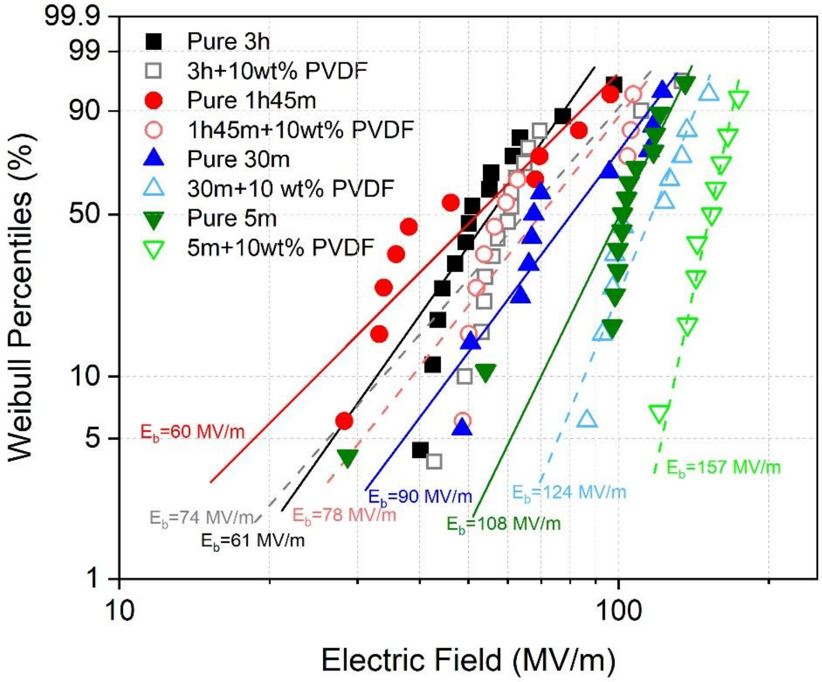

Figure 51. *Failure probability of dielectric breakdown* determined from the Weibull distribution for pristine CNF and composite CNF/PVDF films.

While the addition of PVDF seemingly enhances the breakdown strength of the studied CNF films, even a small addition of nanoparticle fillers is known to form large-area interfaces within the bulk matrix, which can cause the breakdown strength of composites to differ vastly compared to their pristine polymer counterparts[96,184,192] Nanoparticles have been proven to suppress space charge at increasing applied electric fields, limiting the probability of electrical breakdown by trapping charge within the interface regions[193,194]. At lower charge densities, nanoparticle distribution is assumed to be less uniform within the composite films, resulting in high and low nanoparticle density areas. In the low density areas, less charge may be able to be trapped by the interface regions, leading to localized areas of breakdown, reducing the overall breakdown strength of the film.

Notably, the breakdown of a pure PVDF film (15-25 μm), prepared from aqueous PVDF received from Arkema, was measured at 222.6 MV/m by Che et al[26], which is lower than typically reported breakdown strengths of PVDF films prepared from traditional solution casting or melt-extruding processes (~350-400 MV/m)[195,196]. The discrepancies of results reported in the literature are most likely from the film processing techniques. Solution casting the aqueous colloidal PVDF provided by Arkema led to significant cracking in the dried film due to capillary pressure created between tightly packed PVDF nanoparticles, brought closer together as the water evaporated throughout the drying process[26]. Without additional additives, such as PVA, to assist in film formation, it is extremely difficult to achieve large-area pristine PVDF films for accurate breakdown measurements.

Polarization-electric field (P-E) loops were measured to assess the linearity and hysteresis of both pristine and composite films. By incrementally applying increasing electric fields that approach breakdown, inherent properties about the materials dielectric strength and ability to store charge, including device efficiency, charge energy density, and discharge energy density can be determined. The shape of the resulting P-E loops is also a clear indicator of the material properties and can help to explain the results from EIS and breakdown strength measurements. If the material displayed ideal linear capacitor behavior, the P-E loop would present as a straight line where the applied electric field is proportional to the capacitance, and the charge and discharge energy are the same at all applied electric fields, as shown in **Figure 52a**[197]. When the material behaves as an ideal resistor, the P-E loop presents as an oval, demonstrating the material is never storing any charge, and is simply allowing current to flow through it (**Figure 52b**)[197]. If the properties of these two responses are combined, a lossy capacitor is achieved, where the area of the P-E loop is directly proportional to the device's loss tangent, as measured from EIS, and the slope is proportional to the capacitance. This presents itself as a tilted oval through the origin, as shown in **Figure 52c**[197].

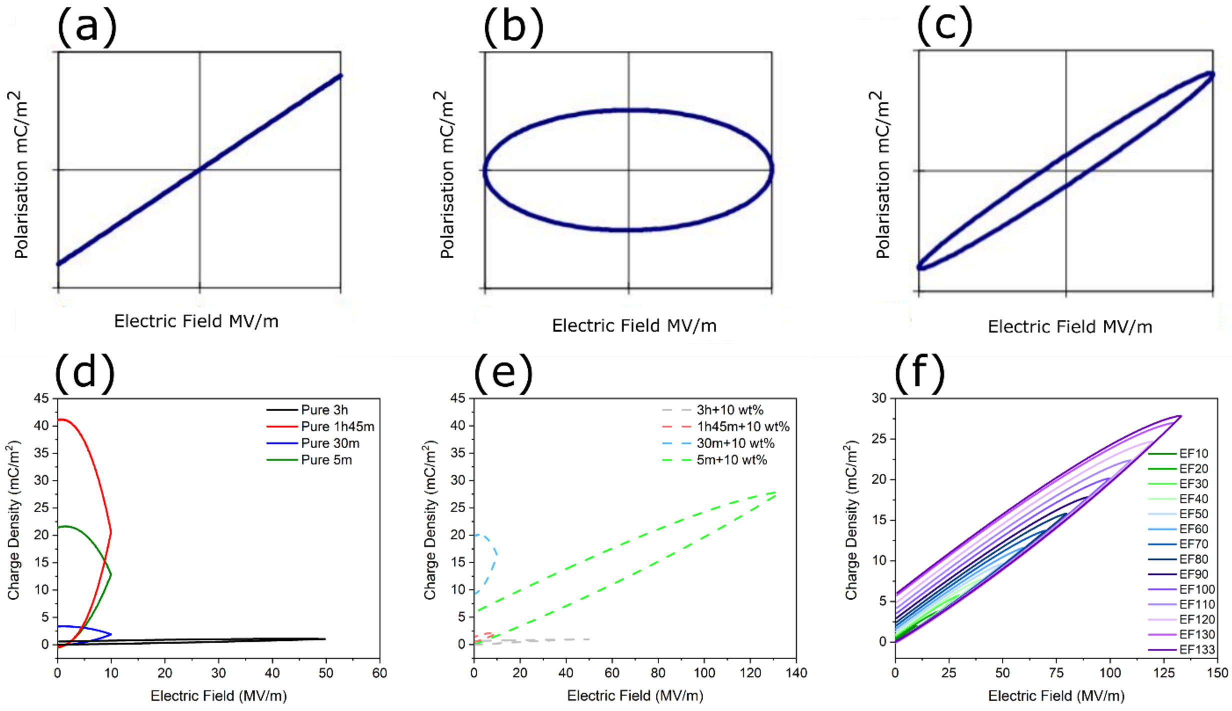

Figure 52. *Polarization electric-field (P-E) loops* of (a) an ideal capacitor[197], (b) an ideal resistor[197], and (d) a lossy capacitor[197]. P-E loops comparing the maximum electric field applied before breakdown was reached for (d) pristine CNF films and (e) composite CNF/PVDF films prepared from CNF oxidized for different lengths of time. (f) P-E loop of composite 5m+10 wt% PVDF film.

As can be seen from **Figure 52d**, when comparing the results from the highest sub-breakdown applied electric fields for pristine CNF films, the shape of the P-E loops most closely resembles that of an ideal resistor, regardless of oxidation time studied. For the case of the films prepared from the longest oxidation time CNF (i.e. highest charge density), even at higher applied electric fields, almost no charge is able to be stored, as indicated by the nearly horizontal black line on the graph. Even at the shorter oxidation times, pristine films behave more like resistors rather than capacitors, indicating they are unable to store significant charge, even at low electric fields, due to the bulk conductivity of the CNF matrix. When comparing the highest sub-breakdown P-E loops for composite CNF/PVDF films, only the film prepared from the shortest oxidation time CNF (5 minutes) behaves as a lossy capacitor, reversibly storing charge. As can be seen from **Figure 52e**, the 5m+10 wt% PVDF composite film demonstrates an increase in charge density for an increase in applied electric field, indicating the material is able to store charge, rather than solely letting current flow through it. However, the shape of the curve at the highest electric field applied still indicates some hysteresis, confirming the losses in the material as seen with EIS. When examining the full range of P-E loops studied for the 5m+10wt% PVDF composite film (**Figure 52f**), electric fields from 10 MV/m to 133 MV/m were applied. As the electric field increased, the hysteresis observed also increased, to a point that beyond 133 MV/m the material could not continue to store charge and reached breakdown, likely due to the bulk conduction in the CNF matrix[26].

Given that only the composite film prepared from the shortest oxidation time CNF (5m +10wt% PVDF) demonstrated the ability to store charge, it was the only film where the discharge energy density and efficiency of the device could be calculated (**Figure 53**). The discharge energy density is calculated at each applied electric field until the film reaches breakdown and indicates a maximum energy density (U_e) of ~1.3 J/cm3 at the highest electric field (133 MV/m). For practical applications, however, it is important to also evaluate the charge/discharge efficiency to better understand device performance. The charge/discharge efficiency, η, is defined as

$$\eta = \frac{U_e}{U_s} = 1 - \frac{U_l}{U_s} * 100\% \qquad \textit{Eqn 10.}$$

Where U_s, U_e, and U_l represent the stored energy, discharge energy, and energy loss, respectively[26]. The energy loss is calculated by the numerical integration of the area under the P-E loops caused by the hysteresis of the material.

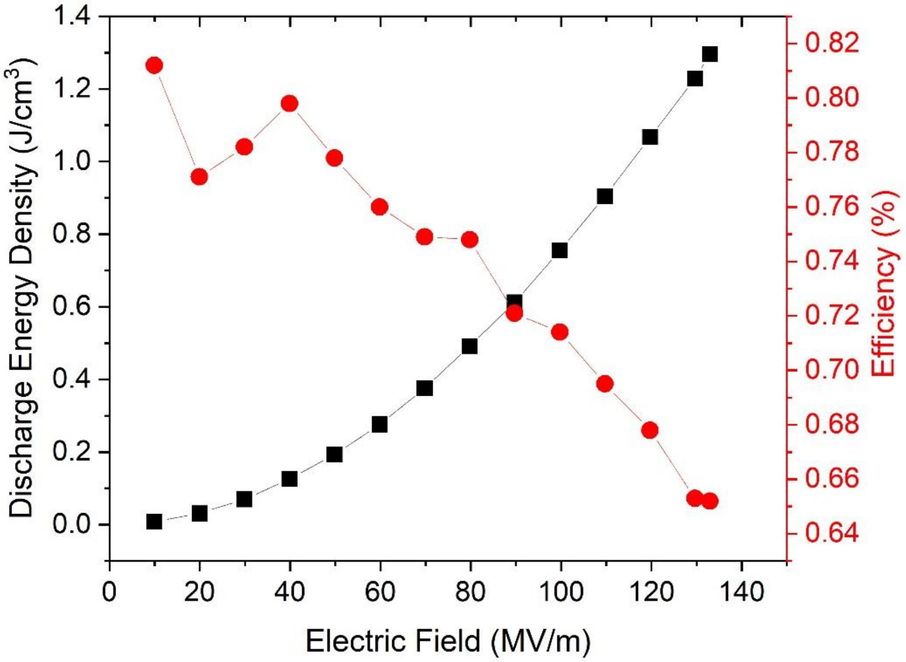

Figure 53. Discharge energy density and efficiency curves of 5m+10 wt% PVDF composite film.

As can be seen from **Figure 53**, as the applied electric field is increased, the device efficiency decreases. This can be attributed to the heightened conduction losses, which are more prevalent at higher electric fields. Operational device conditions should consider both the discharge energy density and efficiency to determine the most optimal performance of the dielectric material, as the highest discharge energy density occurs when the device is the least efficient. Although the discharge energy density remains much lower than what can be achieved for traditional PVDF based films, overall film performance remains comparable given the relatively low electric fields applied (<200 MV/m)[26,99,198]. The low breakdown strength of the composite film severely hinders the ability to apply higher electric fields, reducing the potential for increased charge storage. Results from the 5m+10 wt% PVDF composite film suggest that while CNF offers a robust matrix for dielectric film formation, low breakdown strength from inherent conduction in the bulk CNF matrix is the limiting factor in the use of CNF composite films for energy storage applications, resulting in increased losses during charge storage experiments.

6.2.4 Dielectric performance of bilayer and sandwich structured films

6.2.4a. Fabrication and characterization of bilayer and sandwich structure films

In an effort to improve breakdown strength and reduce losses of 5m+10 wt% PVDF composite films, bilayer and sandwich structure films were evaluated as a way to create more insulating barriers within the composite films and reduce the effect of the innate semi-conducting properties of the CNF matrix. By encasing the best performing CNF/PVDF composite film (i.e. 5m+10 wt% PVDF) with insulating PVA layers, the overall bulk conductance can be reduced. By incorporating 3 wt% PVDF nanoparticles to augment permittivity of the insulating PVA layer, additional dielectric performance can potentially be demonstrated. Following the procedure outlined in detail in subsection 2.2.7d-e of the Materials and Methods section of this text, bilayer and sandwich structure films were prepared from alternating layers of a 5m+10wt% PVDF (CNF/PVDF) and either pure PVA or a composite PVA/PVDF layer. Briefly, bilayer films were prepared by first drying a well-mixed CNF+10wt% PVDF solution in a crystalizing dish in the oven at 50 °C for 32 hours. Following removal from the oven, a well-mixed PVA (1.1 wt% aq) or PVA/PVDF (1.1 wt% aq, 3 wt% PVDF) solution was gently poured on top, taking care to not disturb the surface of the CNF layer. Films were then placed in the oven again at 50 °C until fully dried. An infrared heat lamp was also used for additional drying when necessary. Sandwich structure films were prepared by first completely drying a base PVA or PVA/PVDF layer with an IR heat lamp, followed by gently pouring a well-mixed CNF+10 wt% PVDF solution on top and oven drying at 50 °C for 32 hours. The semi-dried film structure was then removed from the oven and a well-mixed PVA (1.1 wt% aq) or PVA/PVDF (1.1 wt% aq, 3 wt% PVDF) solution was gently poured on top, taking care to not disturb the surface of the CNF layer. Sandwich films were then oven dried at 50 °C. The procedure outlined by Che et al was used as a baseline for preparing the PVA and PVA/PVDF film layers as solution processing, PVDF loading, and drying techniques were studied in detail to achieve the highest breakdown strength[26]. A simplified representation of resulting formation of bilayer and sandwich structured films is outlined in **Figure 54**.

Figure 54. *Schematic representing resulting structure of bilayer and sandwich structure films* prepared by a film casting process, outlined in detail in the Materials and Methods section of this text.

The cross-section of both bilayer and sandwich structure films was examined with SEM to assess the formation of the layered structured. Films were first cryo-fractured in liquid nitrogen to achieve a clean break, which allowed for imaging of the film cross section. As can be seen from the SEM image in **Figure 55a**, the CNF layer in the bilayer films is slightly more than double the thickness of the top PVA based layer with an average thickness of 31.9±1.3 µm and 15.4±0.8 µm, respectively. When comparing to the sandwich structured film in **Figure 55b**, it is clear that the base PVA layer (6.5±0.6 µm) is much thinner than the top PVA layer (16.5+1.8 µm), even though the same amount of solution was used for each layer. As the top layer for the bilayer films shared a similar thickness, it suggests that the 32 hour dry used to prepare the semi-dry CNF layer may not have been long enough to prevent leaching of the top PVA layer into the CNF layer. Since the base PVA layer was completely dried prior to adding the CNF layer on top, a distinct layer was able to form with minimal leaching of the CNF solution into the base layer. Regardless of the interaction between layers at the interface regions, no delamination was observed and films remained robust even after repeated bending (**Figure 55a inset**).

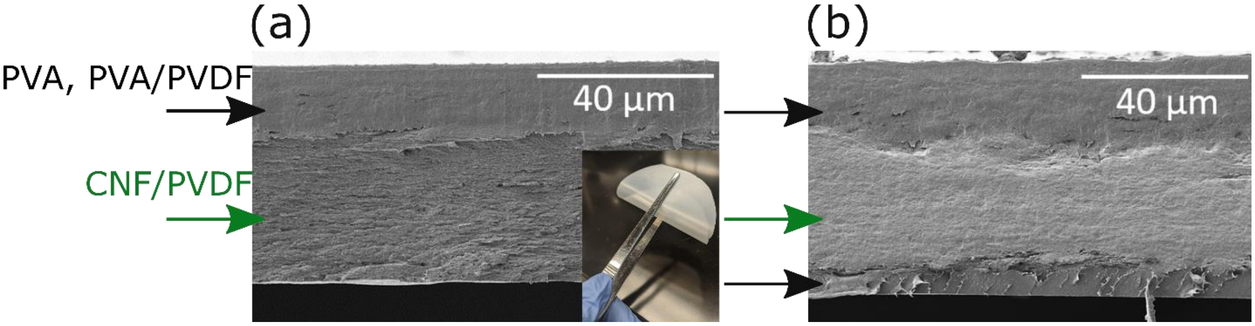

Figure 55. *Representative SEM micrographs of film cross-sections* for (a) bilayer 5m+10wt% PVDF: PVA film and (b) sandwich structure PVA: 5m+10wt%PVDF: PVA film.

6.2.4b Dielectric performance of bilayer and sandwich structure films

The frequency dependent properties of the as-prepared bilayer and sandwich structure films were compared to their single layer 5m+10 wt% PVDF counterpart, as well as a pure 5 minute CNF film, using EIS. As can be seen from **Figure 56a**, the relative permittivity of the bilayer and sandwich structure films increased almost one order of magnitude compared to a single layer 5m+10 wt% PVDF composite film, restoring the permittivity to that of the pure 5 minute CNF film. This is due to the additional polarizability of both the PVA and PVDF chains, contributing to the overall permittivity of the structure[26]. Although both the bilayer and sandwich structure films with 3 wt% PVDF included achieve a slightly higher permittivity than the pure PVA layered counterparts, the effect is minimal. This slight increase is likely due to the innate higher dielectric constant of the PVDF chains compared to the PVA.

As the conductivity is directly proportional to the permittivity, bilayer and sandwich structure films also showed approximately an order of magnitude increase compared to their single layer film counterparts (**Figure 56b**). However, given the significant enhancement of the permittivity, allowing for increased charge storage, the slight increase in conductivity is a worthwhile side effect given how low the conductivity remains at lower and more applicable frequencies. Interestingly, both layered film structures presented only slightly higher losses compared to the single layer composite CNF/PVDF film (**Figure 56c**). The maintenance of losses with increased permittivity is consistent with other layered film structures where the interfaces act as blocking layers than can slow or stop the spread of charge between layers[29,199].

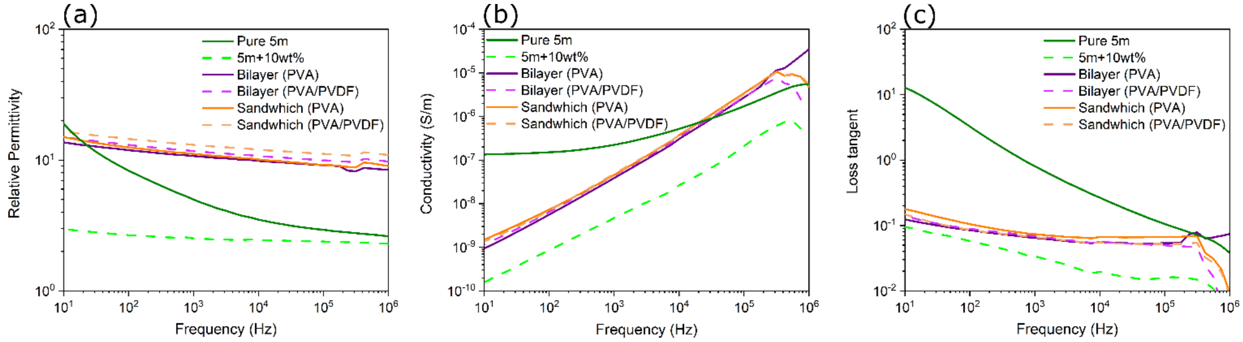

Figure 56. *Frequency dependent dielectric properties* calculated from EIS measurements for bilayer and sandwich structure films compared to their single layer film counterparts. (a) Relative permittivity, (b) AC conductivity, and (c) loss tangent.

Due to the thicker resulting structures of the multi-layered films, at 39.5±3μm and 46±5μm for bilayer and sandwich structure films respectively, the breakdown strength was unable to be collected given the limit of the high voltage amplifier used. Future work will ensure thinner films are prepared to allow for the breakdown strength of multi-layered films to be measured. In an effort to still gain insight into the energy storage capabilities of the multi-layered films, P-E loops were collected up until the maximum possible electric field was reached given the thickness the film at each electrode measured. Results of the P-E loop analysis in **Figure 57** demonstrate an improvement in charge density for all bilayer and sandwich structure films studied, regardless of if PVDF was added to the PVA layer/s, demonstrated by the ability to continue to store charge at significantly higher applied electric fields than was seen for the single layer composite film. A reduction in hysteresis compared to the single layer film was also seen for all multi-layered films studied. Similar results have been reported where the thickness of each layer plays an important role in the hysteresis displayed by multi-layered films, claiming that the interfaces separating each layer may act as charge barriers, limiting the loss of charge through each layer[29,199]. Reports demonstrate that, given an applied electric field, charges start to build up at the interfaces due to drift, yielding an ion concentration gradient and drift current. This migration of charge is possible through the free volume, similar to gas diffusion through polymers. This charge buildup continues until the drift current is balanced by the diffusion current. In the case of thinner film layers, the charge build-up is less pronounced and drift is less likely, reducing hysteresis even further, especially at higher fields[29].

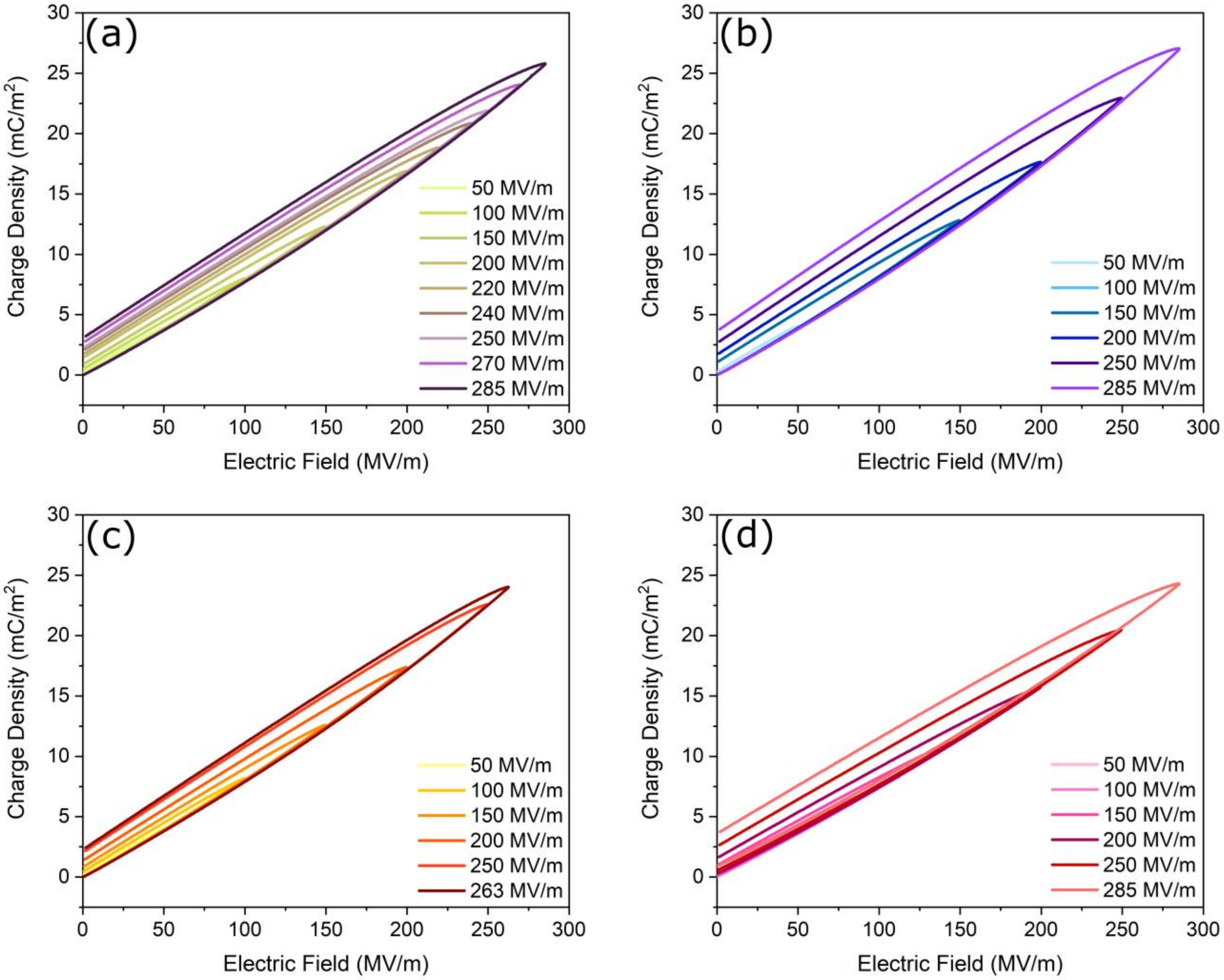

Figure 57. *Partial P-E loops measured up until limited applied voltage* (electric field) was reached due to thicker multi-layered film structures (a) 5m+10 wt% PVDF: PVA bilayer film, (b) 5m+10 wt% PVDF: PVA/PVDF bilayer film, (c) PVA: 5m+10 wt% PVDF: PVA sandwich structure film, and (d) PVA/PVDF: 5m+10 wt% PVDF: PVA/PVDF sandwich structure film.

Although the maximum breakdown strength of the multi-layered films was unable to be measured, the discharge energy density and efficiency for the applied electric fields studied were still calculated from the P-E loop data, and plotted against that of the single layer 5m +10 wt% PVDF film for comparison (**Figure 58**). It is obvious that both the bilayer and sandwich structured films have a higher breakdown strength than the single layer film counterpart, as they are able to withstand significantly higher applied electric fields while maintaining the ability to store charge. Although both the bilayer and sandwich structure films appear to have the same discharge energy density, the efficiency of the sandwich films remains slightly higher, likely due to the low energy losses of the material.

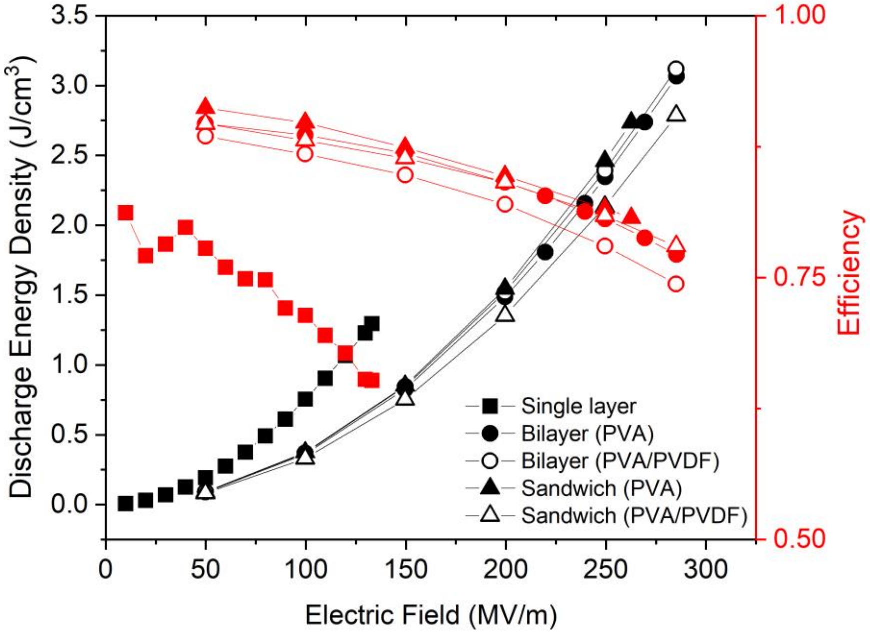

Figure 58. *Discharge energy density and efficiency curves* comparing bilayer and sandwich structure composite films prepared with both PVA and PVA/PVDF additional layers. Multi-layered films are also compared to their single layer composite 5m+10 wt% PVDF film counterpart.

6.3 Conclusion

Cellulose nanofibril (CNF) and PVDF composite films were fabricated using a sustainable water-based preparation method, limiting the use of harsh chemicals typically needed to solubilize PVDF. The effect of oxidation time of resulting CNF morphology and charge density, and the relationship to dielectric performance and energy storage, were studied in detail. Results indicate that composite films prepared with 10 wt% PVDF and CNF oxidized for the shortest amount of time resulted in the highest breakdown strength while maintaining the lowest losses. Bilayer and sandwich structured films were evaluated based on the potential for improved breakdown strength and energy storage capabilities. Preliminary results demonstrate multi-layered structures with enhanced flexibility and dielectric performance while maintaining the low losses obtained with single layer composite films and a reduction in hysteresis. Although additional breakdown strength and higher applied electric field analyses are needed to fully understand the material properties, preliminary results demonstrate the potential of multi-layer CNF based films for use as flexible dielectrics for advanced energy storage devices.

VII. Conclusion and future work

As technology continues to advance and the demand for energy continues to rise, the need for smart electronics will continue to grow. With consumers reaching for more mobile electronics and a dependence on Internet of Things (IoT) devices, the portability and robustness of devices is becoming of paramount importance[12]. Novel flexible electronics with commercial viability are gaining considerable interest for their ability to be implemented in portable and wearable devices. In this work, the use of cellulose microfibers (pulp) and cellulose nanofibrils (CNF) have been evaluated as alternative polymer materials to reduce the dependence on petrochemical derived sources in multifunctional sensing and energy storage applications. Here, a highly sensitive paper nanocomposite was developed by integrating carbon nanotubes into a hierarchical network of pulp fibers and CNF. Composite material properties were optimized for a response to liquid water. Achieved sensitivity spans an outstanding four orders of magnitude, even after 30 cycles and 6-month natural aging, due to the rapid and reversible hygroexpansion of the hierarchical cellulose network, altering the intertube distance between neighboring CNTs, and resulting in changes to the overall conductivity of the nanocomposite. Optimized material composition also enabled the detection of water volumes as small as 0.25 µL with great accuracy. While a fifth of the world population lacks access to safe water, leaky pipes and wasteful irrigation systems are a major contributor to water scarcity on the planet. As the American Society of Civil Engineers indicates that about a quarter-million water line breaks occur each year in the U.S., representing more than 26 billion liters lost each day due to leaky pipes, the need for a rapid and reliable remote leak detector is of paramount importance to reduce water waste[138]. The successful small volume detection limit of paper nanocomposites demonstrates opportunity as an inexpensive and flexible remote water leak detector.

Paper nanocomposites were successfully adapted from the batch-scale to pilot-scale production using an aqueous-phase dynamic web forming process run at 3.2 m/min, enabling the scalable production of sensory paper nanocomposites with minimal nanoparticle loss due to the tailored interfacial bonding between CNT and cellulose components, and maintained sensitivity. The resulting material is applied in a remote IoT leak detection device. In collaboration with the ATLAS team at CERN, the long term reliability of paper nanocomposites and integration as a remote water sensor were thoroughly evaluated and demonstrate successful leak detection even under significant humidity and temperature swings. While initial results demonstrate reduced false alerts compared to existing systems, and a chasing average algorithm (ESI) can be used to prevent false positives in remote leak detection, additional work will be completed to optimize signal processing and enhance sensing predictions in unstable environments (i.e. temperature and humidity fluctuations).

Composite films based on a CNF matrix were developed as a more environmentally friendly alternative to traditional ceramic and polymeric materials used in dielectric energy storage devices. While typical polymeric films are processed using harsh chemicals and energy intensive processes, CNF can be processed using a facile water-based film casting process. Here, poly(vinylidene fluoride) (PVDF) nanoparticles are imbedded in a TEMPO-oxidized CNF matrix, and the resulting frequency dependent dielectric properties and breakdown strength were studied in detail. By controlling the TEMPO oxidation process and reducing the effective oxidation time from 3 hours to 5 minutes, films losses were reduced by two fold while the breakdown strength was enhanced by twofold. Preliminary energy density analysis indicates enhanced energy storage capacity compared to other biodegradable cellulose composite films, advancing the use of alternative polymers in energy storage applications. Preliminary results demonstrate that multi-layered film structures, combining CNF/PVDF layers with PVA/PVDF layers, offer enhanced flexibility and have potential to further increase breakdown strength and significantly increase the potential for energy storage compared to single layer films structures. Continued efforts will be focused on optimizing the composition of each layer in multi-layered film structures, and refining the interfacial regions between layers to maximize the benefits each layer contributes and increase the overall device efficiency. Special interest will be taken toward enhancing the overall relative permittivity, while achieving a higher dielectric breakdown strength. Polarization-electric field (P-E) loops will be studied in detail to determine the optimum operational electric field that yields the best device performance in terms of discharge energy density and efficiency. Through the optimization of multi-layered film structures, enhancements in breakdown strength and energy storage capabilities can be achieved. These improvements offer significant advancement for the incorporation of sustainable polymer based materials for use in dielectric capacitors, capable of high power density and extended life span. Additional work will also be completed to assess the ability of optimized multi-layered films to generate electrical energy as piezoelectric devices. Combined with the potential for increased energy storage capabilities, the ability to generate energy positions cellulose based materials as a viable alternative to help meet the growing electrical energy demands.

VIII. References

[1] D. Zhao, Y. Zhu, W. Cheng, W. Chen, Y. Wu, H. Yu, *Advanced Materials*, **2020**, 2000619.

[2] S. Elazzouzi-Hafraoui, Y. Nishiyama, J.-L. Putaux, L. Heux, F. Dubreuil, C. Rochas, *Biomacromolecules*, **2008**, *9*, 57.

[3] T. Saito, Y. Nishiyama, J.-L. Putaux, M. Vignon, A. Isogai, *Biomacromolecules*, **2006**, *7*, 1687.

[4] A. Alemdar, M. Sain, *Bioresource Technology*, **2008**, *99*, 1664.

[5] T. Imai, J. Sugiyama, *Macromolecules*, **1998**, *31*, 6275.

[6] J.-F. Revol, *Carbohydrate Polymers*, **1982**, *2*, 123.

[7] R. M. B. Jr, *Journal of Macromolecular Science, Part A*, **1996**, *33*, 1345.

[8] M. Iguchi, S. Yamanaka, A. Budhiono, *Journal of Materials Science*, **2000**, *35*, 261.

[9] M. Khandelwal, A. H. Windle, *MRS Online Proceedings Library Archive*, **2013**, *1504*, DOI 10.1557/opl.2013.379.

[10] R. J. Moon, A. Martini, J. Nairn, J. Simonsen, J. Youngblood, *Chem. Soc. Rev.*, **2011**, *40*, 3941.

[11] H. Koga, M. Nogi, in *Lignocellulosics* (Eds.: I. Filpponen, M.S. Peresin, T. Nypelö), Elsevier, Amsterdam, **2020**, pp. 171–191.

[12] Y.-W. Lim, J. Jin, B.-S. Bae, *Advanced Materials*, **2020**, *32*, 1907143.

[13] J. Fan, S. Zhang, F. Li, Y. Yang, M. Du, *Cellulose*, **2020**, *27*, 9157.

[14] J. Zhang, S. M. Goodman, H. G. Wise, A. B. Dichiara, J.-H. Chung, *J. Mater. Chem. C*, **2021**, DOI 10.1039/D0TC05526C.

[15] S. Chen, Y. Song, D. Ding, Z. Ling, F. Xu, *Advanced Functional Materials*, **2018**, *28*, 1802547.

[16] C. Wang, Z.-Z. Pan, W. Lv, B. Liu, J. Wei, X. Lv, Y. Luo, H. Nishihara, Q.-H. Yang, *Small*, **2019**, *15*, 1805363.

[17] Z. Pang, Z. Yang, Y. Chen, J. Zhang, Q. Wang, F. Huang, Q. Wei, *Colloids and Surfaces A: Physicochemical and Engineering Aspects*, **2016**, *494*, 248.

[18] S. K. Mahadeva, S. Yun, J. Kim, *Sensors and Actuators A: Physical*, **2011**, *165*, 194.

[19] A. B. Dichiara, A. Song, S. M. Goodman, D. He, J. Bai, *J. Mater. Chem. A*, **2017**, *5*, 20161.

[20] M. Chang, T. Song, X. Liu, Q. Lin, B. He, J. Ren, *Current Medicinal Chemistry*, **2020**, *27*, 4593.

[21] N. O. Gomes, E. Carrilho, S. A. S. Machado, L. F. Sgobbi, *Electrochimica Acta*, **2020**, *349*, 136341.

[22] L. Dai, D. W. Chang, J.-B. Baek, W. Lu, *Small*, **2012**, *8*, 1130.

[23] S. Ummartyotin, H. Manuspiya, *Renewable and Sustainable Energy Reviews*, **2015**, *41*, 402.

[24] T. Huber, J. Müssig, O. Curnow, S. Pang, S. Bickerton, M. P. Staiger, *J Mater Sci*, **2012**, *47*, 1171.

[25] B. Baghaei, M. Skrifvars, *Molecules*, **2020**, *25*, 2836.

[26] J. Che, W. Neri, I. Ly, P. Poulin, C. Zakri, J. Yuan, *ACS Appl. Energy Mater.*, **2020**, *3*, 9107.

[27] H. Pan, J. Ma, J. Ma, Q. Zhang, X. Liu, B. Guan, L. Gu, X. Zhang, Y.-J. Zhang, L. Li, Y. Shen, Y.-H. Lin, C.-W. Nan, *Nature Communications*, **2018**, *9*, 1813.

[28] F. Torres-Canas, J. Yuan, I. Ly, W. Neri, A. Colin, P. Poulin, *Advanced Functional Materials*, **2019**, *29*, 1901884.

[29] M. Mackey, D. E. Schuele, L. Zhu, L. Flandin, M. A. Wolak, J. S. Shirk, A. Hiltner, E. Baer, *Macromolecules*, **2012**, *45*, 1954.

[30] A. M. Abdel-karim, A. H. Salama, M. L. Hassan, *Journal of Physical Organic Chemistry*, **2018**, *31*, e3851.

[31] J.-H. Kim, D. Lee, Y.-H. Lee, W. Chen, S.-Y. Lee, *Advanced Materials*, **2019**, *31*, 1804826.

[32] J. Wang, C. Carlos, Z. Zhang, J. Li, Y. Long, F. Yang, Y. Dong, X. Qiu, Y. Qian, X. Wang, *ACS Appl. Mater. Interfaces*, **2020**, *12*, 26399.

[33] S. Rajala, T. Siponkoski, E. Sarlin, M. Mettänen, M. Vuoriluoto, A. Pammo, J. Juuti, O. J. Rojas, S. Franssila, S. Tuukkanen, *ACS Appl. Mater. Interfaces*, **2016**, *8*, 15607.

[34] H. V. Lee, S. B. A. Hamid, S. K. Zain, *Sci. World. J.*, **2014**, *2014*, DOI 10.1155/2014/631013.

[35] M. A. S. Azizi Samir, F. Alloin, A. Dufresne, *Biomacromolecules*, **2005**, *6*, 612.

[36] T. Puspasari, N. Pradeep, K.-V. Peinemann, *Journal of Membrane Science*, **2015**, *491*, DOI 10.1016/j.memsci.2015.05.002.

[37] A. Aravamudhan, D. M. Ramos, A. A. Nada, S. G. Kumbar, in *Natural and Synthetic Biomedical Polymers* (Eds.: S.G. Kumbar, C.T. Laurencin, M. Deng), Elsevier, Oxford, **2014**, pp. 67–89.

[38] R. Kathahira, T. J. Elder, G. T. Beckham, *Lignin Valorization: Emerging Approaches Energy and Environment Series No. 19*, **2018**, *19*, 1.

[39] Y. Pu, F. Hu, F. Huang, B. H. Davison, A. J. Ragauskas, *Biotechnology for Biofuels*, **2013**, *6*, 15.

[40] G. Smook, *Handbook For Pulp and Paper Technologists (The SMOOK Book), Fourth Edition - Handbook For Pulp & Paper Technologists Fourth Edition*, TAPPI Press, **2016**.

[41] F. J. Martin-Martinez, *PNAS*, **2018**, *115*, 7174.

[42] M. A. Hubbe, O. J. Rojas, L. A. Lucia, M. Sain, *BioResources*, **2008**, *3*, 929.

[43] W. Stelte, A. R. Sanadi, *Ind. Eng. Chem. Res.*, **2009**, *48*, 11211.

[44] I. Siró, D. Plackett, *Cellulose*, **2010**, *17*, 459.

[45] D. Platikanov, D. Exerowa, *Highlights in Colloid Science*, John Wiley & Sons, **2009**.

[46] Y. Habibi, L. A. Lucia, O. J. Rojas, *Chem. Rev.*, **2010**, *110*, 3479.

[47] H. P. S. Abdul Khalil, Y. Davoudpour, Md. N. Islam, A. Mustapha, K. Sudesh, R. Dungani, M. Jawaid, *Carbohydrate Polymers*, **2014**, *99*, 649.

[48] P. Phanthong, P. Reubroycharoen, X. Hao, G. Xu, A. Abudula, G. Guan, *Carbon Resources Conversion*, **2018**, *1*, 32.

[49] J. George, K. V. Ramana, A. S. Bawa, Siddaramaiah, *International Journal of Biological Macromolecules*, **2011**, *48*, 50.

[50] A. Isogai, T. Saito, H. Fukuzumi, *Nanoscale*, **2011**, *3*, 71.

[51] X. Yang, M. S. Reid, P. Olsén, L. A. Berglund, *ACS Nano*, **2020**, *14*, 724.

[52] S. Dong, M. Roman, *J. Am. Chem. Soc.*, **2007**, *129*, 13810.

[53] S. P. Mishra, A.-S. Manent, B. Chabot, C. Daneault, *BioResources*, **2012**, *7*, 0422.

[54] F. Jiang, S. Han, Y.-L. Hsieh, *RSC Advances*, **2013**, *3*, 12366.

[55] Q. Li, S. Renneckar, *Biomacromolecules*, **2011**, *12*, 650.

[56] M. Pääkkö, M. Ankerfors, H. Kosonen, A. Nykänen, S. Ahola, M. Österberg, J. Ruokolainen, J. Laine, P. T. Larsson, O. Ikkala, T. Lindström, *Biomacromolecules*, **2007**, *8*, 1934.

[57] A. Dufresne, J.-Y. Cavaillé, M. R. Vignon, *Journal of Applied Polymer Science*, **1997**, *64*, 1185.

[58] A. Dufresne, *Materials Today*, **2013**, *16*, 220.

[59] J. Levanič, V. P. Šenk, P. Nadrah, I. Poljanšek, P. Oven, A. Haapala, *ACS Sustainable Chem. Eng.*, **2020**, *8*, 17752.

[60] T. Saito, S. Kimura, Y. Nishiyama, A. Isogai, *Biomacromolecules*, **2007**, *8*, 2485.

[61] Y. Li, H. Zhu, F. Shen, J. Wan, S. Lacey, Z. Fang, H. Dai, L. Hu, *Nano Energy*, **2015**, *13*, 346.

[62] A. Hajian, S. B. Lindström, T. Pettersson, M. M. Hamedi, L. Wågberg, *Nano Lett.*, **2017**, *17*, 1439.

[63] H. Qi, E. Mäder, J. Liu, *Sensors and Actuators B: Chemical*, **2013**, *185*, 225.

[64] S. Yun, S. Jang, G.-Y. Yun, J. Kim, *Smart Mater. Struct.*, **2009**, *18*, 117001.

[65] H. Qi, J. Liu, J. Pionteck, P. Pötschke, E. Mäder, *Sensors and Actuators B: Chemical*, **2015**, *213*, 20.

[66] S. Kotresh, Y. T. Ravikiran, H. G. Raj Prakash, CH. V. V. Ramana, S. C. Vijayakumari, S. Thomas, *Cellulose*, **2016**, *23*, 3177.

[67] S. Bi, L. Hou, H. Zhao, L. Zhu, Y. Lu, *Journal of Materials Chemistry A*, **2018**, *6*, 16556.

[68] M. Amjadi, M. Sitti, *ACS Nano*, **2016**, *10*, 10202.

[69] M. Weng, P. Zhou, L. Chen, L. Zhang, W. Zhang, Z. Huang, C. Liu, S. Fan, *Advanced Functional Materials*, **2016**, *26*, 7244.

[70] S. Kanaparthi, S. Badhulika, *Sensors and Actuators B: Chemical*, **2017**, *242*, 857.

[71] F. Güder, A. Ainla, J. Redston, B. Mosadegh, A. Glavan, T. J. Martin, G. M. Whitesides, *Angew Chem Int Ed Engl*, **2016**, *55*, 5727.

[72] H. Oh, S. S. Kwak, B. Kim, E. Han, G.-H. Lim, S.-W. Kim, B. Lim, *Advanced Functional Materials*, **2019**, *29*, 1904066.

[73] L. Hu, J. W. Choi, Y. Yang, S. Jeong, F. La Mantia, L.-F. Cui, Y. Cui, *Proc. Natl. Acad. Sci. U.S.A.*, **2009**, *106*, 21490.

[74] M. Agarwal, Q. Xing, B. S. Shim, N. Kotov, K. Varahramyan, Y. Lvov, *Nanotechnology*, **2009**, *20*, 215602.

[75] R. E. Anderson, J. Guan, M. Ricard, G. Dubey, J. Su, G. Lopinski, G. Dorris, O. Bourne, B. Simard, *J. Mater. Chem.*, **2010**, *20*, 2400.

[76] M. Imai, K. Akiyama, T. Tanaka, E. Sano, *Composites Science and Technology*, **2010**, *70*, 1564.

[77] K. Parikh, K. Cattanach, R. Rao, D.-S. Suh, A. Wu, S. K. Manohar, *Sensors and Actuators B: Chemical*, **2006**, *113*, 55.

[78] J. A. Covington, J. W. Gardner, D. Briand, N. F. de Rooij, *Sensors and Actuators B: Chemical*, **2001**, *77*, 155.

[79] J. Barkauskas, *Talanta*, **1997**, *44*, 1107.

[80] A. Bouvree, J.-F. Feller, M. Castro, Y. Grohens, M. Rinaudo, *Sensors and Actuators B: Chemical*, **2009**, *138*, 138.

[81] T. Villmow, S. Pegel, A. John, R. Rentenberger, P. Pötschke, *Materials Today*, **2011**, *14*, 340.

[82] X. Wu, Y. Han, X. Zhang, C. Lu, *Physical Chemistry Chemical Physics*, **2017**, *19*, 16198.

[83] K. Bethke, S. Palantöken, V. Andrei, M. Roß, V. S. Raghuwanshi, F. Kettemann, K. Greis, T. T. K. Ingber, J. B. Stückrath, S. Valiyaveettil, K. Rademann, *Advanced Functional Materials*, **2018**, *28*, 1800409.
[84] **2011**.
[85] O. Zaytseva, G. Neumann, *Chemical and Biological Technologies in Agriculture*, **2016**, *3*, 17.
[86] S. Iijima, T. Ichihashi, *Nature*, **1993**, *363*, 603.
[87] S. Iijima, *Nature*, **1991**, *354*, 56.
[88] N. Arora, N. N. Sharma, *Diamond and Related Materials*, **2014**, *50*, 135.
[89] Y. Ma, A. B. Dichiara, D. He, L. Zimmer, J. Bai, *Carbon*, **2016**, *107*, 171.
[90] S. Iijima, *Physica B: Condensed Matter*, **2002**, *323*, 1.
[91] R. K. Abu Al-Rub, A. I. Ashour, B. M. Tyson, *Construction and Building Materials*, **2012**, *35*, 647.
[92] *Carbon Nanotechnology-Recent Development in Chemistry, Physics, Materials Science and Device Applications*, Elsevier Science, **2006**.
[93] P. G. Collins, P. Avouris, *Scientific American*, **2000**, *283*, 62.
[94] Safa O. Kasap, *Principles of Electronic Materials and Devices*, McGraw Hill Education, **2006**.
[95] J. Gao, Y. Wang, Y. Liu, X. Hu, X. Ke, L. Zhong, Y. He, X. Ren, *Scientific Reports*, **2017**, *7*, 40916.
[96] Q. Chen, Y. Shen, S. Zhang, Q. m. Zhang, *Annu. Rev. Mater. Res.*, **2015**, *45*, 433.
[97] B. Fan, M. Zhou, C. Zhang, J. Yuan, D. He, Y. Liu, P. Haghi-Ashtiani, J. Bai, *J. Phys. Chem. C*, **2019**, *123*, 11993.
[98] H. Y. Choi, Y. G. Jeong, *Composites Part B: Engineering*, **2019**, *168*, 58.
[99] Y. Zhang, Q. Chi, L. Liu, T. Zhang, C. Zhang, Q. Chen, X. Wang, Q. Lei, *ACS Appl. Energy Mater.*, **2018**, *1*, 6320.
[100] M. A. Wolak, M.-J. Pan, A. Wan, J. S. Shirk, M. Mackey, A. Hiltner, E. Baer, L. Flandin, *Appl. Phys. Lett.*, **2008**, *92*, 113301.
[101] K. Yin, Z. Zhou, D. E. Schuele, M. Wolak, L. Zhu, E. Baer, *ACS Appl. Mater. Interfaces*, **2016**, *8*, 13555.
[102] H. A. D. Luca, W. B. Campbell, O. Maass, *Canadian Journal of Research*, **2011**, DOI 10.1139/cjr38b-037.
[103] S. K. Mahadeva, K. Walus, B. Stoeber, *ACS Appl. Mater. Interfaces*, **2015**, *7*, 8345.
[104] G. Zhang, Q. Liao, Z. Zhang, Q. Liang, Y. Zhao, X. Zheng, Y. Zhang, *Advanced Science*, **2016**, *3*, 1500257.
[105] J. Tao, L. Jiao, Y. Deng, in *Nanocellulose Based Composites for Electronics* (Eds.: S. Thomas, Y.B. Pottathara), Elsevier, **2021**, pp. 73–100.
[106] X. Zeng, L. Deng, Y. Yao, R. Sun, J. Xu, C.-P. Wong, *J. Mater. Chem. C*, **2016**, *4*, 6037.
[107] S. El-Sayed, K. H. Mahmoud, A. A. Fatah, A. Hassen, *Physica B: Condensed Matter*, **2011**, *406*, 4068.
[108] L. L. Sun, B. Li, Z. G. Zhang, W. H. Zhong, *European Polymer Journal*, **2010**, *46*, 2112.
[109] E. Barnes, J. A. Jefcoat, E. M. Alberts, M. A. McKechnie, H. R. Peel, J. P. Buchanan, C. A. Weiss Jr., K. L. Klaus, L. C. Mimun, C. M. Warner, *Polymers (Basel)*, **2019**, *11*, DOI 10.3390/polym11071091.
[110] S. M. Goodman, N. Ferguson, A. B. Dichiara, *RSC Adv.*, **2017**, *7*, 5488.

[111] L. Segal, J. J. Creely, A. E. Martin, C. M. Conrad, *Textile Research Journal*, **1959**, *29*, 786.

[112] U. P. Agarwal, S. A. Ralph, C. Baez, R. S. Reiner, S. P. Verrill, *Cellulose*, **2017**, *24*, 1971.

[113] P. Alafogianni, K. Dassios, S. Farmaki, S. K. Antiohos, T. E. Matikas, N.-M. Barkoula, *Colloids and Surfaces A: Physicochemical and Engineering Aspects*, **2016**, *495*, 118.

[114] TAPPI, "TAPPI T 569 Internal bond strength," https://ipstesting.com/find-a-test/tappi-test-methods/tappi-t-569-internal-bond-strength/.

[115] Q. Li, L. Chen, M. R. Gadinski, S. Zhang, G. Zhang, H. U. Li, E. Iagodkine, A. Haque, L.-Q. Chen, T. N. Jackson, Q. Wang, *Nature*, **2015**, *523*, 576.

[116] X. Zhang, J. Jiang, Z. Shen, Z. Dan, M. Li, Y. Lin, C.-W. Nan, L. Chen, Y. Shen, *Advanced Materials*, **2018**, *30*, 1707269.

[117] G. Zhang, B. Fan, P. Zhao, Z. Hu, Y. Liu, F. Liu, S. Jiang, S. Zhang, H. Li, Q. Wang, *ACS Appl. Energy Mater.*, **2018**, *1*, 1344.

[118] J.-W. Han, B. Kim, J. Li, M. Meyyappan, *J. Phys. Chem. C*, **2012**, *116*, 22094.

[119] H.-D. Huang, C.-Y. Liu, L.-Q. Zhang, G.-J. Zhong, Z.-M. Li, *ACS Sustainable Chem. Eng.*, **2015**, *3*, 317.

[120] H. Qi, B. Schulz, T. Vad, J. Liu, E. Mäder, G. Seide, T. Gries, *ACS Appl. Mater. Interfaces*, **2015**, *7*, 22404.

[121] S. Yun, J. Kim, *Sensors and Actuators B: Chemical*, **2010**, *150*, 308.

[122] Z. Pang, X. Sun, X. Wu, Y. Nie, Z. Liu, L. Yue, *Vacuum*, **2015**, *122*, 135.

[123] T.-W. Lee, S.-E. Lee, Y. G. Jeong, *Composites Science and Technology*, **2016**, *131*, 77.

[124] D.-H. Kim, I.-Y. Na, D. H. Lee, G. T. Kim, *RSC Adv.*, **2019**, *10*, 402.

[125] K. Ariga, J. P. Hill, Q. Ji, *Physical Chemistry Chemical Physics*, **2007**, *9*, 2319.

[126] Z. Yan, S. Chen, H. Wang, B. Wang, J. Jiang, *Carbohydrate Polymers*, **2008**, *74*, 659.

[127] L. Stobinski, B. Lesiak, L. Kövér, J. Tóth, S. Biniak, G. Trykowski, J. Judek, *Journal of Alloys and Compounds*, **2010**, *501*, 77.

[128] A. Koubaa, Z. Koran, *Tappi Journal*, **1995**, *78*, 103.

[129] G. T. Pham, Y.-B. Park, Z. Liang, C. Zhang, B. Wang, *Composites Part B: Engineering*, **2008**, *39*, 209.

[130] Alamusi, N. Hu, H. Fukunaga, S. Atobe, Y. Liu, J. Li, *Sensors*, **2011**, *11*, 10691.

[131] M. Park, H. Kim, J. P. Youngblood, *Nanotechnology*, **2008**, *19*, 055705.

[132] C.-Y. Li, T.-W. Chou, *Nanotechnology*, **2004**, *15*, 1493.

[133] A. T. Jafry, H. Lim, S. I. Kang, J. W. Suk, J. Lee, *Colloids and Surfaces A: Physicochemical and Engineering Aspects*, **2016**, *492*, 190.

[134] L. C. Fidale, N. Ruiz, T. Heinze, O. A. E. Seoud, *Macromolecular Chemistry and Physics*, **2008**, *209*, 1240.

[135] G. I. Mantanis, R. A. Young, R. M. Rowell, *Cellulose*, **1995**, *2*, 1.

[136] Y. Y. Liang, *Anal. Chem.*, **1990**, *62*, 2504.

[137] A. Samadi-Maybodi, R. Akhoondi, *J Fluoresc*, **2012**, *22*, 1217.

[138] Drinking Water Report, https://www.infrastructurereportcard.org/cat-item/drinking_water/.

[139] US EPA, "Fix a Leak Week," https://www.epa.gov/watersense/fix-leak-week.

[140] N. Kurra, G. U. Kulkarni, *Lab on a Chip*, **2013**, *13*, 2866.

[141] T. H. da Costa, E. Song, R. P. Tortorich, J.-W. Choi, *ECS J. Solid State Sci. Technol.*, **2015**, *4*, S3044.

[142] O.-S. Kwon, H. Kim, H. Ko, J. Lee, B. Lee, C.-H. Jung, J.-H. Choi, K. Shin, *Carbon*, **2013**, *58*, 116.

[143] H. Kataura, Y. Kumazawa, Y. Maniwa, I. Umezu, S. Suzuki, Y. Ohtsuka, Y. Achiba, *Synthetic Metals*, **1999**, *103*, 2555.

[144] O. A. El Seoud, L. C. Fidale, N. Ruiz, M. L. O. D'Almeida, E. Frollini, *Cellulose*, **2008**, *15*, 371.

[145] A. A. Robertson, *Pulp and paper magazine of Canada*, **1964**, 171.

[146] A. A. Robertson, *TAPPI*, **1970**, *53*, 1331.

[147] M. Botková, Š. Šutý, M. Jablonský, L. Kucerkova, M. Vrška, *Cell Chem Technol*, **2013**, *47*, 95.

[148] Qing, Wu, Cai, and Li, "Water-Triggered Dimensional Swelling of Cellulose Nanofibril Films: Instant Observation Using Optical Microscope," DOI 10.1155/2013/594734https://www.hindawi.com/journals/jnm/2013/594734/.

[149] S. Fält, L. Wågberg, E.-L. Vesterlind, *Langmuir*, **2003**, *19*, 7895.

[150] V. Ottesen, K. Syverud, *Cellulose*, **2021**, *28*, 19.

[151] S. Zhang, F. Zhang, Y. Pan, L. Jin, B. Liu, Y. Mao, J. Huang, *RSC Advances*, **2018**, *8*, 5678.

[152] C. Forró, L. Demkó, S. Weydert, J. Vörös, K. Tybrandt, *ACS Nano*, **2018**, *12*, 11080.

[153] Y. Qing, Y. Wu, Z. Cai, X. Li, *Journal of Nanomaterials*, **2013**, *2013*, 1.

[154] H. Qi, J. Liu, Y. Deng, S. Gao, E. Mäder, *J. Mater. Chem. A*, **2014**, *2*, DOI 10.1039/C3TA14820C.

[155] S. Bi, W. Dong, B. Lan, H. Zhao, L. Hou, L. Zhu, Y. Xu, Y. Lu, *Composites Part A: Applied Science and Manufacturing*, **2019**, *124*, 105452.

[156] Y. Chen, P. Pötschke, J. Pionteck, B. Voit, H. Qi, *Journal of Materials Chemistry A*, **2018**, *6*, 7777.

[157] P. A. Larsson, L. Wågberg, *Cellulose*, **2010**, *17*, 891.

[158] P. Yuvaraj, J. Ajantha, S. Easwaramoorthi, J. Raghava Rao, *New Journal of Chemistry*, **2020**, *44*, 6566.

[159] P. Verma, M. L. Shofner, A. C. Griffin, *Phys. Status Solidi B*, **2014**, *251*, 289.

[160] C. Li, E. T. Thostenson, T.-W. Chou, *Appl. Phys. Lett.*, **2007**, *91*, 223114.

[161] A. Tejado, T. G. M. van de Ven, *Materials Today*, **2010**, *13*, 42.

[162] B. D. Chen, W. Tang, C. He, C. R. Deng, L. J. Yang, L. P. Zhu, J. Chen, J. J. Shao, L. Liu, Z. L. Wang, *Materials Today*, **2018**, *21*, 88.

[163] M. Xu, S. Wang, S. L. Zhang, W. Ding, P. T. Kien, C. Wang, Z. Li, X. Pan, Z. L. Wang, *Nano Energy*, **2019**, *57*, 574.

[164] J. Thornton, R. Sturm, G. Kunkel, *Water Loss Control, Second Edition*, McGraw-Hill, **2008**.

[165] US EPA, "Statistics and Facts," https://www.epa.gov/watersense/statistics-and-facts.

[166] D. O. Castro, Z. Karim, L. Medina, J.-O. Häggström, F. Carosio, A. Svedberg, L. Wågberg, D. Söderberg, L. A. Berglund, *Composites Science and Technology*, **2018**, *162*, 215.

[167] B. Nordström, *J Pulp Pap Sci*, **1995**, *21*, 427.

[168] H. C. Kim, J. W. Kim, L. Zhai, J. Kim, *Cellulose*, **2019**, *26*, 5821.

[169] Q. Meng, T. Wang, *Applied Mechanics Reviews*, **2019**, *71*, 040801.

[170] Metz, "Homeowners Insurance For Burst Pipes And Water Leaks," https://www.forbes.com/advisor/homeowners-insurance/water-damage/.

[171] Facts + Statistics: Homeowners and renters insurance | III, https://www.iii.org/fact-statistic/facts-statistics-homeowners-and-renters-insurance.
[172] B. Matthias, A. von Hippel, *Phys. Rev.*, **1948**, *73*, 1378.
[173] R. Freer, F. Azough, *Journal of the European Ceramic Society*, **2008**, *28*, 1433.
[174] S. K. Mahadeva, K. Walus, B. Stoeber, *ACS Appl. Mater. Interfaces*, **2014**, *6*, 7547.
[175] M. Guo, J. Jiang, Z. Shen, Y. Lin, C.-W. Nan, Y. Shen, *Materials Today*, **2019**, *29*, 49.
[176] M. Parit, P. Saha, V. A. Davis, Z. Jiang, *ACS Omega*, **2018**, *3*, 10679.
[177] B. Zhang, C. Huang, H. Zhao, J. Wang, C. Yin, L. Zhang, Y. Zhao, *Polymers*, **2019**, *11*, 2063.
[178] G. Chinga-Carrasco, *Micron*, **2013**, *48*, 42.
[179] Polyvinylidene Fluoride (PVDF) Plastic: Material Properties & Other Info, https://omnexus.specialchem.com/selection-guide/polyvinylidene-fluoride-pvdf-plastic.
[180] Arshad, Wahid, Rusop, Majid, Subban, and Rozana, "Dielectric and Structural Properties of Poly(vinylidene fluoride) (PVDF) and Poly(vinylidene fluoride-trifluoroethylene) (PVDF-TrFE) Filled with Magnesium Oxide Nanofillers."
[181] X. Cai, T. Lei, D. Sun, L. Lin, *RSC Adv.*, **2017**, *7*, 15382.
[182] C.-W. Tang, B. Li, L. Sun, B. Lively, W.-H. Zhong, *European Polymer Journal*, **2012**, *48*, 1062.
[183] G. Srivastava, V. Tiwari, *Journal of Polymer Research*, **2014**, *21*, 587.
[184] J. Keith Nelson, Ed., *Dielectric Polymer Composites*, Springer, **2010**.
[185] M. T. Sebastian, in *Dielectric Materials for Wireless Communication* (Ed.: M.T. Sebastian), Elsevier, Amsterdam, **2008**, pp. 11–47.
[186] Y. Feldman, A. Puzenko, Y. Ryabov, in *Advances in Chemical Physics*, **2005**, pp. 1–125.
[187] P. N. Vakil, F. Muhammed, D. Hardy, T. J. Dickens, S. Ramakrishnan, G. F. Strouse, *ACS Omega*, **2018**, *3*, 12813.
[188] X. L. Dong, X. F. Zhang, H. Huang, F. Zuo, *Appl. Phys. Lett.*, **2008**, *92*, 013127.
[189] J. K. Nelson, J. C. Fothergill, *Nanotechnology*, **2004**, *15*, 586.
[190] Andrew Jonscher, *J. Phys. D: Appl. Phys.*, **1999**, *32*, R57.
[191] T. Zangina, J. Hassan, K. A. Matori, R. S. Azis, U. Ahmadu, A. See, *Results in Physics*, **2016**, *6*, 719.
[192] Z.-M. Dang, J.-K. Yuan, S.-H. Yao, R.-J. Liao, *Advanced Materials*, **2013**, *25*, 6334.
[193] S. Li, G. Yin, S. Bai, J. Li, *IEEE Transactions on Dielectrics and Electrical Insulation*, **2011**, *18*, 1535.
[194] Z.-H. Shen, J.-J. Wang, Y. Lin, C.-W. Nan, L.-Q. Chen, Y. Shen, *Advanced Materials*, **2018**, *30*, 1704380.
[195] M.-S. Zheng, J.-W. Zha, Y. Yang, P. Han, C.-H. Hu, Z.-M. Dang, *Appl. Phys. Lett.*, **2016**, *109*, 072902.
[196] L. Yao, D. Wang, P. Hu, B.-Z. Han, Z.-M. Dang, *Advanced Materials Interfaces*, **2016**, *3*, 1600016.
[197] M. Stewart, M. G. Cain, D. A. Hall, *Ferroelectric Hysteresis Measurement & Analysis*, National Physics Laboratory, **1999**.
[198] F. Ram, A. Gudadhe, T. Vijayakanth, S. Aherrao, V. Borkar, R. Boomishankar, K. Shanmuganathan, *ACS Appl. Polym. Mater.*, **2020**, *2*, 2550.
[199] C. Zhang, L. Zhu, A. Olah, E. Baer, *Journal of Applied Polymer Science*, **2021**, *138*, 50298.